MEMS Actuation and Self-Assembly Applied to RF and Optical Devices

by

Niladri Sarkar

A thesis
presented to the University of Waterloo
in fulfillment of the
thesis requirement for the degree of
Master of Applied Science
in
Electrical and Computer Engineering

Waterloo, Ontario, Canada, 2004

I hereby declare that I am the sole author of this thesis. This is a true copy of the thesis, including any required final revisions, as accepted by my examiners.

I understand that my thesis may be made electronically available to the public.

Abstract

The focus of this work involves optical and RF (radio frequency) applications of novel microactuation and self-assembly techniques in MEMS (microelectromechanical systems). The scaling of physical forces into the micro domain is favorably used to design several types of actuators that can provide large forces and large static displacements at low operation voltages. A self-assembly method based on thermally induced localized plastic deformation of microstructures has been developed to obtain truly three-dimensional structures from a planar fabrication process.

RF applications of this work include variable discrete components such as capacitors and inductors as well as tunable coupling circuits. Optical applications include scanning micromirrors with large scan angles (>90 degrees), low operation voltages (<10 Volts), and up to three degrees of freedom. One and two-dimensional periodic structures with variable periods and orientations (with respect to an incident wave) are investigated as well, and analyzed using phased array concepts of electromagnetic theory.

Throughout the research, permanent tuning via plastic deformation and power-off latching techniques are used in order to demonstrate that the optical and RF devices can exhibit zero quiescent power consumption once their geometry is set.

Acknowledgements

I would like to thank my supervisors, Dr. Raafat Mansour and Dr. Sujeet Chaudhuri, for their unconditional support, patience and guidance. I was very fortunate to have advisors who allowed me to pursue my research interests with freedom, and who could always include me in their busy schedules whenever their expertise was needed.

I am grateful for the countless hours of discussion and teachings with Dr. Safavi-Naeini, who also agreed to be a reviewer. I appreciate the time that Dr. Sivoththaman has taken to read this thesis as well.

There are many people at Zyvex who made this work possible. Jim Von Ehr is a rare individual who has a vision and the enduring courage to pursue and finance it. Dr. George Skidmore and Matthew Ellis are outstanding managers and valued friends; they introduced me to the fascinating worlds of MEMS and nanotechnology, and provided the insight and resources that made this possible. My energetic and humorous colleagues Andre Mercanzini and Jeff Hochberg make my time at Zyvex even more enjoyable.

Aaron Geisberger is a friend who taught me most of what I know about MEMS, and he is truly an expert in his field. I consider his mentorship an important contribution to my education and career.

For sharing the everyday fun of graduate life, thanks to my fellow research group members Winter Yan and Arash Rohani, who had to serve as my sanity-check, coffee mates, and friends. They have helped me throughout my coursework and research, and even with the submission of this thesis. My dear friends Sath, Kyle, Nikki, Chris and Dara have been like an extended family to me with their support, encouragement, and companionship.

Last but not least, Wendy Gauthier and Wendy Boles (W^2) are remarkably organized and efficient people who have always managed to cope with my last-minute requests and general scatterbrained-ness. Thank you!

Dedication

To my mother, father, sister and brother-in-law.

My mother is an incredible woman. She has dedicated her life to care and provide for her children and has always placed the highest value on our education and health. My father is the most patient and resourceful person I know, and has given me unquestioning support throughout my life. My sister is a resilient person, whose mission in life is to bring happiness to others. I owe it all to them.

Table of Contents

List of Figures

List of Tables

Chapter 1
Introduction

As early as 1965, when Moore's law was first proposed, it was known that integrated circuits would follow an aggressive miniaturization trend with the "complexity for minimum component costs increasing at a rate of roughly a factor of two per year."[1] This bold prediction has been closely monitored with respect to microprocessors and has been remarkably accurate for the past four decades. In retrospect, the many technological breakthroughs that were required for the continued validity of Moore's law could not have been known a priori; nevertheless, the trend has continued and has even been used to describe progress in other technologies.

It was not until the early 1980's that silicon, which had already revolutionized the way we think about electronics, had begun to alter conventional perceptions of miniature mechanical devices and components. In 1982, the first review paper on the field, "Silicon as a mechanical material," was published in *Proceedings of the IEEE.* [2] "The basis of micromechanics is that silicon, in conjunction with its conventional role as an electronic material, and taking advantage of an already advanced microfabrication technology, can also be exploited as a high-precision high-strength high-reliability mechanical material..."[3] The microelectronics industry's mature micron-scale lithography, thin film deposition, ion implantation, and etching technologies applied to micromechanics had given rise to "Micromachines" in Japan, "Microsystems Technology" (MST) in Europe and Microelectromechanical Systems (MEMS) in North America. The applications of this research range from optical signal processing and RF devices to silicon valves and pumps (microfluidics) to nanopositioning (hard drives, scanning probe microscopes) to inertial sensors and inkjet print heads and more. Thus the field has a multidisciplinary nature that includes: silicon microfabrication technology, mechanical design, material science, tribology, control theory, metrology, robotics, optics, electromagnetics and many other areas. Despite the wide range of applications and the complex multifaceted nature of the field, several truly fascinating breakthroughs have occurred in order to ensure a rate of progress that is consistent with Moore's Law.

The focus of this work involves optical and RF applications of novel microactuation and self-assembly techniques in MEMS. The scaling of physical forces into the micro domain is favorably used to design several types of actuators that can provide large forces and large static displacements at low operation voltages. A self-assembly method based on thermally induced localized plastic deformation of microstructures has been developed to obtain truly three-dimensional structures from

a planar fabrication process. RF applications include variable discrete components such as capacitors and inductors as well as tunable coupling circuits. Optical applications include scanning micromirrors with large scan angles (>90 degrees), low operation voltages (<10 Volts), and multiple degrees of freedom. One and two-dimensional periodic structures with variable periods and orientations (with respect to an incident wave) are investigated as well, and analyzed using phased array concepts of electromagnetic theory. Throughout the research, permanent tuning via plastic deformation and power-off latching techniques are used in order to demonstrate that the optical and RF devices can exhibit zero quiescent power consumption once their geometry is set.

1.1 General Considerations

1.1.1 Microfabrication Processes

Silicon micromachining can be broadly categorized into bulk micromachining and surface micromachining (Figure 1). The former involves etching structures into the substrate (removal of material), and the latter involves the deposition and subsequent etching of thin films of sacrificial and structural materials (additive processes). Although the details of processing are beyond the scope of this work, some of the popular methods are briefly discussed here. Several texts have been published with exhaustive surveys of MEMS and silicon processing technology, some of which are included in the references.[4,2,5]

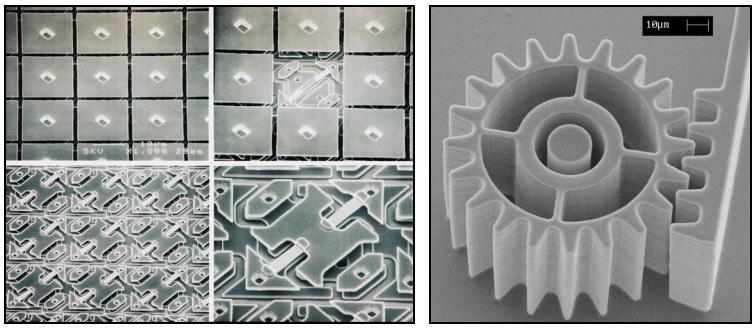

Figure 1: Surface micromachining (left) of Texas Instruments Digital Micromirror Device and bulk micromachining (right) of a silicon gear.

Most of the work presented in this thesis involves surface micromachined devices fabricated by the MUMPs (Multi-User MEMS Process), which is described further below.

1.1.1.1 Bulk Micromachining Process Technology

Several methods have been used for the removal of material from the bulk of the wafer. Wet or dry etchants are selected based on selectivity to etch masks, availability of etch stop methods, etch rate, cost, etch geometry, and many other criteria.**Error! Bookmark not defined.** The most common isotropic method for wet etching of silicon is HNA, a mixture of hydrofluoric acid (HF), nitric acid (HNO_3), and acetic acid (CH_3COOH). This method results in a spherical etch geometry when agitation is used. The most common anisotropic wet etchant is KOH, which etches preferentially along the <100> surface of the wafer, leaving the <111> surfaces exposed. When high aspect ratios are desired, dry etching methods are used, such as DRIE (deep reactive ion etching). High aspect ratios can also be obtained with thick photoresists such as SU8 and molding/electroplating processes such as LIGA for metallic materials.

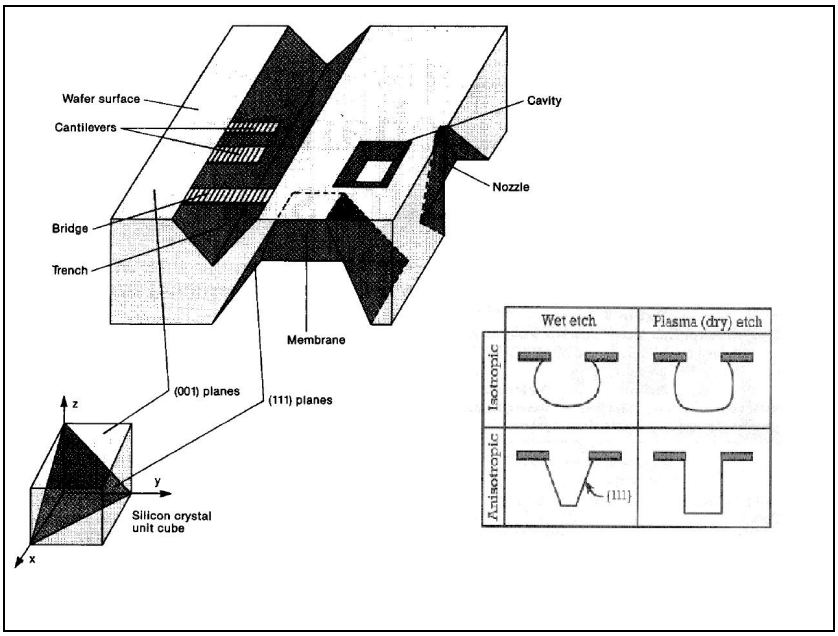

Figure 2: pictorial depiction of bulk micromachining techniques

1.1.1.2 Surface Micromachining Process Technology

Surface micromachining consists of the deposition, patterning, etching and release of thin films of material.[6] Techniques that fall under this category are sometimes called additive processes since material is added to the surface of the substrate. Unlike bulk micromachining, there is no removal of material from the substrate. In order to obtain functional electromechanical microsystems, both insulating and conductive films are required. Finally, in order to create free-standing

microstructures, sacrificial layers are used. These layers are deposited between mechanical layers, and removed near the end of processing.

Low pressure chemical vapor deposition (LPCVD), plasma enhanced chemical vapor deposition (PECVD), evaporation, sputtering, electroplating, epitaxial growth, and spin-coating are among the techniques used to deposit materials onto the surface of wafers.

Polysilicon is the most common structural material in surface micromachining, and is typically doped heavily in order to ensure good conductivity. There is no requirement for patterned doping, since a uniform doping level is desirable throughout the film. In some cases, a film of PSG (phosophosilicate glass) is used as a sacrificial layer and as a dopant – a high temperature anneal serves as a doping step (via diffusion) and as a stress reduction step.

Silicon nitride is extremely useful as an insulating material, and it can serve as a passivation layer, a capacitor dielectric, a structural material, and as a mask for etching or for selective oxidation of Si. This material is most commonly deposited using LPCVD as well, to obtain low stress, stoichiometric film quality. Several highly selective etch chemistries exist which allow the use of nitrides as an etch stop for oxides and polysilicon. LPCVD is preferred for nitride deposition over PECVD, since PECVD films are not stoichiometric and incorporate hydrogen, which affects etch selectivity.

Silicon dioxide is certainly the most commonly available dielectric in silicon fabrication laboratories. In surface micromachining, it often serves as a sacrificial layer and is commonly deposited using LPCVD or PECVD as opposed to thermal oxidation, which is more common in IC's. PSG (phosphosilicate glass, phosphorus doped) and BSG (borosilicate glass, boron-doped) can serve as a sacrificial layer and can be used to dope underlying layers of polysilicon during a thermal anneal process. BPSG (doped with both boron and phosphorus) is a low temperature oxide, and has excellent low-temperature reflow properties, which makes it suitable for use in CMP (chemical mechanical planarization) steps.

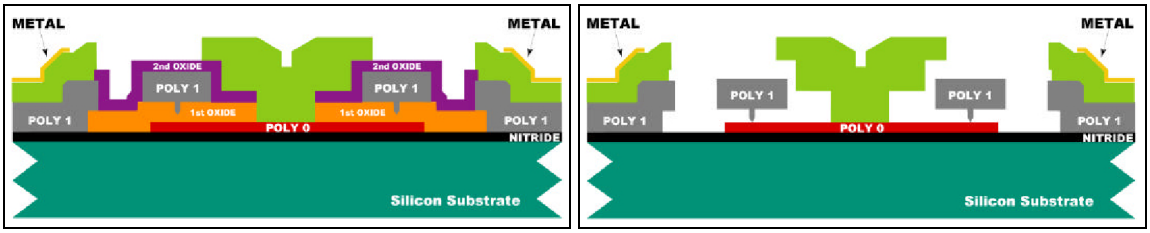

Figure 3: cutaway diagrams of the MUMPs process, before (left) and after (right) release.

By alternating layers of these and other materials (eg. polycristalline diamond, silicon carbide), 2 ½ dimensional structures of insulating, conducting, and sacrificial layers can be manufactured. After the release step in which the sacrificial layers are removed, these structures are become free standing electromechanical microsystems, which can be entirely removed from the substrate in some cases. As an example of a commonly used surface micromachining process, Figure 3 shows cutaway diagrams of the MUMPs (multi-user MEMS processes) process before and after release.

As shown in

Figure 3, the MUMPs process contains a nitride layer to electrically isolate polysilicon structures from one another. There is one layer of polysilicon (poly0) deposited directly onto the substrate, and 2 released poly layers (poly 1 and poly 2). Sacrificial oxides are deposited between all the structural layers. Finally, an evaporated metal layer is deposited and patterned using the liftoff technique.

There are two features in this diagram that are worth noting. First of all, in the top diagram, all the space occupied by oxide is replaced by fluids during the release process. These fluids exert capillary forces when they evaporate, and this can lead to stiction effects. Another feature is the dimple layer, which can be seen as protrusions from the bottom of the poly1 layer. The dimples prevent a large surface area of contact between poly1 and the layer below it. Finally, it should be noted that after the release process, mechanically free structures will no longer be constrained by oxide, and should be constrained by the other mechanical layers. For instance, in the case of the diagram above, the released poly 1 falls onto poly0, and is constrained from floating away in the etchant liquid by the poly 2 overhang above it. Special care should be taken to ensure that the constraining layers do not come into contact with the released parts with a large surface area of contact.

1.1.2 Scaling of Systems

A fundamental issue in microdynamics is the scaling of physical properties into the micro domain. [7] When a system is scaled down by a factor of 100, its volume and mass and hence the inertial and gravitational forces decrease by a factor of $100^3 = 1\ 000\ 000$. In many of the actuator designs that are discussed here, long singly-clamped beams with relatively small aspect ratios are used. In a scaled-up system, these beams would sag and inertial forces would make the design highly impractical; however, these forces are rarely a consideration in the design of microactuators, due to the small mass and high stiffness of the materials used. The thermodynamics of a scaled down

system are affected by this dramatic reduction in volume and mass as well. Since the thermal mass is reduced by a factor 1000 000 in this example, the thermal time constant for a beam is quite small. This makes it possible to thermally cycle a beam at several kHz in many cases. Electrothermal actuators of various geometries and materials are used throughout the research presented in this thesis. Typically, these actuators are based on Joule heating and can provide high static displacements and large forces at low operating voltages if properly designed.

Forces that scale as a function of area, such as electrostatic attraction, will decrease by a factor of only 10 000 when the system is scaled down 100 times. Thus, the ratio of electrostatic to inertial forces increases by a factor of 100. Comb drives, parallel plate actuators and scratch drive actuators are examples of practical electrostatic actuators at the micron scale.

The forces of surface tension scale with the linear dimension of the system and become large relative to other forces. Hence, the phenomenon of stiction during the release process of the MEMS becomes significant.[8]

1.1.3 Origins of Stiction

Stiction can arise during the sacrificial release process or while a device is in operation. The causes of adhesion are similar in both cases; however, the remedy for in use failure is more involved since it involves lubrication at the micron scale, an area of tribology that has not yet been thoroughly explored. In this section, the four most common sources of stiction will be discussed. Capillary forces may arise if the liquids used in the etching process evaporate slowly, and the reduced volume of the fluid "pulls" microstructures together. Hydrogen bridging results when thin films of moisture are adsorbed on hydrophilic surfaces, and O-H bonds form between the layers. Electrostatic forces from stored charge can arise during operation of electrostatic devices, or when materials with different work functions come into intimate contact. The van der Waals dispersion forces between two bodies are caused by mutual electric interaction of the induced dipoles in the two bodies. This is the dominant adhesion mechanism for hydrophobic surfaces.

1.1.3.1 Capillary Forces

A thin liquid layer between two solid plates can work as an adhesive. If the contact angle between liquid and solid is less than 90 degrees, the pressure inside the liquid drop will be lower than outside. This is a function of the hydrophobicity of the solid surface. In Figure 4, the geometry of a

water droplet on an oxide-coated Si (hydrophilic) substrate is compared to its geometry on a fluorinated SAM-coated Si (hydrophobic) substrate.[9]

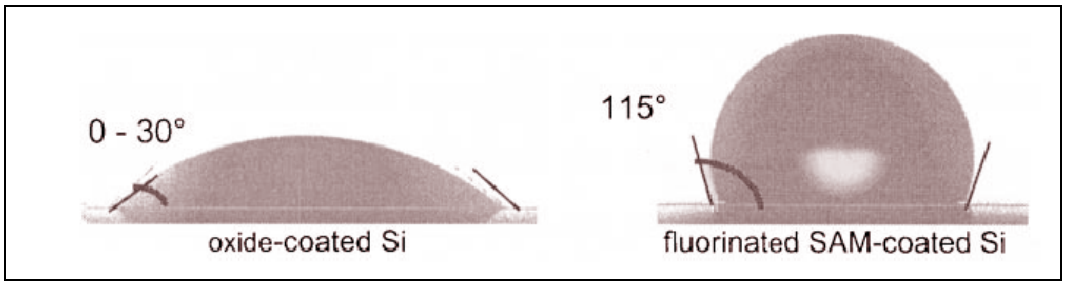

Figure 4: water droplet geometries on hydrophilic and hydrophobic surfaces

In the case of hydrophilic surfaces with a thin layer of liquid bridging them, the liquid acts as an adhesive. This situation is depicted below, in Figure 5. [9]

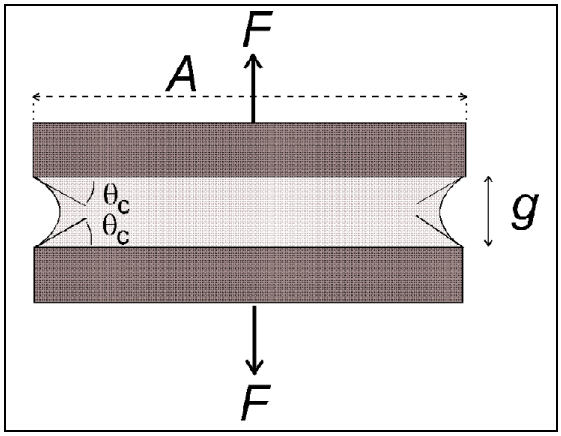

Figure 5: A thin layer of liquid acting as an adhesive between two plates

The pressure difference at the liquid-air interface is given by the Laplace equation[10]:

$$\Delta p_{la} = \frac{\gamma_{la}}{r}$$

where γ_{la} is the surface tension of the liquid - air interface and r is the radius of curvature of the meniscus :

$$r = -g / 2\cos\theta_c$$

In equilibrium, an external force can be applied to counteract the liquid bridging force, as shown in Figure 5. This force can be calculated as follows:[11]

$$F = -\Delta p_{la} A = \frac{2A\gamma_{la}\cos\theta_c}{g}$$

where A is the wetted area, and other quantities are drawn in the figure. These forces are on the same order of magnitude as the restoring forces of the thin beams of polysilicon that are widely used as support structures or in actuators in surface micromachined devices.

1.1.3.2 Hydrogen bridging

Hydrophilic silicon surfaces under atmospheric conditions contain adsorbed water layers.[12] When two hydrated surfaces come into close contact, hydrogen bonds may form between oxygen atoms and hydrogen atoms of the adsorbed water layers, as shown in Figure 6. The adhesion energies which have been reported for this process range from 60 to 270 mJ/m^2. This is high enough to permanently hold micromechanical plates together. The proposed mechanism for permanent stiction failure with hydrophilic surfaces therefore involves bringing two surfaces together by liquid bridging or otherwise, and permanently bonding them with hydrogen bridging forces.

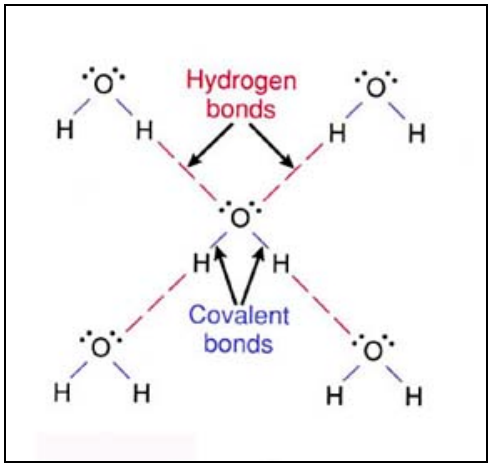

Figure 6: covalent bonding in water which leads to hydrogen bridging

1.1.3.3 Electrostatic Forces

Electrostatic forces can arise from a difference in work functions or from charging of opposed surfaces. A difference in work functions will lead to an electrical double layer by a net transfer of electrons from one layer to another, similar to the cause of band bending that is observed

to occur in a Schottky junction. Contact potentials are generally below 0.5 V, and the electrostatic pressure between flat surfaces is generally smaller than the van der Waals pressure.

Temporary charging can occur through the tribocharging of rubbing surfaces or through charge accumulation in insulators. The scratch drive actuator is an electrostatic actuator based on asymmetries in friction, which can exhibit electrostatic stiction failure if the insulator quality is poor.

1.1.3.4 Van Der Waals Forces

The van der Waals force between two plates is thought to be the main mechanism of permanent adhesion between hydrophobic surfaces. Figure 7 below depicts the force as a function of the distance separating two objects. When the distance between two flat surfaces is less than 20 nm, these forces dominate.

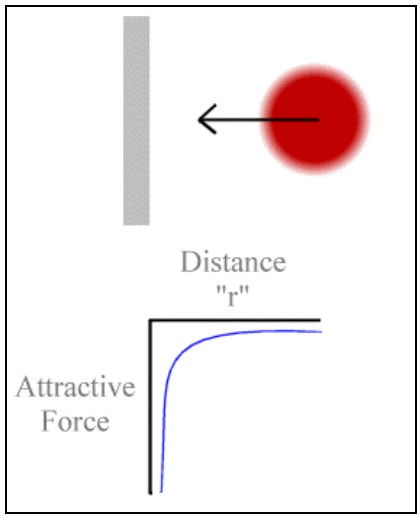

Figure 7: schematic depiction of van der Waals force as a function of separation distance

The expression for the force between the two plates is:

$$F_{vdW} = -\frac{HA}{6\pi h^3}$$

H is the Hamaker constant, and generally lies in the range of 0.4 – 4 E -19 J, and can be reduced by surface modification. The separation between the plates of area A is h in the expression.

1.1.3.5 Critical Dimensions of micromechanical structures

The forces resulting from the mechanisms discussed above can all be expressed in terms of surface energies and equated with the elastic energy stored in a cantilever. If the restoring force of

the cantilever is lower than the force applied by the stiction force, permanent adhesion will result. Since the surface area of contact determines the total force in all cases, we equate surface energies instead of forces. The expression for energy stored in a cantilever, as a function of its material properties and geometry, is given as:[13]

$$E_m = \frac{Et^3 g^2 w}{2x^3}$$

Where E is the Young's modulus, and other quantities are shown in Figure 8 below.

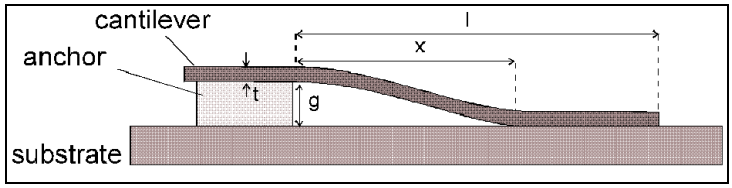

Figure 8: a cantilever beam attached to the substrate

The critical length of the beam is the length at which the restoring force can no longer overcome the forces of stiction, and can be obtained by equating the stored energy in the beam with the adhesion energy for a given area of contact.

1.1.4 Microfabrication Processing Technology to Reduce Stiction

1.1.4.1 Phase Change Release Methods

The gradual evaporation of liquids from the release etch leads to a change in meniscus geometry, and the lowest energy state of the liquid film in the case of hydrophilic films is to spread along the surfaces. This pulls released plates together irreversibly. Phase change release methods are the most popular means of combating stiction today, and they involve the use of thermodynamic properties of the materials bridging microstructures to eliminate the gradual evaporation process. Figure 9 below shows a phase diagram that will be used to explain the 3 types of phase change release methods.[14]

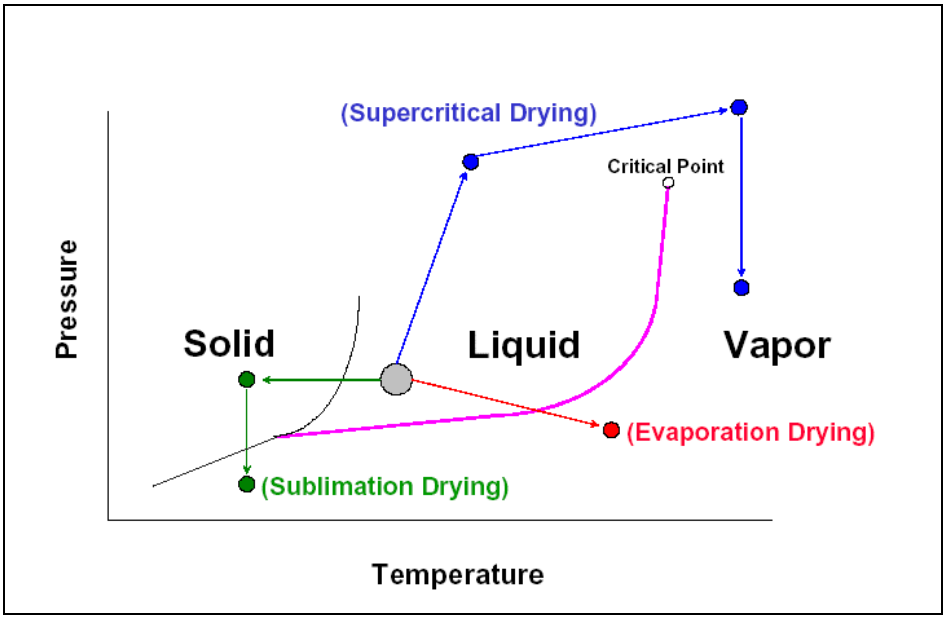

Figure 9: phase diagram showing transitions used in phase change release methods

The simplest release method involves accelerated evaporation from the liquid phase to the vapor phase. Typically, the release etchant (HF for oxides) is exchanged with a low surface tension solvent such as isopropanol. The chip is constantly immersed in solvent and fluids are exchanged, in order to prevent drying. It is then placed in an oven at an elevated temperature to allow the solvent to evaporate. Stiction can be reduced using this method, but not significantly.

Another, more effective way to release structures makes use of sublimation. In this method, the liquid that has replaced the etchant is frozen first. The solid phase of the material, typically t-butyl alcohol, does not exert any significant forces on the microstructures from its volume change. Then the pressure is lowered while the temperature is held constant in order to sublime the solid into the gas phase. This method requires a bulky temperature control and pressure control system, and is therefore not common.

The most common phase change release method is the supercritical CO2 release. Commercially available miniature supercritical CO2 units have been available for the removal of moisture from biological samples for some time. In this case, liquid CO2 replaces the etchant. The transition between liquid and vapor is sudden, as it occurs through the supercritical state. This method is quite effective and is offered as a post-processing step by most MEMS foundries; however, it does not address the problems of in-use stiction, and is often only effective for a short period of time before atmospheric moisture is adsorbed onto surfaces.

1.1.4.2 Design and Process Features

Designers can make use of structures that reduce the total area of contact between components of a microsystem. Intelligent design of structures is the most effective means of combating stiction effects, and the dimple structure has been the most popular means of reducing unwanted large surface areas of contact. In order to fabricate dimples, a patterned etch is performed on the sacrificial oxide layer beneath the structure of interest. This is a timed tech, which is designed to stop before encountering the next structural layer. Once the oxide is patterned with the dimple mask, the next layer of structural polysilicon is conformally deposited. The resulting structure is shown in Figure 10 below.

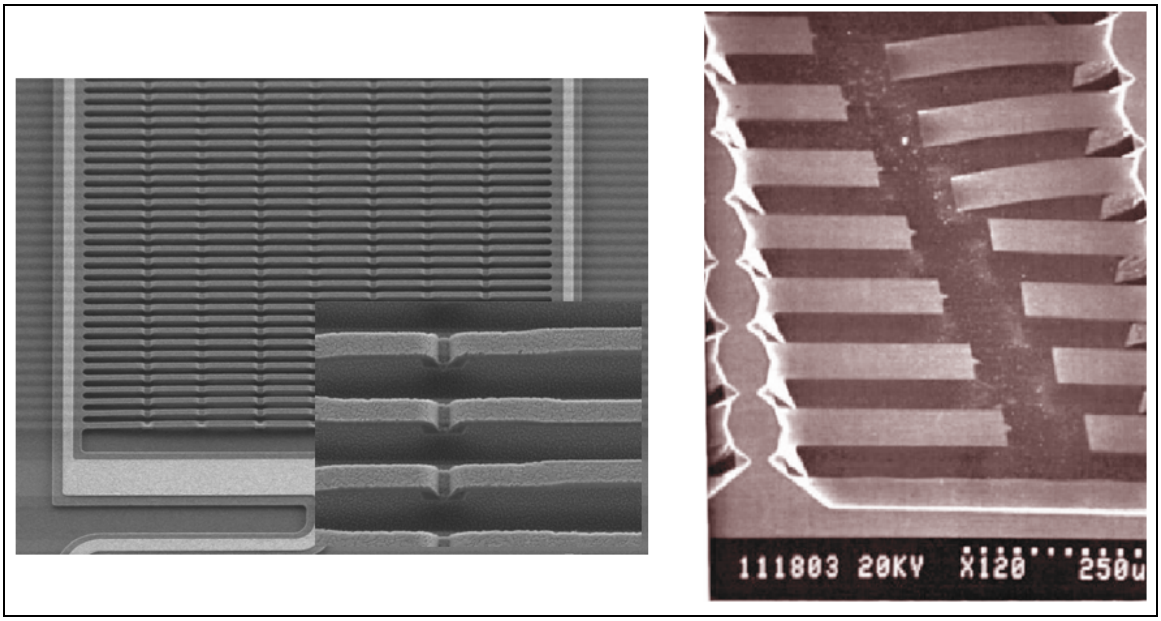

Figure 10: SEM of Dimples (left) and anti-stiction structures (right) used to lower stiction effects.

If the option of adding dimples is not available, geometries such as anti-stiction tabs can be used to reduce the likelihood of stiction.[15] The addition of protrusions with convex corners increases the total energy of the meniscus at these points and forces the liquid to dry in such a way that stiction is prevented. For instance, in the case of the singly anchored beam in Figure 10, liquid typically dries from the base to the tip, forming a disconnected droplet which bridges the structures. By placing a convex corner at the tip, the liquid is forced to dry from the tip to the base, since the meniscus geometry at the tip is not geometrically favorable. In the case of doubly anchored beams, the designer can place tabs near the center of the structure to prevent a droplet from bridging at the

weakest point of the beam. These techniques are quite effective, and are commonly neglected in the early phases of design, which results in the failure of initial prototypes.

1.1.4.3 Plasma deposition of Teflon-like Films

The use of PECVD thin films of polymer materials has been shown to reduce stiction and wear of sliding contacts in MEMS.[16] When a fluorocarbon gas is placed in a plasma reactor, the gas is fractured into a mixture of ions, excited molecules and radicals. Depending on the feed gases, substrates exposed to the plasma can be etched or have a polymeric film deposited on them. Polymerized tetrafluoroethylene {pTFE, $(CF_2)_x$} can be grown by controlling the fluorine-to-carbon ratio in the feed gas.

If the substrate is placed directly on the cathode or anode, ionized species will be accelerated from the plasma to the substrate and will impinge normal to the surface. This results in anisotropic deposition, in a line of sight fashion onto the wafer. To make the field grow conformally and penetrate beneath structures where stiction is likely to occur, the substrate needs to be placed in a shielded, field-free zone.[17] The modified PECVD setup shown in Figure 11 accomplishes conformal deposition by placing a ground shield between the anode and cathode, where field lines terminate.

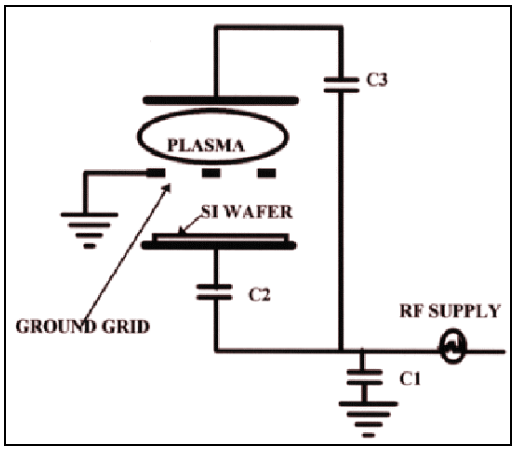

Figure 11: modified PECVD setup to achieve conformal deposition

1.1.4.4 Self-Assembled monolayers

An area of research that is currently being intensely investigated as an alternative means of stiction reduction is the conformal growth of self assembled monolayers (SAM) with desirable properties on substrates.[18] The process of SAM growth involves several steps, starting with bulk

Chapter 1
Introduction

As early as 1965, when Moore's law was first proposed, it was known that integrated circuits would follow an aggressive miniaturization trend with the "complexity for minimum component costs increasing at a rate of roughly a factor of two per year."[1] This bold prediction has been closely monitored with respect to microprocessors and has been remarkably accurate for the past four decades. In retrospect, the many technological breakthroughs that were required for the continued validity of Moore's law could not have been known a priori; nevertheless, the trend has continued and has even been used to describe progress in other technologies.

It was not until the early 1980's that silicon, which had already revolutionized the way we think about electronics, had begun to alter conventional perceptions of miniature mechanical devices and components. In 1982, the first review paper on the field, "Silicon as a mechanical material," was published in *Proceedings of the IEEE.* [2] "The basis of micromechanics is that silicon, in conjunction with its conventional role as an electronic material, and taking advantage of an already advanced microfabrication technology, can also be exploited as a high-precision high-strength high-reliability mechanical material..."[3] The microelectronics industry's mature micron-scale lithography, thin film deposition, ion implantation, and etching technologies applied to micromechanics had given rise to "Micromachines" in Japan, "Microsystems Technology" (MST) in Europe and Microelectromechanical Systems (MEMS) in North America. The applications of this research range from optical signal processing and RF devices to silicon valves and pumps (microfluidics) to nanopositioning (hard drives, scanning probe microscopes) to inertial sensors and inkjet print heads and more. Thus the field has a multidisciplinary nature that includes: silicon microfabrication technology, mechanical design, material science, tribology, control theory, metrology, robotics, optics, electromagnetics and many other areas. Despite the wide range of applications and the complex multifaceted nature of the field, several truly fascinating breakthroughs have occurred in order to ensure a rate of progress that is consistent with Moore's Law.

The focus of this work involves optical and RF applications of novel microactuation and self-assembly techniques in MEMS. The scaling of physical forces into the micro domain is favorably used to design several types of actuators that can provide large forces and large static displacements at low operation voltages. A self-assembly method based on thermally induced localized plastic deformation of microstructures has been developed to obtain truly three-dimensional structures from

a planar fabrication process. RF applications include variable discrete components such as capacitors and inductors as well as tunable coupling circuits. Optical applications include scanning micromirrors with large scan angles (>90 degrees), low operation voltages (<10 Volts), and multiple degrees of freedom. One and two-dimensional periodic structures with variable periods and orientations (with respect to an incident wave) are investigated as well, and analyzed using phased array concepts of electromagnetic theory. Throughout the research, permanent tuning via plastic deformation and power-off latching techniques are used in order to demonstrate that the optical and RF devices can exhibit zero quiescent power consumption once their geometry is set.

1.1 General Considerations

1.1.1 Microfabrication Processes

Silicon micromachining can be broadly categorized into bulk micromachining and surface micromachining (Figure 1). The former involves etching structures into the substrate (removal of material), and the latter involves the deposition and subsequent etching of thin films of sacrificial and structural materials (additive processes). Although the details of processing are beyond the scope of this work, some of the popular methods are briefly discussed here. Several texts have been published with exhaustive surveys of MEMS and silicon processing technology, some of which are included in the references.[4,2,5]

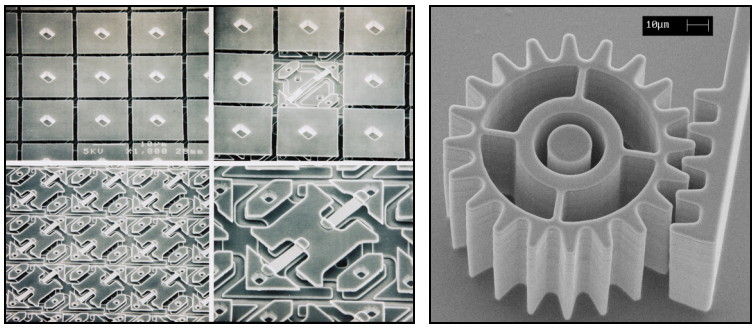

Figure 1: Surface micromachining (left) of Texas Instruments Digital Micromirror Device and bulk micromachining (right) of a silicon gear.

Most of the work presented in this thesis involves surface micromachined devices fabricated by the MUMPs (Multi-User MEMS Process), which is described further below.

1.1.1.1 Bulk Micromachining Process Technology

Several methods have been used for the removal of material from the bulk of the wafer. Wet or dry etchants are selected based on selectivity to etch masks, availability of etch stop methods, etch rate, cost, etch geometry, and many other criteria.**Error! Bookmark not defined.** The most common isotropic method for wet etching of silicon is HNA, a mixture of hydrofluoric acid (HF), nitric acid (HNO_3), and acetic acid (CH_3COOH). This method results in a spherical etch geometry when agitation is used. The most common anisotropic wet etchant is KOH, which etches preferentially along the <100> surface of the wafer, leaving the <111> surfaces exposed. When high aspect ratios are desired, dry etching methods are used, such as DRIE (deep reactive ion etching). High aspect ratios can also be obtained with thick photoresists such as SU8 and molding/electroplating processes such as LIGA for metallic materials.

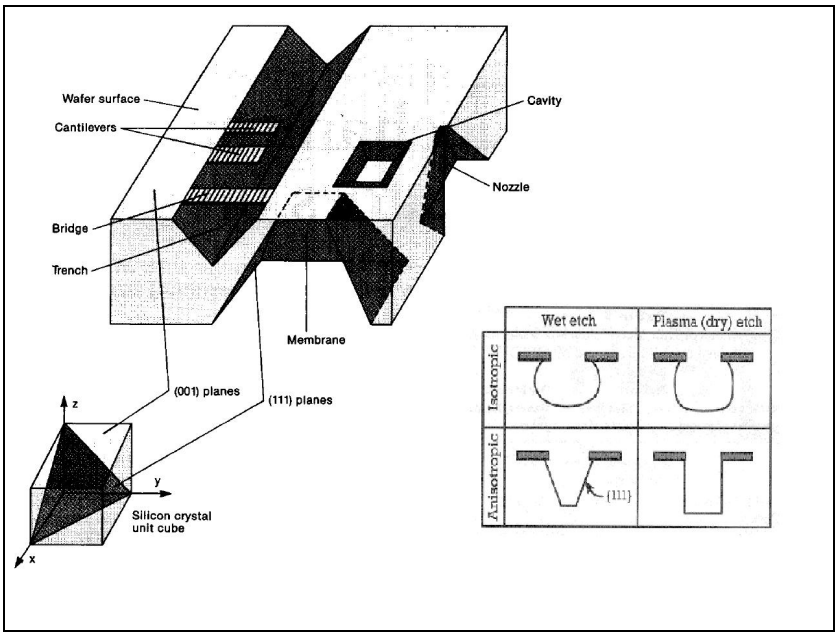

Figure 2: pictorial depiction of bulk micromachining techniques

1.1.1.2 Surface Micromachining Process Technology

Surface micromachining consists of the deposition, patterning, etching and release of thin films of material.[6] Techniques that fall under this category are sometimes called additive processes since material is added to the surface of the substrate. Unlike bulk micromachining, there is no removal of material from the substrate. In order to obtain functional electromechanical microsystems, both insulating and conductive films are required. Finally, in order to create free-standing

microstructures, sacrificial layers are used. These layers are deposited between mechanical layers, and removed near the end of processing.

Low pressure chemical vapor deposition (LPCVD), plasma enhanced chemical vapor deposition (PECVD), evaporation, sputtering, electroplating, epitaxial growth, and spin-coating are among the techniques used to deposit materials onto the surface of wafers.

Polysilicon is the most common structural material in surface micromachining, and is typically doped heavily in order to ensure good conductivity. There is no requirement for patterned doping, since a uniform doping level is desirable throughout the film. In some cases, a film of PSG (phosophosilicate glass) is used as a sacrificial layer and as a dopant – a high temperature anneal serves as a doping step (via diffusion) and as a stress reduction step.

Silicon nitride is extremely useful as an insulating material, and it can serve as a passivation layer, a capacitor dielectric, a structural material, and as a mask for etching or for selective oxidation of Si. This material is most commonly deposited using LPCVD as well, to obtain low stress, stoichiometric film quality. Several highly selective etch chemistries exist which allow the use of nitrides as an etch stop for oxides and polysilicon. LPCVD is preferred for nitride deposition over PECVD, since PECVD films are not stoichiometric and incorporate hydrogen, which affects etch selectivity.

Silicon dioxide is certainly the most commonly available dielectric in silicon fabrication laboratories. In surface micromachining, it often serves as a sacrificial layer and is commonly deposited using LPCVD or PECVD as opposed to thermal oxidation, which is more common in IC's. PSG (phosphosilicate glass, phosphorus doped) and BSG (borosilicate glass, boron-doped) can serve as a sacrificial layer and can be used to dope underlying layers of polysilicon during a thermal anneal process. BPSG (doped with both boron and phosphorus) is a low temperature oxide, and has excellent low-temperature reflow properties, which makes it suitable for use in CMP (chemical mechanical planarization) steps.

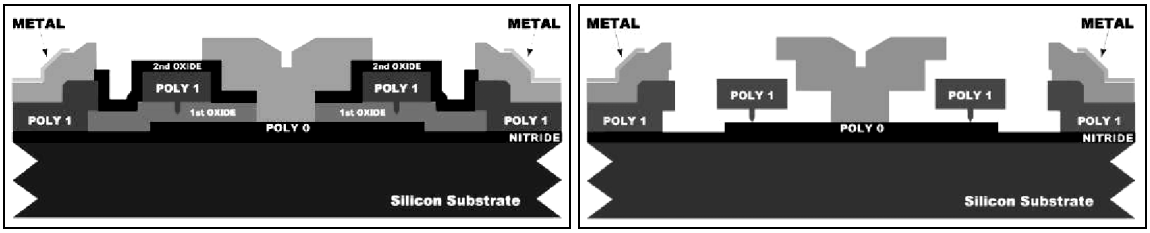

Figure 3: cutaway diagrams of the MUMPs process, before (left) and after (right) release.

By alternating layers of these and other materials (eg. polycristalline diamond, silicon carbide), 2 ½ dimensional structures of insulating, conducting, and sacrificial layers can be manufactured. After the release step in which the sacrificial layers are removed, these structures are become free standing electromechanical microsystems, which can be entirely removed from the substrate in some cases. As an example of a commonly used surface micromachining process, Figure 3 shows cutaway diagrams of the MUMPs (multi-user MEMS processes) process before and after release.

As shown in

Figure 3, the MUMPs process contains a nitride layer to electrically isolate polysilicon structures from one another. There is one layer of polysilicon (poly0) deposited directly onto the substrate, and 2 released poly layers (poly 1 and poly 2). Sacrificial oxides are deposited between all the structural layers. Finally, an evaporated metal layer is deposited and patterned using the liftoff technique.

There are two features in this diagram that are worth noting. First of all, in the top diagram, all the space occupied by oxide is replaced by fluids during the release process. These fluids exert capillary forces when they evaporate, and this can lead to stiction effects. Another feature is the dimple layer, which can be seen as protrusions from the bottom of the poly1 layer. The dimples prevent a large surface area of contact between poly1 and the layer below it. Finally, it should be noted that after the release process, mechanically free structures will no longer be constrained by oxide, and should be constrained by the other mechanical layers. For instance, in the case of the diagram above, the released poly 1 falls onto poly0, and is constrained from floating away in the etchant liquid by the poly 2 overhang above it. Special care should be taken to ensure that the constraining layers do not come into contact with the released parts with a large surface area of contact.

1.1.2 Scaling of Systems

A fundamental issue in microdynamics is the scaling of physical properties into the micro domain. [7] When a system is scaled down by a factor of 100, its volume and mass and hence the inertial and gravitational forces decrease by a factor of $100^3 = 1\ 000\ 000$. In many of the actuator designs that are discussed here, long singly-clamped beams with relatively small aspect ratios are used. In a scaled-up system, these beams would sag and inertial forces would make the design highly impractical; however, these forces are rarely a consideration in the design of microactuators, due to the small mass and high stiffness of the materials used. The thermodynamics of a scaled down

system are affected by this dramatic reduction in volume and mass as well. Since the thermal mass is reduced by a factor 1000 000 in this example, the thermal time constant for a beam is quite small. This makes it possible to thermally cycle a beam at several kHz in many cases. Electrothermal actuators of various geometries and materials are used throughout the research presented in this thesis. Typically, these actuators are based on Joule heating and can provide high static displacements and large forces at low operating voltages if properly designed.

Forces that scale as a function of area, such as electrostatic attraction, will decrease by a factor of only 10 000 when the system is scaled down 100 times. Thus, the ratio of electrostatic to inertial forces increases by a factor of 100. Comb drives, parallel plate actuators and scratch drive actuators are examples of practical electrostatic actuators at the micron scale.

The forces of surface tension scale with the linear dimension of the system and become large relative to other forces. Hence, the phenomenon of stiction during the release process of the MEMS becomes significant.[8]

1.1.3 Origins of Stiction

Stiction can arise during the sacrificial release process or while a device is in operation. The causes of adhesion are similar in both cases; however, the remedy for in use failure is more involved since it involves lubrication at the micron scale, an area of tribology that has not yet been thoroughly explored. In this section, the four most common sources of stiction will be discussed. Capillary forces may arise if the liquids used in the etching process evaporate slowly, and the reduced volume of the fluid "pulls" microstructures together. Hydrogen bridging results when thin films of moisture are adsorbed on hydrophilic surfaces, and O-H bonds form between the layers. Electrostatic forces from stored charge can arise during operation of electrostatic devices, or when materials with different work functions come into intimate contact. The van der Waals dispersion forces between two bodies are caused by mutual electric interaction of the induced dipoles in the two bodies. This is the dominant adhesion mechanism for hydrophobic surfaces.

1.1.3.1 Capillary Forces

A thin liquid layer between two solid plates can work as an adhesive. If the contact angle between liquid and solid is less than 90 degrees, the pressure inside the liquid drop will be lower than outside. This is a function of the hydrophobicity of the solid surface. In Figure 4, the geometry of a

water droplet on an oxide-coated Si (hydrophilic) substrate is compared to its geometry on a fluorinated SAM-coated Si (hydrophobic) substrate.[9]

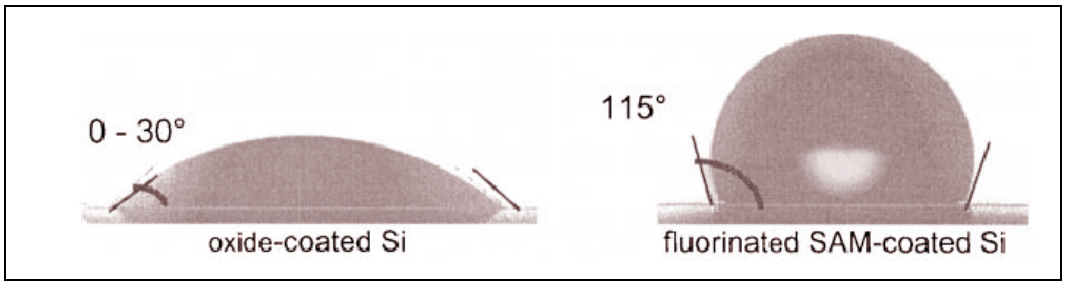

Figure 4: water droplet geometries on hydrophilic and hydrophobic surfaces

In the case of hydrophilic surfaces with a thin layer of liquid bridging them, the liquid acts as an adhesive. This situation is depicted below, in Figure 5. [9]

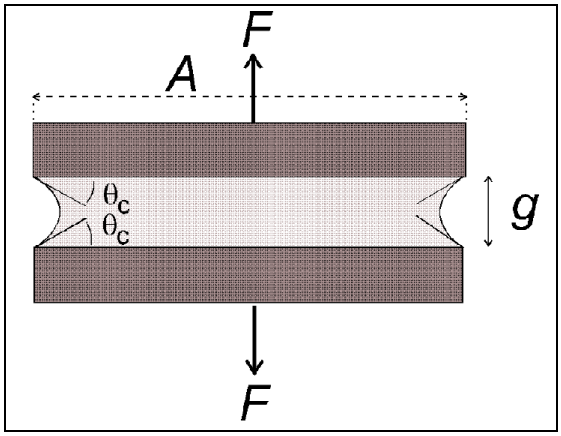

Figure 5: A thin layer of liquid acting as an adhesive between two plates

The pressure difference at the liquid-air interface is given by the Laplace equation[10]:

$$\Delta p_{la} = \frac{\gamma_{la}}{r}$$

where γ_{la} is the surface tension of the liquid - air interface and r is the radius of curvature of the meniscus :

$$r = -g / 2\cos\theta_c$$

In equilibrium, an external force can be applied to counteract the liquid bridging force, as shown in Figure 5. This force can be calculated as follows:[11]

$$F = -\Delta p_{la} A = \frac{2A\gamma_{la}\cos\theta_c}{g}$$

where A is the wetted area, and other quantities are drawn in the figure. These forces are on the same order of magnitude as the restoring forces of the thin beams of polysilicon that are widely used as support structures or in actuators in surface micromachined devices.

1.1.3.2 Hydrogen bridging

Hydrophilic silicon surfaces under atmospheric conditions contain adsorbed water layers.[12] When two hydrated surfaces come into close contact, hydrogen bonds may form between oxygen atoms and hydrogen atoms of the adsorbed water layers, as shown in Figure 6. The adhesion energies which have been reported for this process range from 60 to 270 mJ/m^2. This is high enough to permanently hold micromechanical plates together. The proposed mechanism for permanent stiction failure with hydrophilic surfaces therefore involves bringing two surfaces together by liquid bridging or otherwise, and permanently bonding them with hydrogen bridging forces.

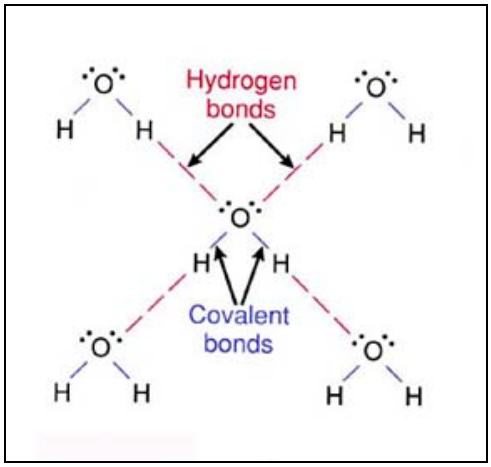

Figure 6: covalent bonding in water which leads to hydrogen bridging

1.1.3.3 Electrostatic Forces

Electrostatic forces can arise from a difference in work functions or from charging of opposed surfaces. A difference in work functions will lead to an electrical double layer by a net transfer of electrons from one layer to another, similar to the cause of band bending that is observed

to occur in a Schottky junction. Contact potentials are generally below 0.5 V, and the electrostatic pressure between flat surfaces is generally smaller than the van der Waals pressure.

Temporary charging can occur through the tribocharging of rubbing surfaces or through charge accumulation in insulators. The scratch drive actuator is an electrostatic actuator based on asymmetries in friction, which can exhibit electrostatic stiction failure if the insulator quality is poor.

1.1.3.4 Van Der Waals Forces

The van der Waals force between two plates is thought to be the main mechanism of permanent adhesion between hydrophobic surfaces. Figure 7 below depicts the force as a function of the distance separating two objects. When the distance between two flat surfaces is less than 20 nm, these forces dominate.

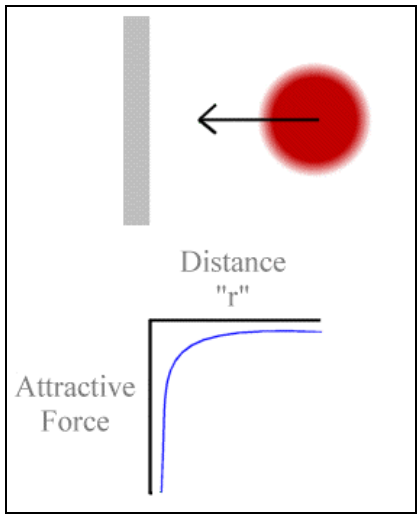

Figure 7: schematic depiction of van der Waals force as a function of separation distance

The expression for the force between the two plates is:

$$F_{vdW} = -\frac{HA}{6\pi h^3}$$

H is the Hamaker constant, and generally lies in the range of 0.4 – 4 E -19 J, and can be reduced by surface modification. The separation between the plates of area A is h in the expression.

1.1.3.5 Critical Dimensions of micromechanical structures

The forces resulting from the mechanisms discussed above can all be expressed in terms of surface energies and equated with the elastic energy stored in a cantilever. If the restoring force of

the cantilever is lower than the force applied by the stiction force, permanent adhesion will result. Since the surface area of contact determines the total force in all cases, we equate surface energies instead of forces. The expression for energy stored in a cantilever, as a function of its material properties and geometry, is given as:[13]

$$E_m = \frac{Et^3 g^2 w}{2x^3}$$

Where E is the Young's modulus, and other quantities are shown in Figure 8 below.

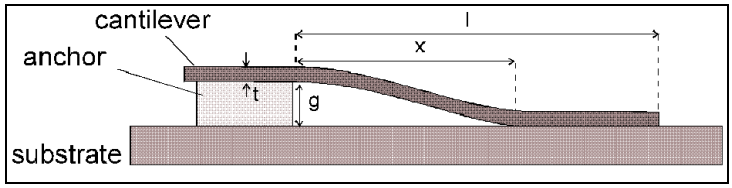

Figure 8: a cantilever beam attached to the substrate

The critical length of the beam is the length at which the restoring force can no longer overcome the forces of stiction, and can be obtained by equating the stored energy in the beam with the adhesion energy for a given area of contact.

1.1.4 Microfabrication Processing Technology to Reduce Stiction

1.1.4.1 Phase Change Release Methods

The gradual evaporation of liquids from the release etch leads to a change in meniscus geometry, and the lowest energy state of the liquid film in the case of hydrophilic films is to spread along the surfaces. This pulls released plates together irreversibly. Phase change release methods are the most popular means of combating stiction today, and they involve the use of thermodynamic properties of the materials bridging microstructures to eliminate the gradual evaporation process. Figure 9 below shows a phase diagram that will be used to explain the 3 types of phase change release methods.[14]

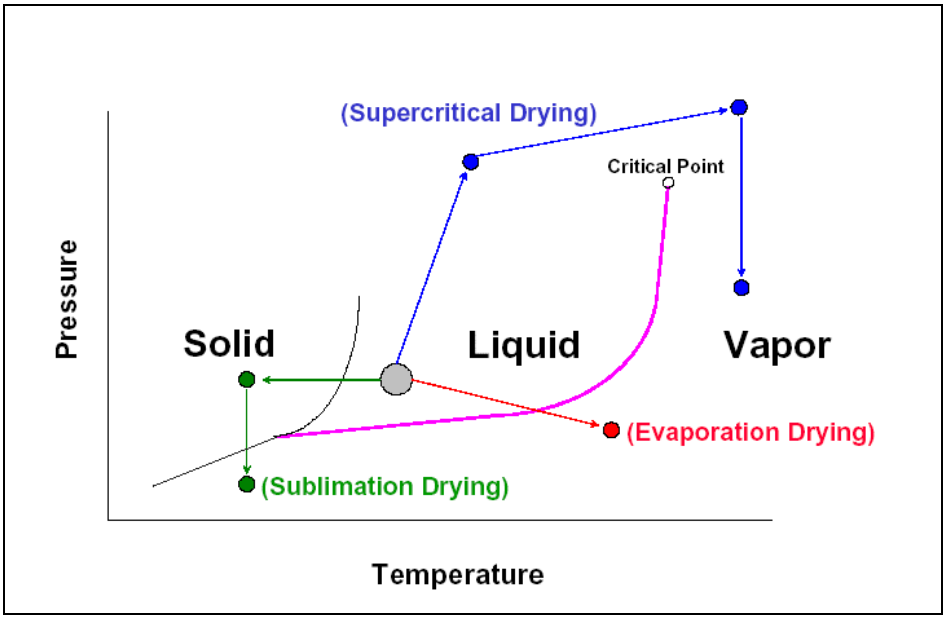

Figure 9: phase diagram showing transitions used in phase change release methods

The simplest release method involves accelerated evaporation from the liquid phase to the vapor phase. Typically, the release etchant (HF for oxides) is exchanged with a low surface tension solvent such as isopropanol. The chip is constantly immersed in solvent and fluids are exchanged, in order to prevent drying. It is then placed in an oven at an elevated temperature to allow the solvent to evaporate. Stiction can be reduced using this method, but not significantly.

Another, more effective way to release structures makes use of sublimation. In this method, the liquid that has replaced the etchant is frozen first. The solid phase of the material, typically t-butyl alcohol, does not exert any significant forces on the microstructures from its volume change. Then the pressure is lowered while the temperature is held constant in order to sublime the solid into the gas phase. This method requires a bulky temperature control and pressure control system, and is therefore not common.

The most common phase change release method is the supercritical CO2 release. Commercially available miniature supercritical CO2 units have been available for the removal of moisture from biological samples for some time. In this case, liquid CO2 replaces the etchant. The transition between liquid and vapor is sudden, as it occurs through the supercritical state. This method is quite effective and is offered as a post-processing step by most MEMS foundries; however, it does not address the problems of in-use stiction, and is often only effective for a short period of time before atmospheric moisture is adsorbed onto surfaces.

1.1.4.2 Design and Process Features

Designers can make use of structures that reduce the total area of contact between components of a microsystem. Intelligent design of structures is the most effective means of combating stiction effects, and the dimple structure has been the most popular means of reducing unwanted large surface areas of contact. In order to fabricate dimples, a patterned etch is performed on the sacrificial oxide layer beneath the structure of interest. This is a timed tech, which is designed to stop before encountering the next structural layer. Once the oxide is patterned with the dimple mask, the next layer of structural polysilicon is conformally deposited. The resulting structure is shown in Figure 10 below.

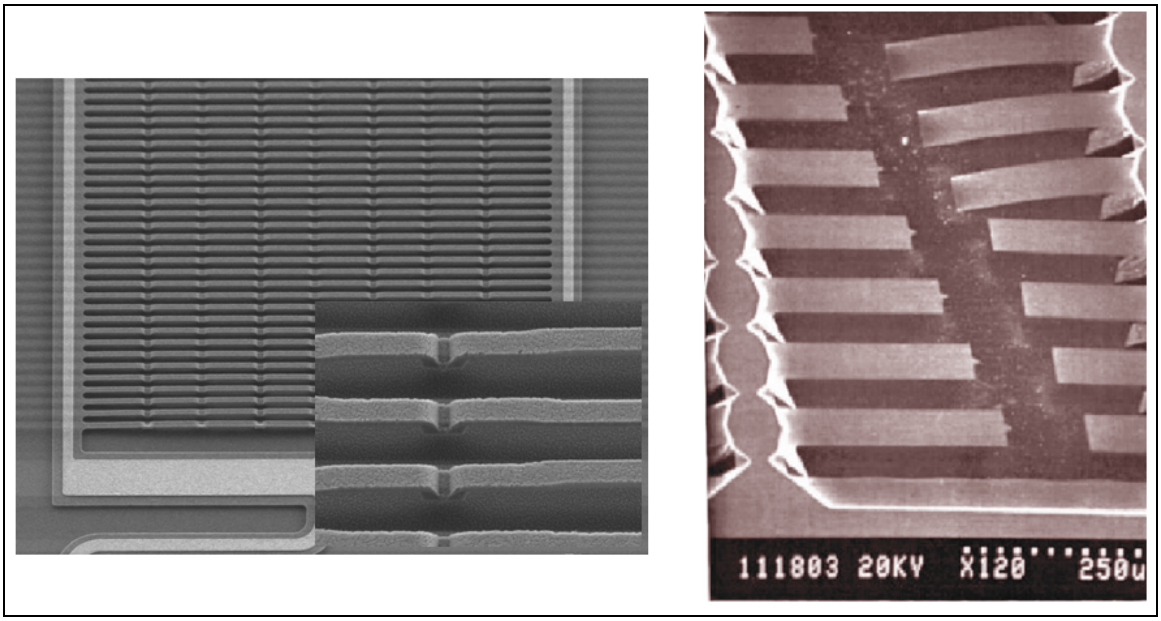

Figure 10: SEM of Dimples (left) and anti-stiction structures (right) used to lower stiction effects.

If the option of adding dimples is not available, geometries such as anti-stiction tabs can be used to reduce the likelihood of stiction.[15] The addition of protrusions with convex corners increases the total energy of the meniscus at these points and forces the liquid to dry in such a way that stiction is prevented. For instance, in the case of the singly anchored beam in Figure 10, liquid typically dries from the base to the tip, forming a disconnected droplet which bridges the structures. By placing a convex corner at the tip, the liquid is forced to dry from the tip to the base, since the meniscus geometry at the tip is not geometrically favorable. In the case of doubly anchored beams, the designer can place tabs near the center of the structure to prevent a droplet from bridging at the

weakest point of the beam. These techniques are quite effective, and are commonly neglected in the early phases of design, which results in the failure of initial prototypes.

1.1.4.3 Plasma deposition of Teflon-like Films

The use of PECVD thin films of polymer materials has been shown to reduce stiction and wear of sliding contacts in MEMS.[16] When a fluorocarbon gas is placed in a plasma reactor, the gas is fractured into a mixture of ions, excited molecules and radicals. Depending on the feed gases, substrates exposed to the plasma can be etched or have a polymeric film deposited on them. Polymerized tetrafluoroethylene {pTFE, $(CF_2)_x$} can be grown by controlling the fluorine-to-carbon ratio in the feed gas.

If the substrate is placed directly on the cathode or anode, ionized species will be accelerated from the plasma to the substrate and will impinge normal to the surface. This results in anisotropic deposition, in a line of sight fashion onto the wafer. To make the field grow conformally and penetrate beneath structures where stiction is likely to occur, the substrate needs to be placed in a shielded, field-free zone.[17] The modified PECVD setup shown in Figure 11 accomplishes conformal deposition by placing a ground shield between the anode and cathode, where field lines terminate.

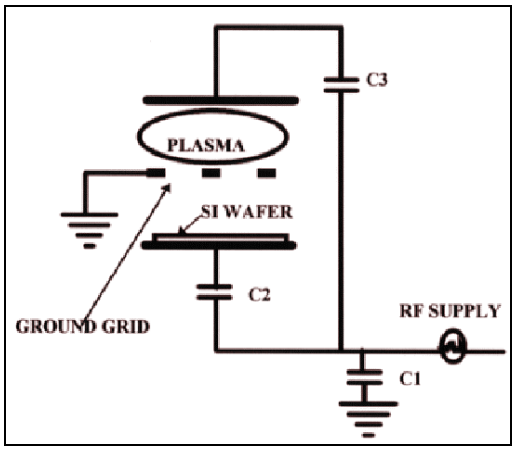

Figure 11: modified PECVD setup to achieve conformal deposition

1.1.4.4 Self-Assembled monolayers

An area of research that is currently being intensely investigated as an alternative means of stiction reduction is the conformal growth of self assembled monolayers (SAM) with desirable properties on substrates.[18] The process of SAM growth involves several steps, starting with bulk

solution transport and surface adsorption and continuing with the two-dimensional organization on the substrate of interest. The latter process can often be described using two-dimensional nucleation and growth models, similar to those used in epitaxy.

Hexamethyldisilane (HMDS) is a commonly used SAM that enhances the adhesion properties of photoresist.[2] Its adhesion mechanisms have been studied and serve here as an example for the formation of SAMs. The molecular structure of HMDS is:

$$(CH_3)_3 - Si - NH - Si - (CH_3)_3 \text{ or } [(CH_3)_3 Si]_2 NH$$

When the molecule is present in solution, the hydroxyl groups on the silicon surface are first removed:

$$2SiOH + [(CH_3)_3 Si]_2 NH \rightarrow 2SiOSi(CH_3)_3\{\text{bound to the surface}\} + NH_3$$

The surface moisture is removed by the formation of hexamethyldisilane and ammonia, both of which evaporate:

$$H_2O + [(CH_3)_3 Si]_2 NH \rightarrow [(CH_3)_3 Si]_2 O + NH_3$$

The removal of water results in superior adhesion.

Some common molecules used in the SAM formation of stiction-reducing films are Octadecyltrichlorosilane (OTS) and perfluorodecyltrichlorosilane (FDTS); several variants and combinations thereof are being investigated.[19,9,20]

The formation of an OTS SAM is shown in Figure 12 below.

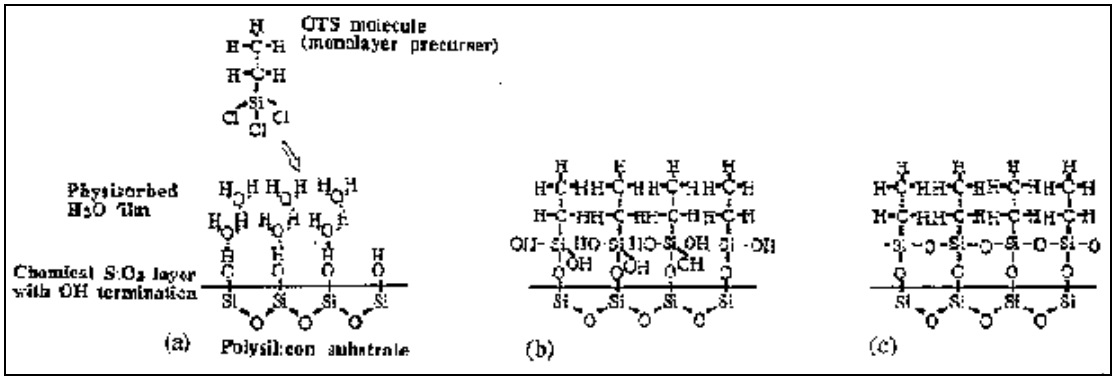

Figure 12: formation of OTS SAM on polysilicon substrate

The process begins with the liquid phase application of the OTS molecule, and a hydrolysis step similar to that of HMDS described above (a). This step is immediately followed by molecule adsorption through the formation of Si-O-Si siloxane bonds (b). Finally, cross-linkage occurs through covalent bonding between molecules, stabilizing the monolayer (c).

The properties of OTS and FDTS films are suitable for MEMS applications. SAMs and Teflon-like coatings are the only methods which have been successfully used to reduce in-use stiction, and SAMs have the advantage that they require no exotic processing equipment, as they are applied in solution in atmospheric conditions. Currently, the films are stable up to 400 C, which is acceptable for most MEMS applications; however, thermal actuators are known to operate at over 500 C for part of a switching cycle, and so films with superior thermal stability are under investigation.

Chapter 2
Literature Review

This section contains a review of published work in micromechanics, RF MEMS, and Optical MEMS. More specifically, actuation methods based on favorable scaling of physical forces are discussed and compared. Self-assembly methods based on various principles are discussed as well. In the area of RF MEMS, discrete components such as variable capacitors and inductors will be reviewed and compared. Optical MEMS devices reviewed here include switched and scanning micromirrors developed by various groups for display, imaging, and optical switching applications, as well as variable periodic structures.

2.1 Micro Actuation Techniques

Actuators enable MEMS to perform physical functions and interact with their environments by altering geometries at the micron scale. In most cases, an electrical input is converted to a non-electrical output signal in the radiant, magnetic, thermal, mechanical, or chemical domains. Reviews of existing actuator techniques have discussed the driving principles and mechanisms for actuators.[21,7,22] The organization of these reviews generally focuses on the classification of a large number of exhaustively surveyed actuation mechanisms according to underlying physical principles, material properties or fabrication methods. However, for a discussion of design details of the actuators, the reader is typically referred to original publications that may contain design parameters and performance data.

In this section the specific device geometries of several types of commonly used actuators are discussed on a case-by-case basis. The underlying physics of the specific embodiments is reviewed and the overall performance of the actuators is evaluated and compared. Actuators that require exotic processing or that have not been encountered in the course of this research are not included. In some cases, actuators from the literature were fabricated and characterized by the author in order to gain some insight into reliability issues and to obtain data that was not made available in publications. Common electrothermal methods of actuation include bimorph actuators (single material [23], bi-material [27], unidirectional and bidirectional structures are discussed), bent-beam actuators [24,25,26] topology optimized structures, and out-of-plane actuators [27,28]. Actuators based on electrostatic principles include scratch drive actuators (SDA's) [29,30] comb drives [31,32] parallel plate designs [33,34] membrane deformation actuators[35,36] S-shape flexures [37], distributed force actuators [38], and

torsional/gimbaled actuators [39]. Impact drive mechanisms [40,41,42], shape memory alloy actuators [43,44] and electromagnetic actuators [45,46] have been implemented at micron scales as well.

2.1.1 Electrothermal

2.1.1.1 U-Shaped "Heatuator" or Single-Material Thermal Bimorph Actuators

The U-Shaped thermal bimorph actuator was one of the first actuators designed in a surface micromachining process that makes use of Joule heating in order to produce mechanical deflections. Figure 13 below is an SEM image of a typical "heatuator" design with the geometrical features

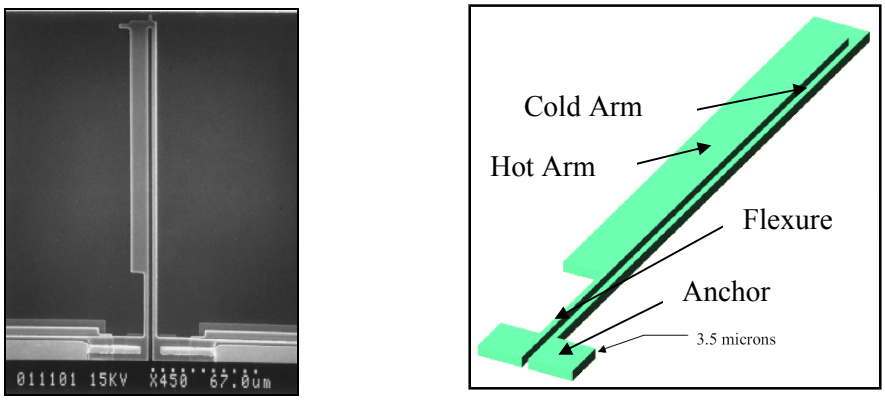

Figure 13 SEM picture (left) and solid model (right) of u-shaped thermal bimorph actuator.

indicated in a solid model. This version of the actuator is "stacked," which means that the Poly1 and Poly2 layers in the MUMPs process description are etched in one step, increasing the thickness of the device to 3.5 microns. The out-of-plane stiffness of stacked structures is higher, the maximum power handling capability is increased, the amplitude of the deflection is greater, and they are generally more robust as well (higher burnout power, lower probability of stiction failure, etc.).

The operating principle of this actuator is thermal expansion via Joule heating. Although thermal expansion is a powerful force, a single material actuator based solely on the expansion of a single beam would produce small deflections with respect to the beam length. In this design, a voltage is placed between the two anchored pads of the device. The resultant current that passes through the device preferentially heats the "hot arm" since its lower cross sectional area results in a higher current density. The "cold arm" therefore experiences a lower thermal expansion, and the tip of the actuator deflects laterally towards the cold arm side, as the arms are joined at the free end. The purpose of the flexure is to increase the compliance of the device to ensure an adequate displacement. The optimal length of the flexure has been determined empirically and through FEA (Finite Element Analysis) to

be approximately 15% of the hot arm length. Thus, the 200 um actuator in Figure 13 has a 30 um flexure. Analytical modeling of these actuators based on calculations of expansion forces and bending moments have been published. [47]

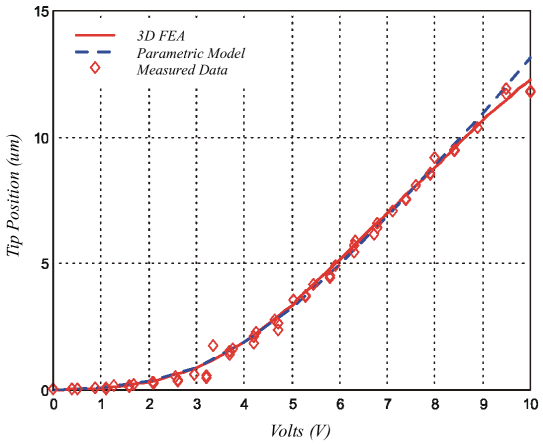

Figure 14: measured and simulated data for u-shaped thermal bimorph

The measurements in Figure 14 were taken with a UMECH MEMS Motion Analyzer,[48] a stroboscopic image processing and analysis tool with a specified in-plane resolution of 10 nm under optimal conditions. Vacuum measurements have been taken in order to experimentally quantify the contributions of air damping and thermal convection. [49]

The parametric model based on a 1-D beam element and the 3D FEA methods are discussed in further detail in the actuator design section of this thesis. Figure 14 above shows a maximum measured deflection of approximately 12.5 um with a 10-volt input, which is sufficient for many applications.

The strengths of this design are that low voltages (IC compatible) are required, static displacements can be provided (as opposed to resonant displacements that are more common in electrostatic devices), moderate forces can be exerted, and the overall footprint of the device is small. Heatuators are relatively insensitive to ambient temperature, since any isothermal distribution results in zero displacement (the *difference* in the temperature between hot and cold arms causes the deflection). Furthermore, devices can be "ganged" in order to increase force output. Many electrothermal actuator geometries share some of these advantages.

The disadvantages of this design are numerous; the cold arm is in the current path and so Joule heating leads to unwanted thermal expansion in it (this is the largest contributor to the inefficiency of the design); the deflections produced are moderate; the low resistance of the device

gives rise to large currents even at moderate voltages, which increases the power consumption and makes thicker versions of the actuator impractical (100 um DRIE versions of the actuator can consume amperes of current!); the operating temperature is high (up to 800K).
Several attempts have been made to remedy the shortcomings of this design.

2.1.1.2 Bi-directional Electrothermal Actuator

Bi-directional devices such as the device shown in Figure 15 [49] designed by the author have been shown to work. By selecting the center arm and either side arm to conduct current, the direction of actuation can be controlled. Furthermore, the thermal expansion is contained within the 2 hot arms, and the cold arm remains isolated from the current path. Although this device is shown to have a large resonant displacement in vacuum, the static displacements are less impressive. This is partially due to the thermal conduction into the cold arm, and the increased stiffness due to the third anchored beam in the design. Figure 16 below indicates the reduced static deflections measured in the same UMECH test station and compared to the same parametric model and 3D FEA methods. Note that the so the tip position can undergo the indicated deflection in both directions, doubling the amplitude of the motion indicated in the graph.

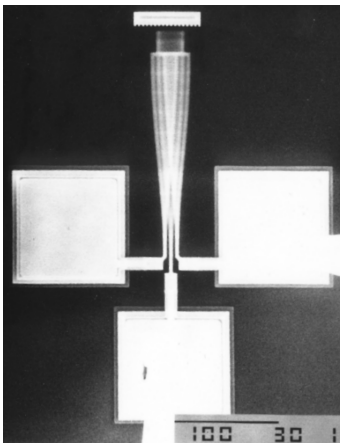

Figure 15: bi-directional actuator in resonance with 30 um deflection amplitude

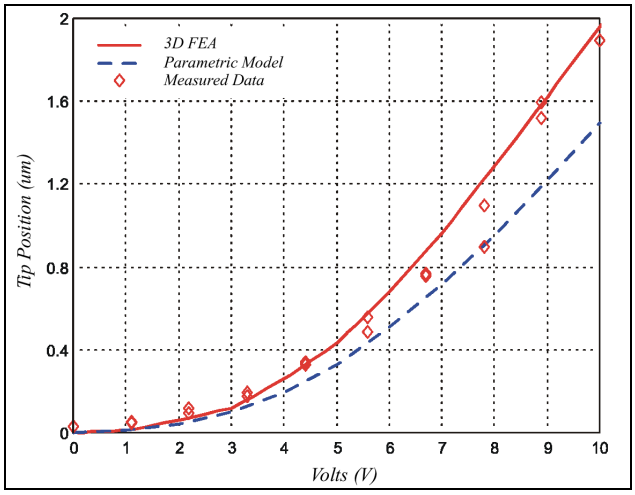

Figure 16: measured and simulated data for bi-directional actuator

Double-hot-arm devices such as the device shown in Figure 17[47] eliminate the current in the cold arm as well, although thermal conduction still contributes to some expansion of the hot arm. The tradeoff is the increased stiffness of the device due to the third beam in the geometry. Although the

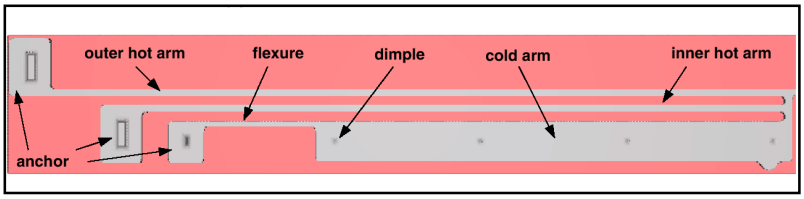

Figure 17: solid model of 2-hot-arm actuator

footprint of this device is larger than that of the traditional heatuator described above, the achieved deflection is comparable. The stiffness is higher, which implies a higher force with a similar deflection, resulting in a greater work output. The geometry of the cold arm in this case improves the performance of the actuator as compared to the bi-directional version.

2.1.1.3 Bent Beam Actuators

The bent beam actuator design has been used by many groups for a variety of applications such as micro-rotary engines, micro tweezers, and micro positioning systems. The basic geometry can be used to create small, high force rectilinear deflections. It can be cascaded in a series mechanical configuration to amplify the displacement or in a parallel mechanical configuration to amplify the force, as shown in Figure 18 below. The analytical formulation for the tip displacement

of these actuators is quite simple, and has been shown to closely agree with FEA and experimental results.[25]

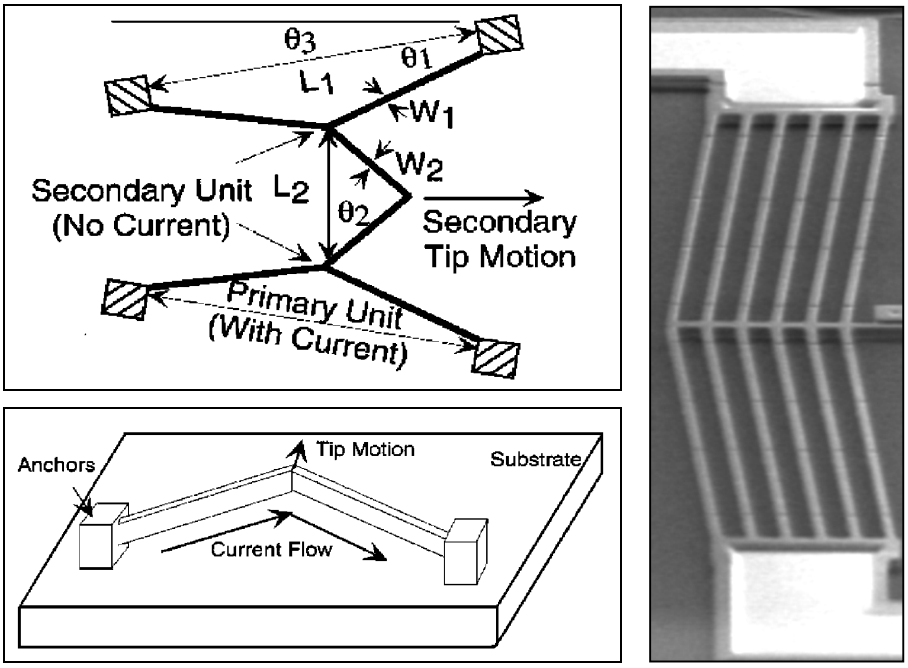

Figure 18: bent beam electrothermal actuators. Top left, a single bent beam unit. Bottom left, series cascading. Right, parallel cascaded structure.

The model facilitates the design of the actuators based on the following parameters: beam length, width, thickness and angle. The design tradeoffs are intuitive. A large angle between beams results in large forces, but smaller displacements. Thicker beam elements result in higher stiffness and force, but the lower resistance results in increased current consumption. Some of the design tradeoffs are exemplified in the load line graph shown in Figure 19.

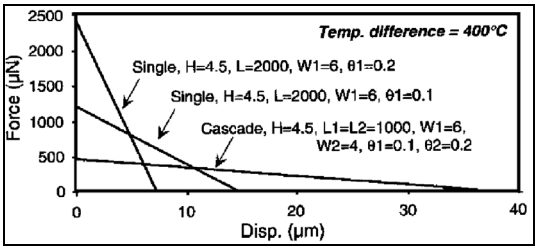

Figure 19: load lines for various bent beam geometries

Large displacements and low forces can be provided by the series or cascaded geometries, and higher forces come at the cost of lower displacements.

The advantages of this design are that large forces are attainable, the displacements are rectilinear, a parametric design method can be used, the operating voltage is low (<15 V) and a simple single-layer process can be used.

Some disadvantages include a large footprint, moderate sensitivity to ambient temperature and film stresses, high current consumption, and high operating temperatures (~700K)

2.1.1.4 Other Electrothermal Actuator Geometries

Several groups have implemented all out-of-plane, bi-material, and topology-optimized structures in MEMS. Typically, out-of-plane mechanisms using the electrothermal principle have higher displacement amplitudes than electrostatic parallel plate versions. One example of an out of plane actuator based on a geometry similar to the bi-directional lateral actuator is shown in Figure 20. [28] The inner beams are at a lower elevation than the outer beams, and by selectively heating beams on one layer (hot arms) and maintaining the other layer at a lower temperature (cold arms) a deflection in the direction of the cold arm is generated. This geometry produces deflections of approximately 10 um.

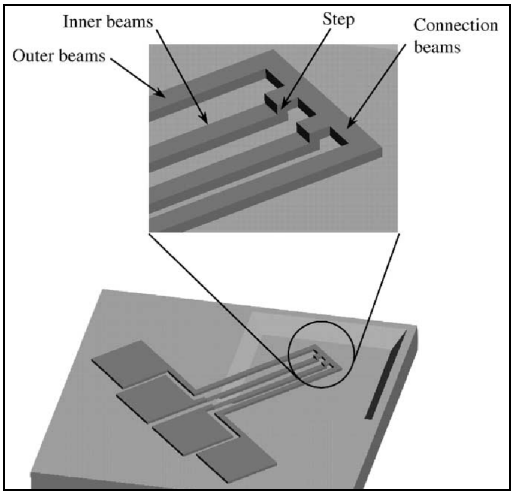

Figure 20: solid model of a single material out-of-plane actuator

Bi-material actuators were the original actuators based on the differential expansion of materials with different CTE's (coefficient of thermal expansion). Many examples of these structures exist in the macroscopic world, such as bimetal temperature gauges. Certain geometries that make of 2-material

bimorphs in cascaded geometries for large deflections and self-assembly are the focus of the actuator design section of this thesis, and will be discussed in greater detail.

Finally, the study of topology optimization applied to compliant mechanisms has generated interesting optimized structures that are capable of generating a desired output motion based on known inputs. First, a feasible topology is synthesized to meet the prescribed input-output force-displacement relationship. Once a feasible topology is established, performance constraints govern the optimization of the size and shape of the geometry. Constraints may involve minimizing energy loss, obtaining a desired motion amplification (geometric advantage) or force amplification (mechanical advantage), or ensuring that buckling doesn't occur under applied forces. [50] Two implementations of optimized structures with 20x geometric advantage used in a MEMS application are shown below in Figure 21.

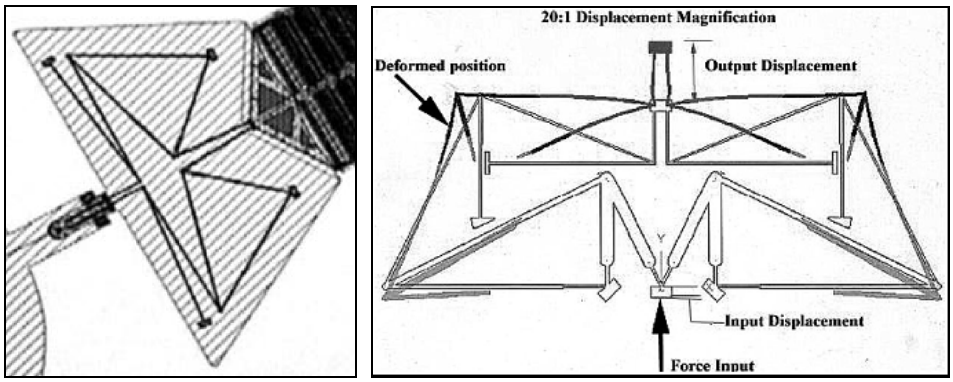

Figure 21: topology optimized geometric advantage designs

More recently, code has been written that accepts input currents or voltages and generates output forces and displacements based on electrothermal actuation. [51] In the case of electrothermal topology optimization, the actuator topologies are optimized by sequential steps of finite element analysis and material redistribution. Some resultant geometries of electrothermal topology-optimized structures are shown below in Figure 22. The measured forces and displacements are commensurate with the existing actuator designs discussed above, and the entire process follows a rational design methodology.

Design parameters				
Actuator number	1	2	3	4
Optimised for load k_1	550 N/m	550 N/m	1370 N/m	1370 N/m
Dimensions Width × Length × Thickness	500 μm × 200 μm × 11 μm	500 μm × 150 μm × 11 μm	500 μm × 200 μm × 16.4 μm	500 μm × 200 μm × 16.4 μm
Material distribution Black indicates material and white indicates void.				
Description	Electrodes at upper and lower left side of the design domain. Work point at the extreme right of the design domain.	Electrodes at upper and lower left side. Work point at the extreme right of the design domain.	Electrodes at each side of the design domain. Work point at central top of the design domain.	Electrodes at each side of the design domain. Work point at central top of the design domain.

Figure 22: electrothermal structures optimized for different loads with electrical inputs and mechanical outputs

A thorough discussion of this powerful method and its strengths is beyond the scope of this research; however, one should be aware that the optimizer should be used as a tool that cannot replace the intuition and creativity that a designer may apply. In fact, although topology optimized structures typically have non-trivial geometries, in some cases the solutions converge to familiar shapes, such as actuators 3 and 4 in Figure 22, which resemble bent beam actuators.

Many of the simple geometries of user-designed electrothermal actuators are amenable to analytical solutions and can be parametrically designed in some cases, whereas optimized structures must be re-calculated for any given set of inputs and desired outputs. The algorithms that are used are usually 2 dimensional, and can solve explicitly formulated problems such as those based on joule heating and thermal expansion. Problems based on electric field geometries and non-linear physical forces are substantially more complex.

The 3-D self-assembly and actuation structures that are the focus of this research have not been optimized using these algorithms. Problems with true 3-d geometries based on a weighted combination of non-linear forces that are applied selectively to regions of the design have not yet been solved in MEMS topology optimization literature, to the best of the author's knowledge. A 3-D optimizer that has the capability to segment the design space into active and passive areas with respect to the physical forces being used (i.e. joule heating of a 2-material bimorph) would be capable of generating optimized versions of the actuators presented here.

2.1.2 Electrostatic

2.1.2.1 Comb Drives

Comb drives are an extensively used method of actuation in MEMS; they have been thoroughly investigated for many years, and applied in numerous devices from micro mechanical resonant filters to inertial sensors to micro motors to hinged optical scanning devices. The basic geometry, shown in Figure 23, consists of a set of interdigitated beams or fingers connected to a stationary electrode and flexured shuttle. In order to ensure that the combs are symmetrically spaced during the operation of the device, the support springs must be stiff in the transverse direction and the out-of-plane directions, but soft in the direction of actuation. The crab spring shown below is one design that accomplishes this characteristic.

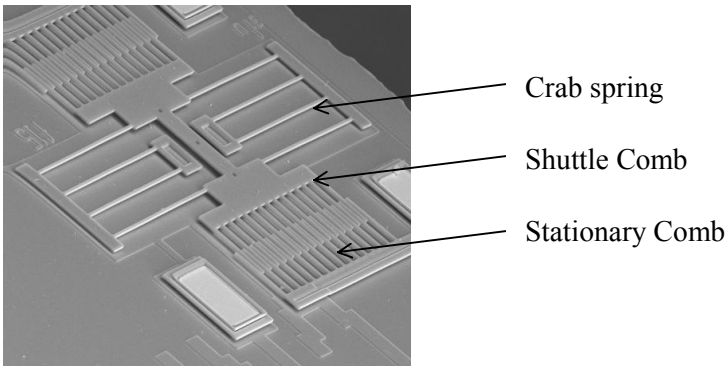

Figure 23: electrostatic comb drive actuator

Many alterations have been performed on this geometry in order to increase the travel range of the shuttle,[52] change the force characteristics,[53] attain rotational actuation or levitation,[54] or operate in a repulsive mode.[55] The analytical formulation for the simplest geometry consisting of interdigitated rectangular fingers is presented here, and it is shown that these fingers exhibit a constant force over a wide range of displacements. Consider the geometry of Figure 24 below.[53]

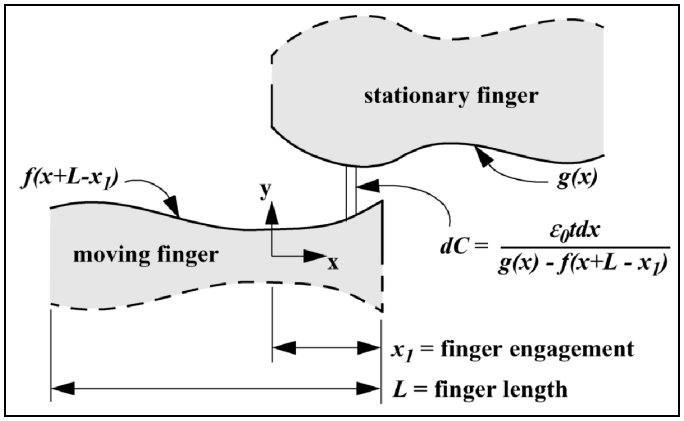

Figure 24: arbitrary comb geometry showing capacitance as a function of finger engagement

The force between the fingers is represented as

$$F_x = \frac{\partial E}{\partial x_1} = \frac{1}{2} V^2 \frac{dC}{dx_1}$$

where F_x is the electrostatic force, E is the stored energy between the conductor plates, V is the applied voltage, C is the capacitance between fingers, and x_1 is the relative engagement between the moving and fixed fingers. Calculating the capacitance as a function of engagement, we obtain

$$C(x_1) = 2\varepsilon_0 t \int_0^{x_1} \frac{dx}{g(x) - f(x + L - x_1)}$$

where t is the out-of-plane thickness of the fingers and ε_0 is the permittivity of free space. Furthermore, if the fingers are parallel and rectangular, the expression for capacitance simplifies to

$$C = 2\varepsilon_0 t \int_0^{x_1} \frac{dx}{h(x)}$$

where $h(x)$ is the gap profile between fingers. Since $f(x) = k$ for the rectangular case, $h(x) = g(x) - k$, and the force expression reduces to

$$F_x = \frac{V^2 \varepsilon_0 t}{h(x_1)}$$

Several factors can contribute to changing the resultant forces associated with this equation. First of all, if the gap between adjacent fingers is decreased, the force increases. Since the minimum feature size of a given process affects the minimum spacing that can be achieved, several geometries make use of clever geometries that reduce the spacing after the fingers are engaged, while still obeying the

process design rules. The geometry of the fingers can be altered in order to follow a certain force vs. deflection profile, as shown in Figure 25.[53] Also, thicker processes linearly increase the electrostatic force and reduce the contributions of non-linear fringing fields to this first order approximation; however the beam stiffness of the support structure increases linearly as well.

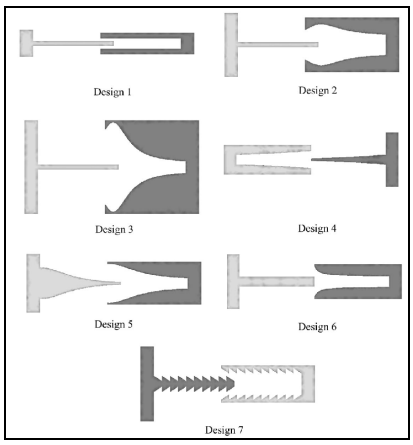

Figure 25: various comb geometries designed for various force vs. deflection profiles

Some of the advantages of comb drive actuators are low power consumption, large resonant displacements, modular design, and insensitivity to thermal variations. The lifetime characterization of these devices has shown a very high measure of reliability both in air and in vacuum, with no apparent degradation in performance or indication of wear over billions of cycles of resonant operation. However, the operating voltages are high (~ 50 - 150 V), even with the use of smaller gaps and optimized geometries. The static displacements are much smaller than resonant displacements, and the forces associated with this type of actuation are much lower than those generated by thermal expansion. Furthermore, the footprint of an array of comb drives is typically quite large, and the motion is limited to in-plane displacements in most cases.

2.1.2.2 Parallel plate actuators

Membrane and parallel plate type actuators have been used in microphones, variable capacitors, microfluidic pumps, RF switches and reflective grating applications for over a decade. In fact, Petersen presented the first micromachined electrostatic cantilever actuators and membrane switches in 1978.[56] In the case of a parallel plate configuration, the force can be determined starting with the energy stored (W) and ignoring the fringing fields,

$$W = -\frac{1}{2}CV^2 = -\frac{1}{2}\frac{\varepsilon_r \varepsilon_0 A V^2}{x}$$

thus the force between the plates is

$$F = \frac{dW}{dx} = +\frac{1}{2}\frac{\varepsilon_r \varepsilon_0 A V^2}{x^2}$$

The non-linear nature of this force curve is the cause of instability once the voltage exceeds a threshold. For instance, with a cantilever structure, once the deflection exceeds a certain voltage the position of the tip is unstable and the beam spontaneously deflects all the way down. This threshold voltage is derived in Kovacs (p.279) [2], and is determined by the following expression:

$$V_{th} \approx \sqrt{\frac{18EId^3}{5\varepsilon_0 L^4 w}}$$

where

d = gap between cantilever and electrode

L = length of the beam

w = width of the beam

E = Young's modulus

I = Moment of inertia

In order to obtain the deflection characteristics of parallel plate devices, one simply substitutes the electrostatic force into the mechanical expression for beam deflection. For a plate supported by flexures, the force over the plate is distributed equally to the flexures.

This instability has been resolved by using charge control methods in the drive circuit instead of voltage control, and the results do increase the stable range of the actuator [57]; however, the control circuit is not trivial.

The advantages of this design are low power consumption, simple design, and insensitivity to thermal variations. Disadvantages include the instability discussed above, high operating voltages, small displacements and low forces. Also, these devices should be designed carefully with respect to stiction, since large surface areas may come into contact during release and operation.

2.1.2.3 Scratch Drive Actuators

The scratch drive actuator is an electrostatic actuator based on asymmetries in friction. A diagram of the SDA is shown below in Figure 26.[58] The cross section of the SDA shows a flat plate and a bushing.

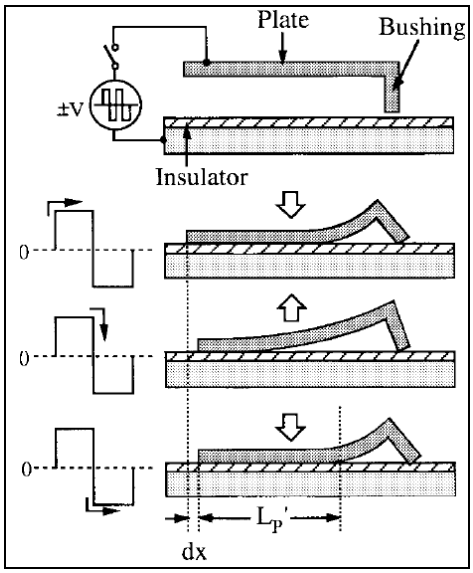

Figure 26: Scratch drive actuation principle

A high oscillating voltage (~75V) is applied between the device and the substrate. The attractive forces associated with the actuation voltages are quantified by the following expression:

$$F_{el} = \frac{\varepsilon V^2 A}{2h^2}$$

where V is the applied voltage, A is the area of the plate, and h is the gap between the plate and the substrate. An insulating layer such as a nitride is used to prevent shorting. As the plate buckles due to electrostatic attraction, the bushing scrapes forward. When the voltage is removed, the plate's restoring force causes the actuator to snap back to its initial position. Asymmetries in the friction in the forward direction compared to the reverse direction cause a net displacement on the order of 30 nm. A detailed analytic model of the electrostatic forces and an optimized geometry for this type of actuator has been published.[30] Although the friction forces exerted by the SDA during the actuated portion of the voltage cycle are high enough to overcome stiction, the device often remains stuck in position at the end of its range when the power is removed. SDA's are notorious for their stiction failure, but the forces they can provide are higher than many other forms of actuation.

2.1.3 Impact Drive Mechanisms

Piezoelectric, thermal expansion and electrostatic methods of implementing impact drive mechanisms have all been attempted and published.[40,41,42] The principle of operation of these mechanisms is similar to "slip-stick" mechanisms often employed in piezoelectric motion control systems. If inertial forces overpower static friction forces acting on a mass momentarily, the mass undergoes a short period of acceleration in a desired direction. By controlling the forces in an asymmetric fashion, overall motion in a desired direction can be achieved. Figure 27 below illustrates the sequence of steps that are followed in the operation of an impact drive mechanism.

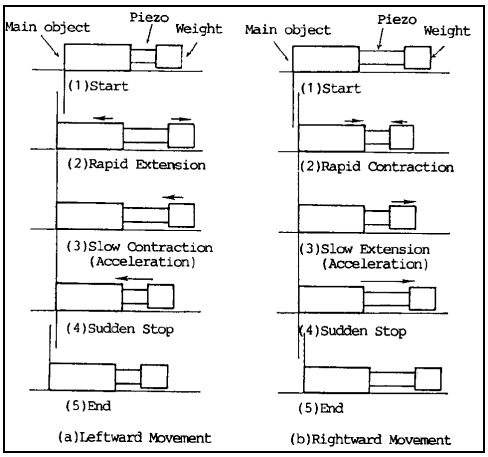

Figure 27: Impact drive mechanism cycle of operation

As illustrated above, the rapid motion of a mass attached to the main object overcomes static friction forces and results in an acceleration of the main body in the opposite direction. During the following slow motion step, the mass returns to its original position (with respect to the main body) but the main body remains stationary in its new position. These steps can be repeated indefinitely to increase the displacement of the mechanism. The advantages of this method include small step sizes over a large range, for precise positioning applications over large distances. Also, some implementations use optical or RF means to heat parts of the structure such that wires are not required. Electrostatic versions have been demonstrated to operate reliably for over 550 million cycles. Disadvantages include large power requirements, large footprint, vulnerability to inertial forces, and variations in the step size repeatability and reliability with atmospheric changes (pressure, humidity).

2.1.4 Magnetic Actuation

Magnetic actuators are very common in the macro-domain (motors, solenoids, relays, etc.) and are becoming increasingly common in micromachined devices (optical modulators, micro relays, micro motors, etc.) Several methods of generating forces based on magnetic fields have been successfully attempted in MEMS, some of which scale better into the micro-domain than others. Electromagnetic forces scale as the area squared, assuming constant current density in the actuator windings, and so they shrink rapidly as systems become smaller. Increasing the current density results in higher power dissipation, so many applications make use of Permalloy materials deposited as thin films that are actuated by an external magnetic field.

Nickel-Iron films are often electroplated or otherwise deposited to make a mechanism magnetically anisotropic. [59] Polymer magnets consisting of magnetically hard materials have been deposited onto microstructures as well. [60] In one magnetic microactuator, magnetic thin films are electroplated onto polysilicon flexure structures to obtain large in-plane and out-of-plane actuation, as shown in Figure 28 below. [61] Self-assembly has been performed using external magnetic fields, and will be discussed in the following section. Magnetostrictive materials experience strains when an external magnetic field is applied. The strains that are produced by this phenomenon can be used to deflect a bimorph. [62]

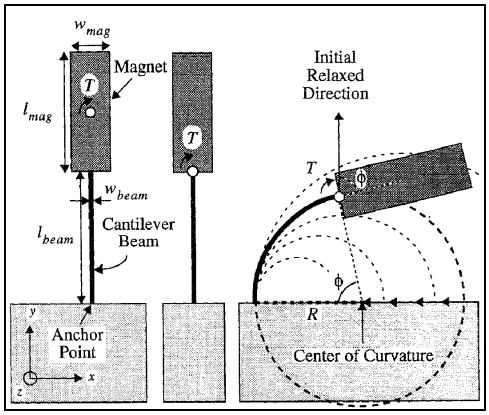

Figure 28: magnetic actuation of polysilicon flexure structures

2.1.5 Piezoelectric Actuation

Piezoelectricity is a phenomenon in which a mechanical stress on a material produces an electrical polarization, and reciprocally an applied electric field produces a mechanical strain.[2][p.215] The applied voltage V across the material gives rise to a corresponding force F that in turn produces a

dimensional change L. Typical values for L vary between 10E-10 and 10E-7 cm/V, and so large voltages (often exceeding 1000V) are required in order to obtain micron scale displacements.
In one example of a MEMS piezoelectric actuator, electrodes are patterned on both sides of a thin film of PZT (lead zirconate titanate) in order to obtain a bimorph structure.[63] Two bimorphs are used in order to implement a scanning micromirror structure as depicted below in Figure 29.

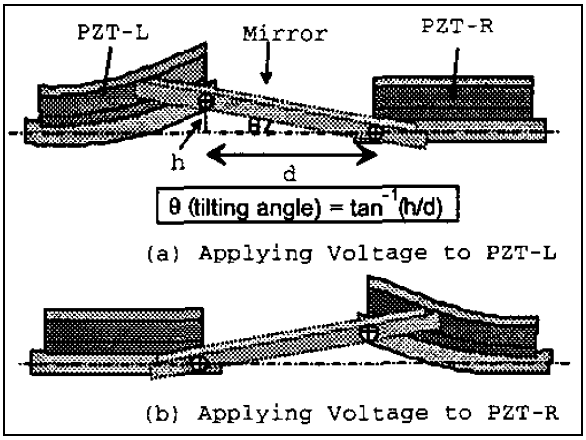

Figure 29: PZT actuated tilting micromirror structure

2.2 Power-off positioning and self-assembly techniques

The structures obtained by surface micromachining are often called 2 ½ dimensional, since 2-D masks define the geometric features patterned by lithography. Using a large number of thin film layers to define lateral geometry layer-by-layer is impractical due to the prohibitively large number of masks and lithography steps that would be required for such a process, although some maskless rapid prototype systems make use of such a method.

Creating 3-D MEMS structures is desirable or required for a large number of applications, and has been shown to dramatically improve the performance of some devices. Some examples of the utility of ascending MEMS into the third dimension are briefly discussed below.

High frequency inductors that are fabricated in CMOS processes suffer from losses due to the underlying silicon substrate. Bulk micromachining has been used to remove part of the substrate under the windings to reduce these losses. Ideally, if the magnetic field lines were parallel to the substrate instead of perpendicular to it, substrate losses could be eliminated. Assembling the inductor out of the plane of the substrate accomplishes this.

A corner-cube reflector is a device that consists of three orthogonally positioned reflectors. This geometry always reflects an incoming collimated beam back to its direction of origin, and is advantageous in free-space optical communication links. Microassembly allows the planar surface micromachined mirrors to be assembled into the corner cube reflector geometry.

Actuated micromirrors have been used in displays, imaging systems and optical switches. It is often desirable to increase the actuation angle of these flat plates; however, even a small angle of actuation about the centroid in the as-fabricated position would result in contact between the mirror edge and the substrate. Assembling the structure away from the substrate has been used to remedy this problem.

In some cases, permanently modifying the geometry of a device can serve the purpose of tuning its response to an input. In RF systems, such tuning elements are required to ensure desired circuit characteristics. In optical systems, micro-alignment of sources to fibers is critical to minimize losses. Assembly methods can be used to achieve such tuning capabilities, with the advantage of consuming no power once the tuned value is fixed. Latching mechanisms, bistable mechanisms, and deformation methods can be used for these purposes as well as assembly.

Finally, the question of integration vs. assembly of microsystems is a commonly debated topic in MEMS. Integration is difficult when disparate technologies have conflicting process

requirements. For instance, the high thermal budget of some LPCVD techniques for the deposition of thin films is incompatible with most CMOS processes. MEMS micromirror optical switches consisting of collimated fiber inputs and outputs need to be assembled with critical alignment tolerances. Although considerable effort has been spent on integrating disparate technologies (a remarkable example is the Texas Instruments digital micromirror device), many assembly solutions have been proven effective.

2.2.1 Flip Chip Bonding

Flip chip bonding allows a high density of interconnects to be made between two substrates. In MEMS, the technique usually involves the placement of micro indium or gold balls on the points of contact, aligning the chips, applying thermosonic and/or pressure forces, and removing the MEMS substrate by performing a chemical etch (release step). This particular method was pioneered and developed by Bright et al. using an in house custom-built bonder, and Figure 30 below demonstrates the process concisely.[64]

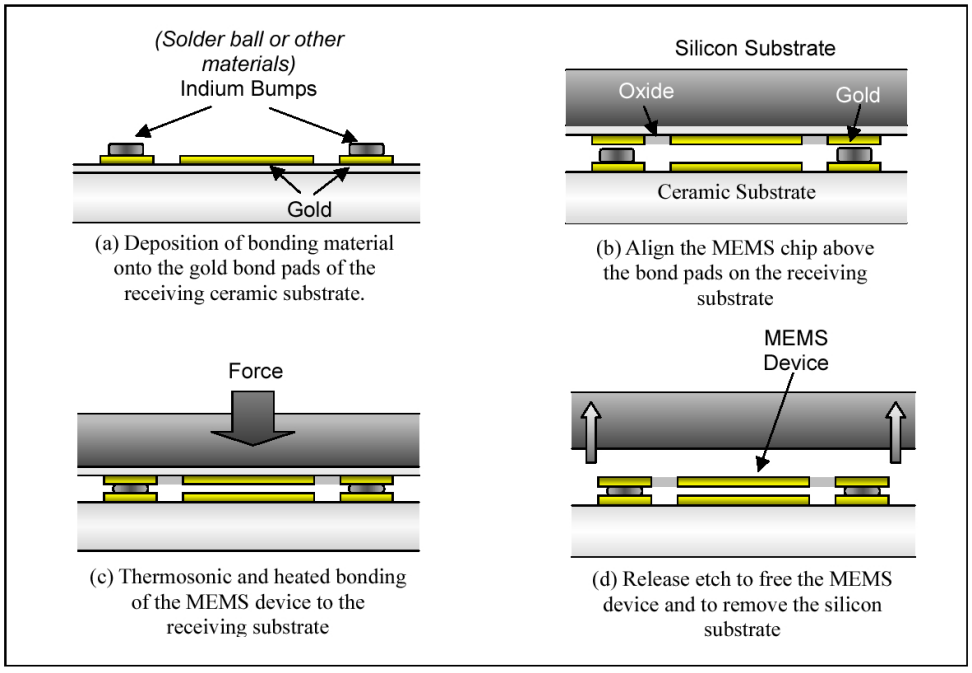

Figure 30: flip chip bonding of fully released MEMS device onto a ceramic substrate

Aside from the obvious benefits of integrating MEMS with electronics or other technologies, removing the surface micromachined structure from its substrate can reduce losses in RF systems.

2.2.2 Bistable mechanisms

A linear spring structure, such as a singly clamped beam with small deflections, stores potential energy as it is deflected. The lowest energy state of such a system occurs when the system is in equilibrium with zero deflection. In bistable mechanisms there are two distinct stable states of equilibrium. Most mechanisms of interest to MEMS applications rely on the storage of strain energy. The focus here is on purely flexural structures with no hinges or sliding contacts.

A simple and intuitive diagram explaining the nature of a mechanical bistable mechanism is shown below in Figure 31. [65,66,67]

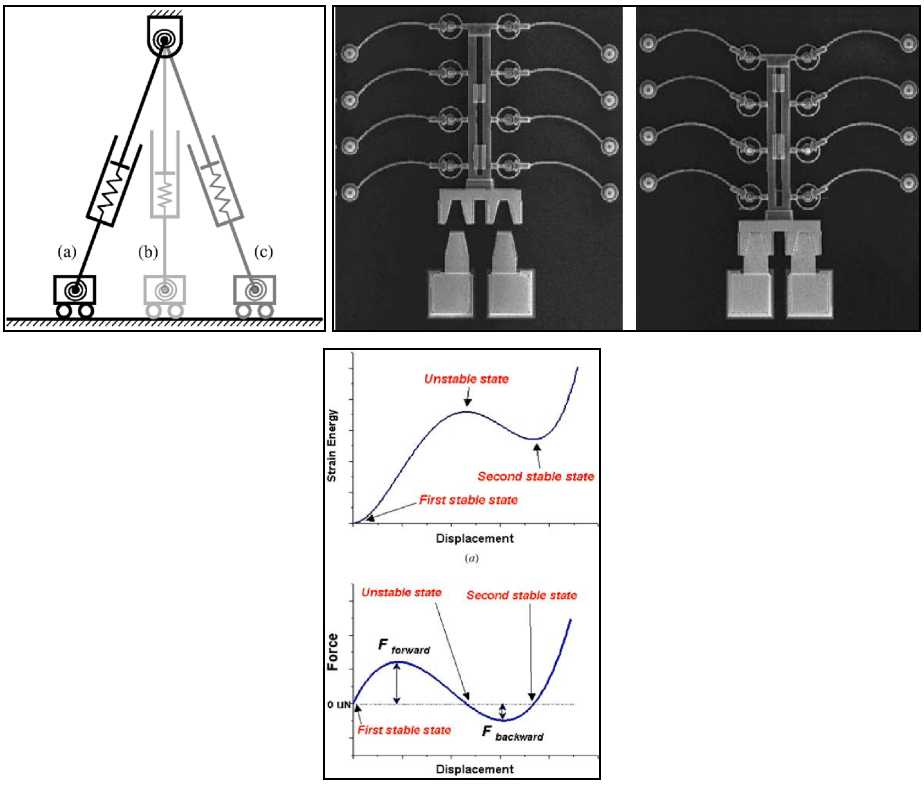

Figure 31: principle of operation of bistable mechanism (left), bistable relay in off and on positions (center), and stored energy and force curves for a typical bistable system (right).

The design shown in figure 31 contains hinges, but several implementations of bistable structures that are purely flexural are contained in the references. A beam that buckles under an axial load will store

strain energy when subjected to a lateral force. When the strain energy stored is at a maximum, "snap through" occurs and the beam assumes a mirrored position.

There are numerous applications that make use of these structures. Quiescent power consumption in micro relays can be eliminated since the on and off states can correspond to the equilibrium states of a bistable system – power need only be applied briefly in order to switch between these states. However, tuning functions that require continuous control of the position of a structure cannot be implemented since the stable positions are distinct.

2.2.3 Latching with Contact Forces

Several designs have made use of direct mechanical interference to fix the position of an actuated structure. These designs can provide multiple stable positions and are simple to design and operate. An example of an in-plane latching mechanism designed by the author is shown in Figure 32: latching mechanism that fixes in-plane position with an out-of-plane actuator. In this design, a lateral actuator (X direction) and an out-of-plane actuator (Z direction) are present. When the Z actuator is on, the X actuator is free to move. When a desired X actuation is achieved, the Z actuator is turned off and the latch interference prevents the X actuator from returning to its initial position.

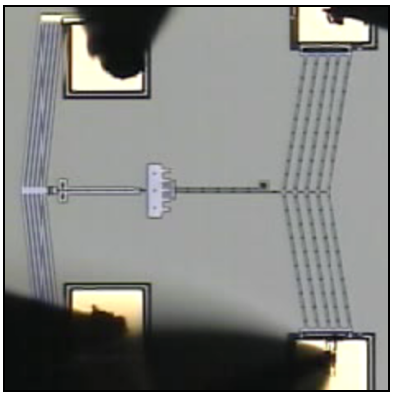

Figure 32: latching mechanism that fixes in-plane position with an out-of-plane actuator

Ellis[68] has designed more robust versions of interference-based latches. These thicker structures (50-100 um) make use of a latch structure, but all the actuators are in-plane in these designs, since large out-of-plane deflections are difficult to achieve with thick devices. Finally, Geisberger[69] has designed the conformal latching mechanism shown in figure 33 below. In this design, the conformal nature of thin films deposited in LPCVD processes is used to create the interference in the latching mechanism. Holes placed in the poly1 layer are conformally filled by material from the poly2 layer, and the resulting dimple-like structures prevent in-plane motion. When the poly2 beam is buckled out of plane, the poly1 layer is no longer constrained. In this design, the conformal nature of thin films deposited in LPCVD processes is used to create the interference in the latching mechanism. Holes placed in the poly1 layer are conformally filled by material from the poly2 layer, preventing in-plane motion. When the poly2 beam is buckled out of plane, the poly1 layer is no longer constrained. This design is compact, effective, and consists of a simple modular geometry that requires a single drive signal. Although the contact forces result in occasional stiction, the force of the buckling actuator can overcome these forces and the poly2 stop prevents the poly1 layer from moving out of plane.

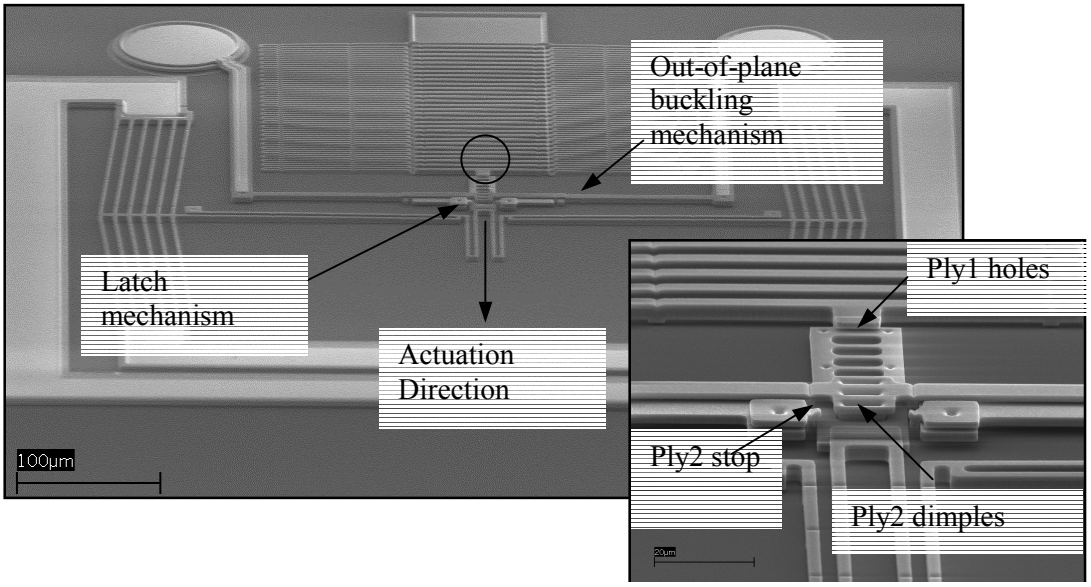

Figure 33: latching mechanism based on conformal deposition of thin films

2.2.4 Hinged, Fluidic, Magnetic, and Directed Assembly methods

As is evidenced by the plethora of assembly methods that have been attempted in MEMS, manufacturing 3-Dimensional microstructures and integrating disparate technologies are powerful capabilities. In this section, several methods of micro-assembly that have been developed over the past decade are discussed.

Hinge-based assembly methods were among the first attempts at addressing the need to create 3-D structures in MEMS.[70] The structure of the hinge consists of a fixed staple and a movable pin, as shown below in Figure 34. This basic mechanism has been extended and many alterations of the geometry have added functionality. Polarity hinges allow for only one direction of deflection. Multiple plates have been constrained by hinges in order to reduce the assembly process to a single degree-of-freedom of motion.[71] This single step process is illustrated in Figure 34 below as well.

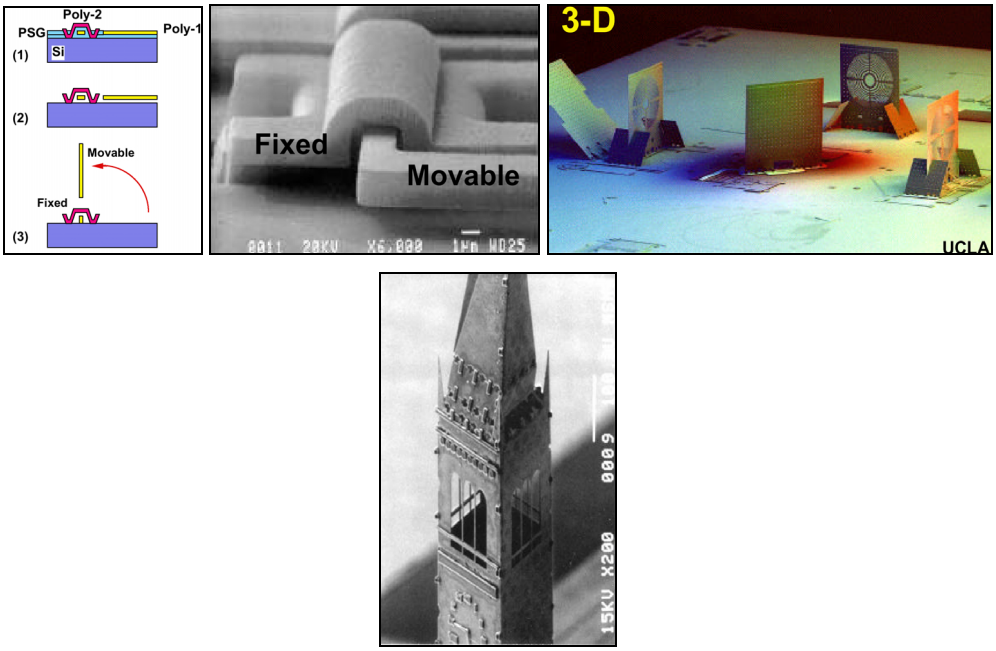

Figure 34: illustration of hinge design and operation (left), SEM of microfabricated hinge (top center), assembled micromirrors and fresnel lenses in free space micro optical bench application (top right), and single step assembly of a complex microstructure (bottom).

Although the initial hinge-based assembly operations were performed manually with probes, automated versions exist as well. Scratch drive actuators can exert enough force to erect hinged structures out-of-plane, and they were initially applied to assemble free space optical benches.[72] The Micro Elevator by Self Assembly (MESA) technique involves the use of SDA's to elevate devices such as inductors away from the substrate, and is discussed further in the inductor section below (2.3.2). Electrostatic and electrothermal methods of actuating hinged structures have been investigated as well for scanning micromirror applications.[73] Centrifugal forces have been used to accomplish the same goal, without the need for powered actuation on the substrate.[74] Thermokinetic forces in conjunction with ultrasonic vibrations have been used to assemble structures such as those in Figure 35.[75] In this research, the purpose of the substrate vibrations is to remove the static friction, and the thermokinetic forces (resulting from gases released from the heated substrate under vacuum conditions) perform the assembly. Another method of hinged assembly is based on the deposition and patterning of Permalloy materials that are subsequently actuated with an external magnetic field. The authors report a high yield and high efficiency, as demonstrated in Figure 35.

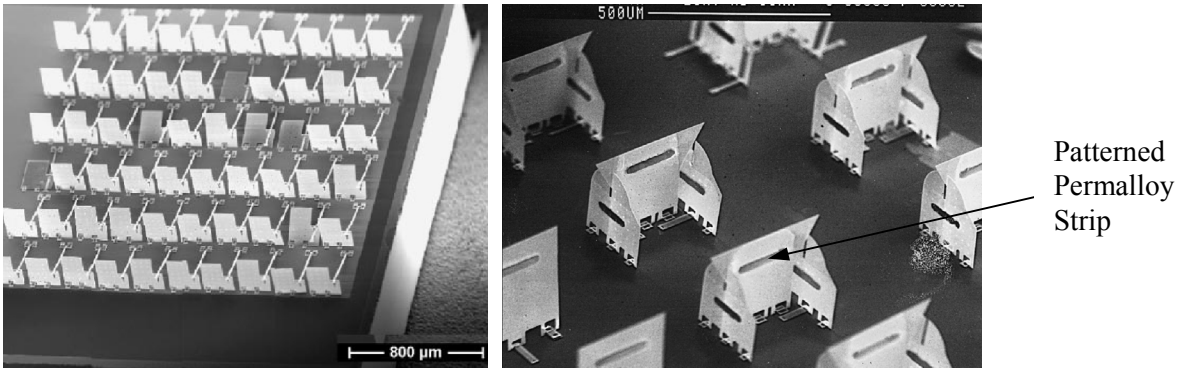

Figure 35: batch assembly of structures using thermokinetic and ultrasonic forces (left) and an external magnetic field (right).

Solder balls have been used to assemble hinged plates by Green et al [76]using the surface tension forces from the reflowed solder. This technique was later perfected by Bright et. al. and demonstrated in a micro-rotary fan application shown in Figure 36 below.[77]

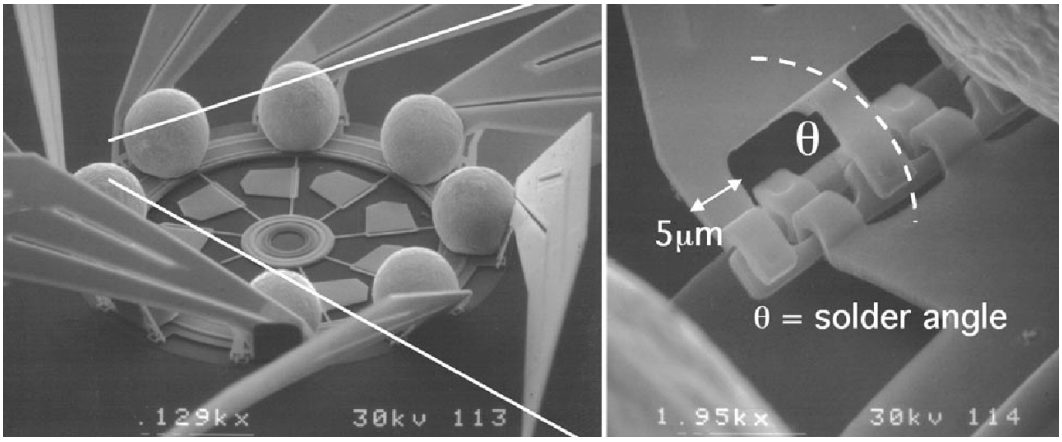

Figure 36: solder self-assembly

This surface tension powered process is another example of self-assembly as opposed to the directed assembly that was required to obtain the structures in Figure 34.

Surface tension forces have also been used to power self organization processes, as reported by Syms et. al.[77] Alignment based on shape recognition can be performed using surface tension forces. The parts are suspended in fluid and randomly attracted to the assembly site, which contains patterned regions with hydrophobic adhesive. When the hydrophobic pattern on a part comes into contact with an adhesive-coated substrate binding site, shape matching occurs spontaneously due to

interfacial free energy minimization. The parts assume the minimum energy configuration, which corresponds to the perimeters of the site and the part being aligned – the parts can be aligned to an accuracy of 0.3 degrees, with 100% yield.[78] Figure 37 below shows a micromirror assembled onto a released actuator using this powerful technique.

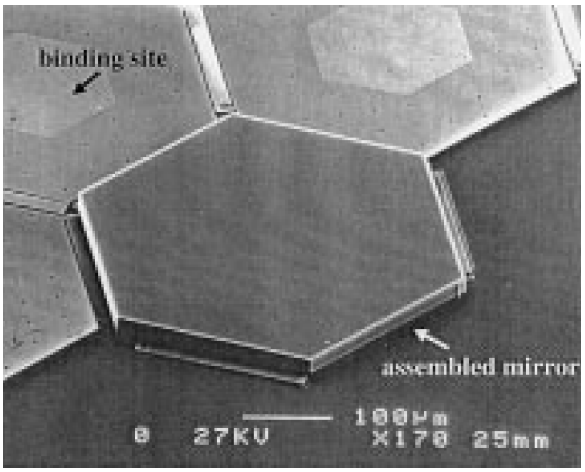

Figure 37: surface tension powered self assembly

Plastic deformation magnetic assembly (PDMA) of microcomponents has been developed for various applications at Urbana-Champaign. The beams shown in Figure 38 are assembled using this method, in which an external magnetic field is applied to re-orient the Permalloy material. A gold region at the base of the beams undergoes plastic deformation under the high stresses that result from the beams bending upward. Once the magnetic field is removed, the beams remain in this out-of-plane position.[79]

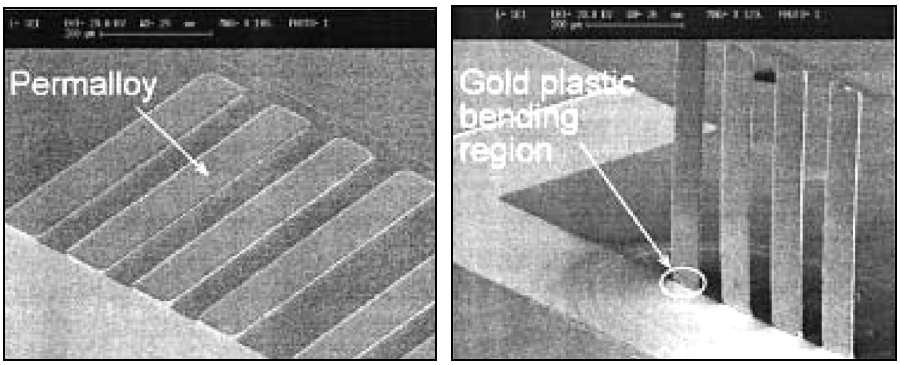

Figure 38: PDMA beams before (left) and after (right) application of external magnetic field.

2.3 RF MEMS Discrete Components

Many groups have focused considerable effort on variable capacitors, with large tuning ranges and high quality factors (Q) as their design objectives. Considerably less effort has been placed on variable inductors, which typically suffer from low Q and self-resonant frequencies due to process limitations such as lossy substrates and thin conductors. Some publications offer a review of RF MEMS from either a device perspective or a circuit perspective.[80,81] RF MEMS switches, phase shifters, mechanical resonators and filters have been developed extensively as well, but they are not the focus of this work. A discussion of RF capacitors and inductors follows.

2.3.1 Capacitors

RF MEMS capacitors can be broadly categorized based on three different tuning mechanisms: area tuning, dielectric tuning, and gap tuning. The well-known equation for parallel plate capacitors, neglecting fringing fields, is

$$C = \frac{\varepsilon_0 A}{d}$$

ε_0 is the permittivity of free space, A is the area of overlap between plates, and d is the distance between plates. A micromechanical electrostatic actuator has the geometry that corresponds to the gap tuning structure, which is non-linear in nature. Area tuning could be accomplished, for example, by translating one of the plates laterally – this would result in a more linear tuning curve, but would have a lower tuning range. Finally, one could adjust the effective dielectric constant by varying the volume of a dielectric that is inserted between the plates.

The Q, base capacitance, and tuning range are the metrics typically used to characterize a capacitor. One expression for the Q, assuming that other loss factors are negligible compared to the resistive losses, is

$$Q = \frac{1}{\omega C R}$$

Thus, the larger the series resistance, the smaller the Q. Another parameter in the set of figures of merit is the inductance associated with a tunable capacitor, which contributes to the electrical self-resonant behaviour of these devices. For frequencies beyond the self-resonance caused by this LC circuit, the inductance dominates. A low parasitic inductance ensures a high self-resonant frequency. The last and perhaps most challenging parameter for a tunable capacitor is its linearity in response to RF power. A third order intermodulation product, or IP3, of greater than +50 dBm is often required.

Solid-state components such as varactors have room for improvements in all these categories. Tuning ratios are often 30% or less, resistive and substrate losses contribute to lower Q's (typically in the low 10s), and self-resonances can occur at lower frequencies due to large parasitic effects.

2.3.1.1 Parallel Plate and Membrane Capacitors

The first variable capacitor in MEMS was a membrane type capacitor fabricated in 1978 by Petersen.[56] These capacitors have been used extensively in switching and phase shifter applications.[82] Tuning ranges of 100:1 have been demonstrated in discrete capacitors that are used for switching applications, and a 22:1 tuning range has been achieved in capacitors that can be linearly tuned.[83] Parallel plate capacitors have also been shown to exhibit high Q-factors, especially in flip chip designs where a Q of 1050 was measured at 1 GHz, and Q=100 was measured at 10 GHz. The Q's obtained for this capacitor were calculated after de-embedding losses; however, initial measurements on the device yielded Q's of over 300 at 1 GHz.[84] A table of typical values for tunable capacitors is shown below (Table 1).[80]

Table 1: Comparison of Several MEMS capacitors

Device characteristics and performance parameters	Varactor diodes	University of California at Berkeley [55–57]	Columbia University [58]
MEMS technology	—	Surface	Surface
Device size (μm × μm)	Discrete SC-79	~800 × 800	~450 × 450
Structural material	Silicon	Aluminium	Polysilicon
Actuation mechanism	Hyperabrupt junction	Electrostatic	Electrostatic
Actuation voltage (V)	4	5.5	1.8
Minimum capacitance (pf)	2 at 4 V	2.11	3.5
Tuning range (%)	335	16	25
Tuning range limit (%)	—	50	100
Series resistance (Ω)	2.8	1.2 at 1 GHz	—
Quality factor, Q	350 at 50 MHz	62 at 1 GHz	9.6 at 1 GHz
Series inductance (nH)	1.5	Not available	Not available
Self-resonance (GHz)	~1.3	>1.2 GHz[d]	>5 GHz[d]
Linearity	Poor	Not available	Not available
Others	Data obtained at packaged level (surface mount)	Data obtained for four tunable caps in parallel	Data obtained at proble level with bond pads included

Device characteristics and performance parameters	University of Colorado [64]	HRL[a] [54]	Rockwell RSC [48, 60]
MEMS technology	Surface + Bonded	Surface	Bonded wafer
Device size (μm × μm)	~500 × 800	~150 × 500	~1000 × 2000
Structural material	Polysilicon	Au	Silicon
Actuation mechanism	Electro-thermal	Sliding motor	Electrostatic
Actuation voltage (V)	5	80–200[b]	2–14
Minimum capacitance (pf)	0.9	0.035	1.8
Tuning range (%)	~90	185	200
Tuning range limit (%)	—	—	—
Series resistance (Ω)	6.2[c]	Not available	1.8
Quality factor, Q	256 at 1 GHz[c]	—	34 for 5.19 pF at 500 MHz
Series inductance (nH)	0.262[c]	Not available	0.19
Self-resonance (GHz)	31[c]	—	5 for 5.19 pF
Linearity	Not available	Not available	IP3 > +50 dB m
Others	The electro-thermal actuator draws a current of about 10 mA	Cap change was measured using mechanical motion	Tuning is electrically isolated from RF. Requires no chokes.

[a] Possible work after 1991 [54] is not available.
[b] 80–200 V to initiate movement of the structure.
[c] Values extracted from S-parameters for $C = 0.102$ pf. Bond pads and parasitics are excluded.
[d] Representing the highest frequency measured.

Two versions of the gap tuning capacitors discussed above are shown in Figure 39. The membrane capacitor developed by Goldsmith et. al. and an electrothermally actuated flip chip design of Bright et. al. are shown.

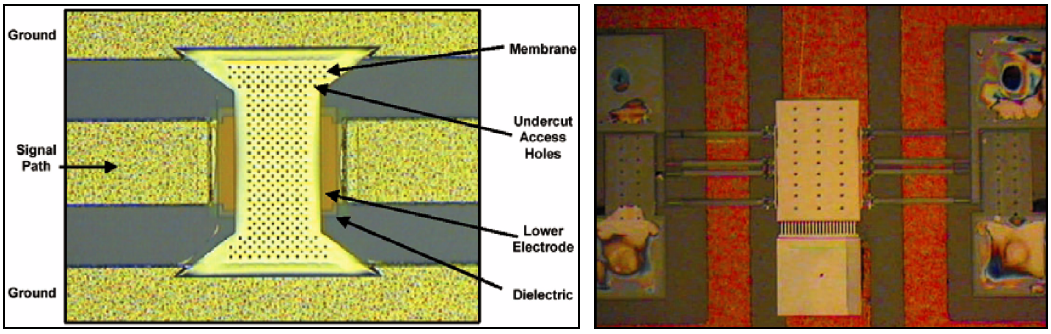

Figure 39: electrostatic membrane-type capacitor and electrothermal parallel plate capacitor

Several examples of high Q, large tuning range variable capacitors based on the area tuning effect have been fabricated and characterized as well. The comb-drive design shown below in Figure 40 was reported to have a Q value in excess of 100 with a tuning range of 8.4 – 1.[85] Some SEM pictures of the device are shown in Figure 40. The design consists of a set of comb drives for actuation and another set of geometrically similar combs that exhibit the tuned capacitance effect. The process makes use of thick silicon (~20-30um) that is later coated with a metal thin film.

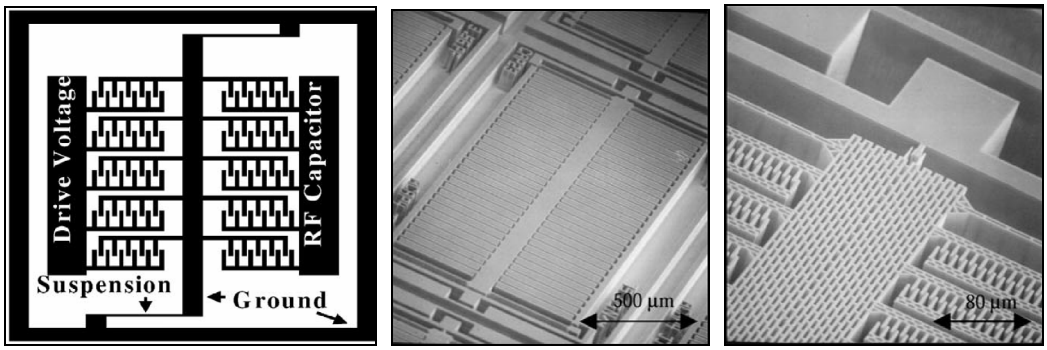

Figure 40: area tuning capacitor

Finally, the dielectric tuning type of variable capacitor is discussed. This type of design has been reported to yield a Q value of 291 at 1GHz, with a lower tuning range of 7.7%. Another version of this design has a Q of 218 with a tuning range of 40%.[86] The tuning mechanism involves the introduction of a movable dielectric slab between the two conductive plates of the capacitor, as shown in Figure 41.

One of the mechanisms uses lateral movement of the dielectric nitride, and is shown in the figure. Other mechanisms with increased tuning range vertically adjust the position of the dielectric layer. The dielectric consists of a nitride layer, and the conductors are 5 um thick copper.

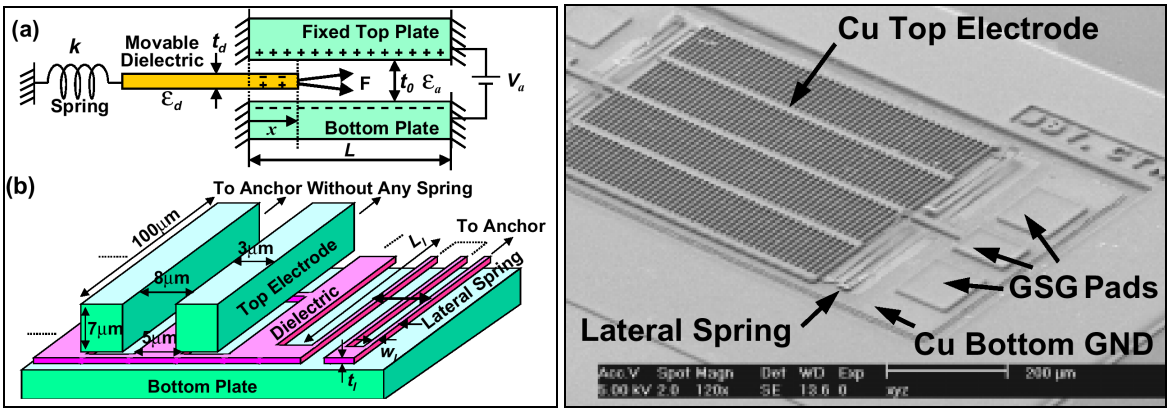

Figure 41: dielectric tuning capacitor

2.3.2 Inductors

The resistive nature of thin-film technology, dielectric loss in silicon substrates, and the close coupling between spiral turns are all significant barriers for integrated on-chip inductors. Several approaches have been taken to reduce these parasitic effects, and some examples of devices founded on these approaches are provided here.

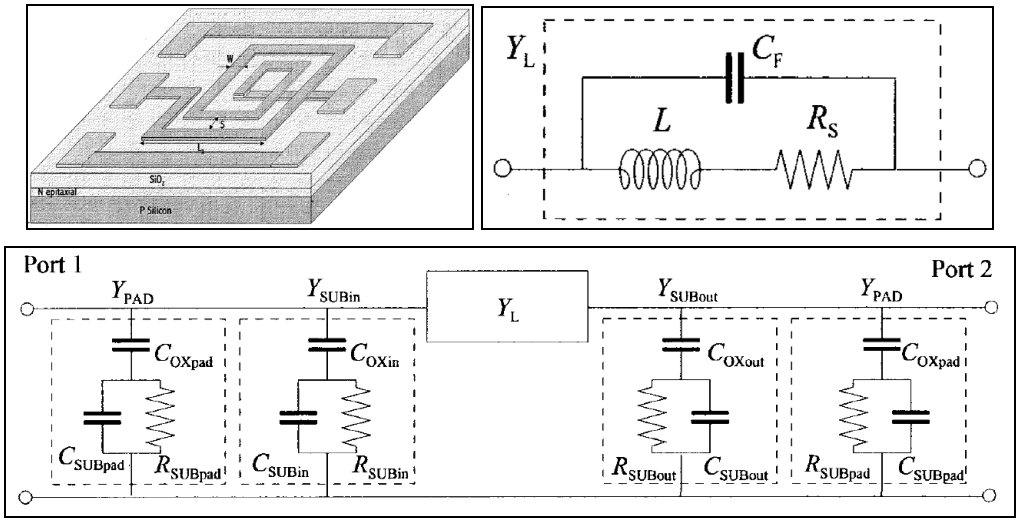

Figure 42: modeling parasitics in a MEMS inductor

A drawing of a typical spiral inductor with schematic depictions of the parasitic contributors is shown in Figure 42. [87]

The parasitics shown are the capacitive coupling of the pads to the oxide and underlying substrate, the capacitive coupling of the inductor to the oxide and the substrate, and the losses associated to the electrical coupling with the substrate. Several methods have been employed to reduce the effects of these parasitics, and some are discussed below.

One way to reduce substrate effects is to locally remove the substrate underneath the metallization layer, using an anisotropic etchant such as KOH. This method was implemented by Chang et al, [88] among others, to increase the self-resonant frequency from 800 MHz to 3GHz, and obtain a Q of 5.

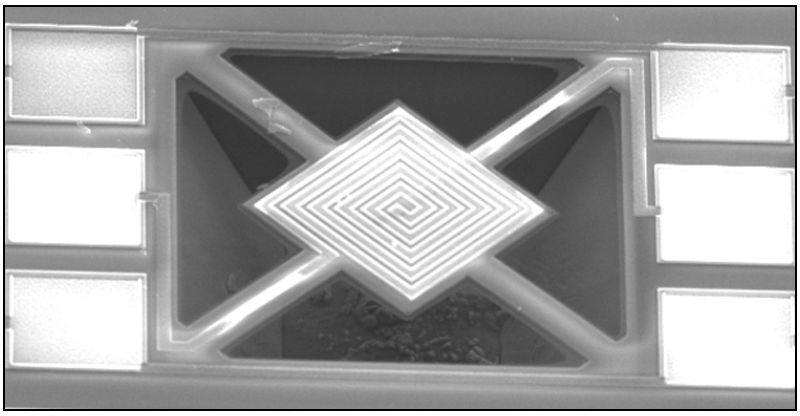

Figure 43: inductor suspended over an anisotropically etched (KOH) pit to reduce substrate losses.

Electroplating methods have also been employed to create micro inductors with thicker conductors, and obtain 3-D structures with magnetic fields geometries that do not enter the substrates. A tunable inductor structure fabricated at University of Texas, Dallas and assembled by Zyvex is shown in Figure 44. A ferrite core is inserted into the electroplated inductor in order to achieve a tuning effect. These inductors have exhibited Q's of 40 at 2.4 GHz and self resonances at 10 GHz.

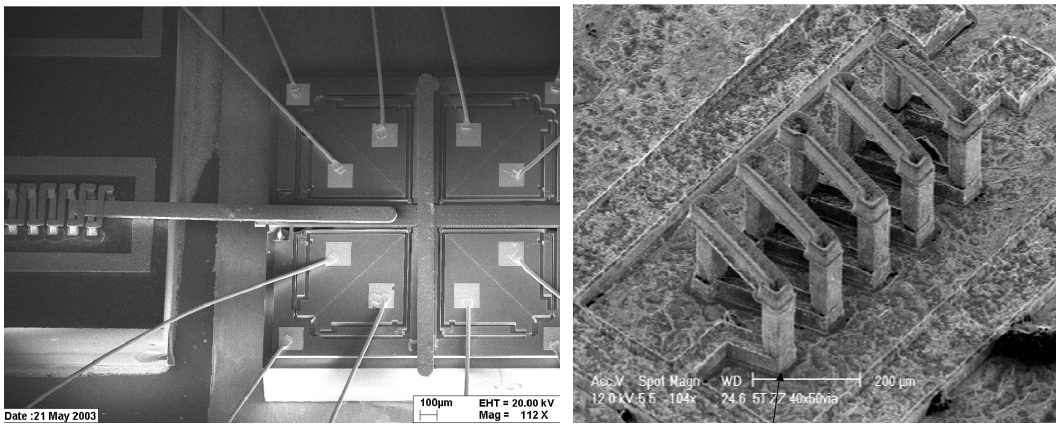

Figure 44: 3-D inductor fabricated using electroplating methods (left) and insertion of a ferrite core for tuning by MEMS actuation

A tunable inductor based on switching conductor loops in or out of the circuit is shown in Figure 45. The switch mechanism is a beam that is initially deflected due to stresses in the fabrication process. The beam is actuated electrothermally and then attracted to the substrate electrostatically in order to make an ohmic contact to add turns to the inductor. A Q of 3.3 at 4.6 GHz was obtained with this device.[89]

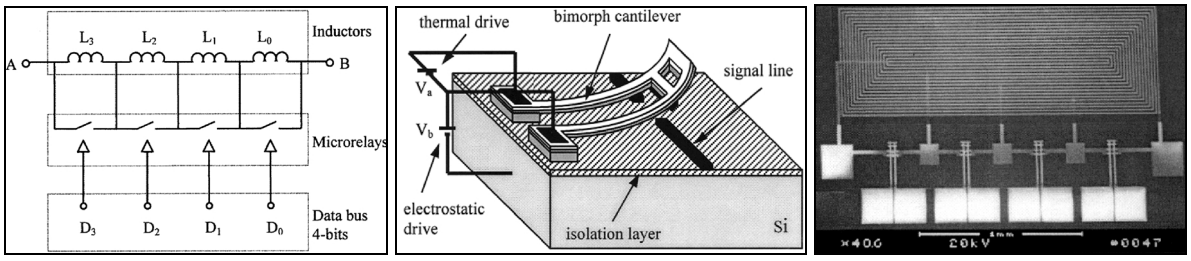

Figure 45: switched tunable inductor using micro-relays actuated by electrothemal and electrostatics forces

The MESA technique has been used to elevate inductors above lossy substrates, using SDA's to exert high forces on hinged structures as shown in Figure 46.[90] The details of the RF performance of these inductors have not been published, and the current path must include the hinges and other high resistivity structures in series with the inductors.

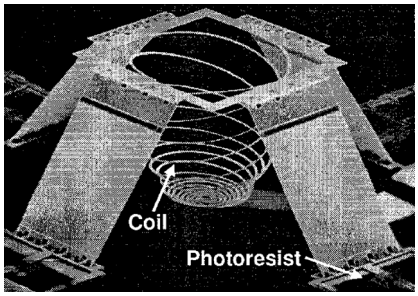

Figure 46: coil assembled with MESA technique

More recently, a cubic millimeter power inductor was fabricated on polyamide flexible substrates, with electroplated copper coils and a micromachined ferrite core was fabricated and characterized at below 10 MHz. The device has a Q factor below 1, and an inductance of approximately 100 uH at frequencies up to 0.1 MHz.[91]

The PDMA technique has been used to assemble planar inductors perpendicular to the substrate. This method was described earlier as a self-assembly technique, and is applied here in order to reduce substrate losses, as shown in Figure 47. The losses associated with the silicon substrate, as shown on the Smith Chart, are quite substantial. The self-resonant frequency increases from 1 GHz to well above 4 GHz, and the peak Q factor of 3.5 increases to 12 when the device is in its assembled position.

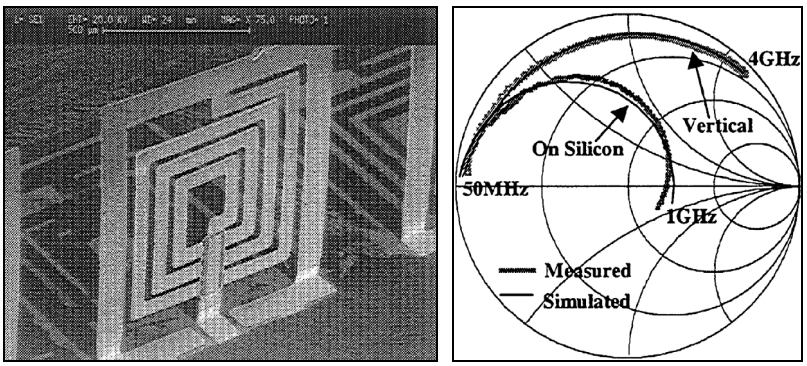

Figure 47: PDMA inductor in assembled position (left) and Smith Chart showing reduction of losses with assembly

The use of innovative microfabrication techniques has facilitated the construction of highly suspended spiral inductors with reported Q's of 70 at 6 GHz, which is a very high value for MEMS inductors. The inductor shown in Figure 48 was fabricated using a thick photoresist layer (AZ9260) that was exposed twice – one patterning step defines the deep features (posts) and the other defines

the suspended inductor structure – and then developed in a single step. The 3-D photoresist structure that remains acts as a mold for copper electroplating, vacuum deposition, and polishing.[92]

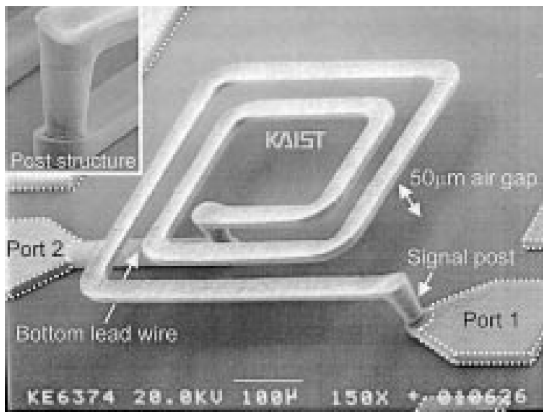

Figure 48: High Q elevated inductor

The built-in stress mismatch that exists between thin films often results in a curvature of structures upon release. Control of process parameters can provide some degree of control over the final stress in the films, and thus the curvature can be varied. This phenomenon has been used to "self assemble" inductive structures consisting of metal and polysilicon. Significant deformations require large structures, such as those shown in Figure 49.[93]

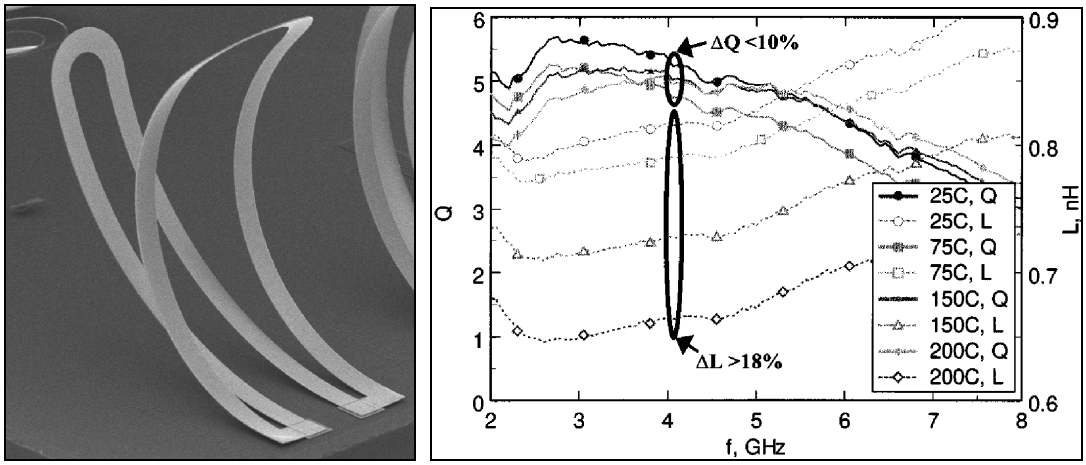

Figure 49: SEM picture of self-assembled inductor (left) and graph showing Q factor and inductance as a function of temperature

Hinged versions of this structure were fabricated to achieve Q's greater than 13, self-resonant frequencies well above 15 GHz, and inductance variations greater than 18%. In order to vary the

device geometry, the authors chose to control the ambient temperature rather then actuate the devices based on the bimorph principle. Furthermore the plastic deformation of the gold layer, which must occur at the high temperatures and stresses discussed, was not mentioned in the publications. The structures are typically ~1mm in length, and the gold layer is 0.5 um thick. The reduction in substrate losses is clearly demonstrated in the graph, since the Q curves are lower when the device is flat on the substrate at higher temperatures.

2.4 Optical MEMS

The area of optical MEMS, often referred to as Micro Optical Electro Mechanical Systems (MOEMS), is the subject of several well-established conferences, large research initiatives, and textbooks of selected papers that provide a thorough coverage of the field.[94] The applications include micromirror and micro grating display devices, adaptive optics, beam scanning and steering, imaging and spectroscopy systems, optical switches, variable optical attenuators, passive fiber alignment structures, tunable filters, lasers and detectors. This review will focus on the development of micromirrors and periodic structures.

2.4.1 Micromirror Devices

Perhaps the most familiar application of MOEMS is the torsional micromirror array developed by TI for high-resolution display applications. Arrays containing over 2 million devices are being shipped, with integrated electronics and carefully designed vacuum packaging. Over a decade of research and development was required to develop the process and design the version of the device that is used in data projectors and cinemas today. The unit cell is a $16um^2$ mirror placed on top of a torsional electrostatic actuator capable of +/-10 degrees of angular deflection (see Figure 1 for cutaway image of device).[95]

Phase-only micromirror arrays with piston-style actuation have been developed using electrostatic and thermal bimorph actuation.[96,97] These devices can be used for small angles of beam steering using the phase array method common in antennas, or more commonly in adaptive optics applications. Although the image in Figure 1 shows a discrete structure consisting of an array of mechanically uncoupled actuators, several continuous membrane deformable mirrors have been developed as well.[98]

Scanning optical mirrors for beam steering and optical switching applications have been thoroughly developed in academic and corporate research settings for over a decade. Many designs

are electrostatic and provide limited angular displacements unless they are driven at resonance. Also, since the devices are typically fabricated in planar surface micromachining processes, the maximum angle of actuation is limited by mechanical interference of the substrate with the mirror surface. Some techniques that have been used to circumvent these limitations are discussed here.

Hinged mirrors on stepping rotator platforms can provide large steering angles.[99] Electrothermal or electrostatic actuation is normally used to rotate the platform, or to actuate a hinged mirror. This method has several drawbacks – the assembly required for the hinged structure is tedious, the sliding contacts are unreliable and can fail due to stiction or wear, the scanning speeds are slow since a large number of actuation steps are required to achieve appreciable motion, and a high resolution of motion is difficult to achieve due to the stepped nature of the mechanisms. Hinged structures that are directly actuated provide a lower scan angle but can provide continuous displacement control.[100]

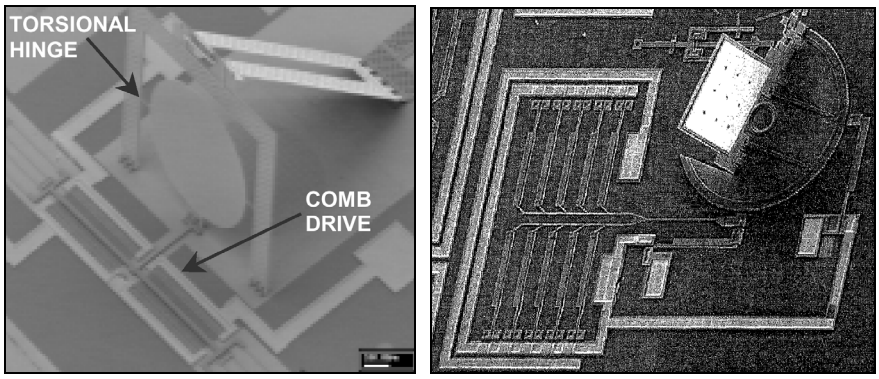

Figure 50: scanning hinged micromirror (left) and hinged mirror mounted on rotating platform (right)

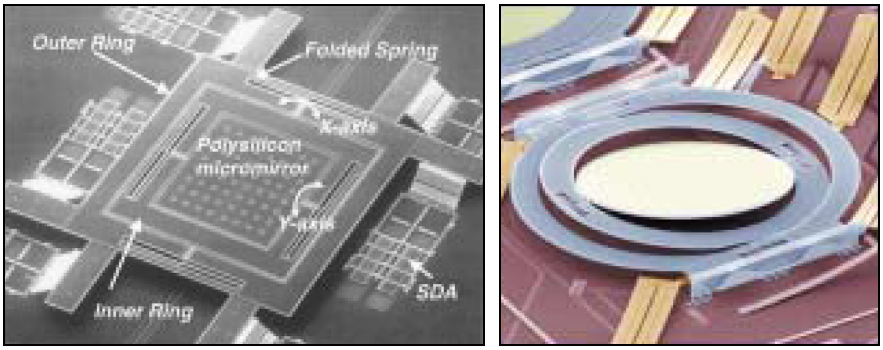

Figure 51: 2-D scanning mirrors elevated with SDA's (left) and built-in stress (right)

Two-dimensional torsional mirror mechanisms, or gimbal mount mirrors, have been implemented by several groups as well. Electrostatic actuation is used to control the 2-axis mirrors and large scanning angles can be achieved with high voltages. At Lucent, a self-assembly method has been used to elevate the 2-axis mirrors before actuation. Stress induced deformation of a beam is used to elevate the hinged gimbal mount structure shown above in Figure 51. The MESA technique has been used to achieve the same function and is shown as well.[101] Solder self assembly of torsional micromirrors has been performed as well.[102]

Magnetic actuation has been used to make scanning mirror structures, and one implementation is shown in Figure 52.[103] This device makes use of an integrated coil and a NiFe film as a structural material for the mirror plate. Due to the large size of the device, the resonance occurs at ~200 Hz, but a large scanning angle can be achieved.

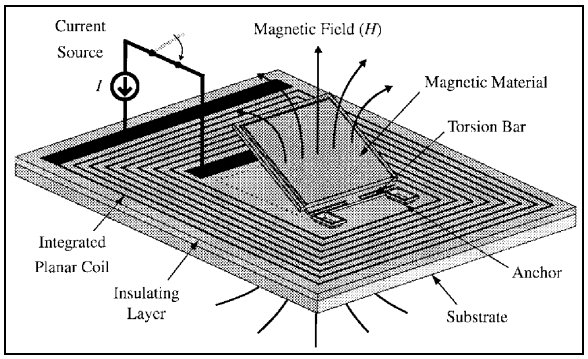

Figure 52: Magnetic actuation of micromirror

Magnetostrictive actuation and vertical electrostatic comb drive structures have also been used to achieve dual and single axis scanning micro mirror structures. In vacuum, the magnetostrictive scanners can resonate at over 13 KHz, with a maximum measured deflection of 24 degrees. The devices require a relatively large magnetic field to operate, and due to the size of the structure, its performance in air is significantly compromised. The device can only be operated at resonance to achieve appreciable deflections, and 2-axis control is possible because the torsional mode and lateral mode occur at different frequencies.[104]

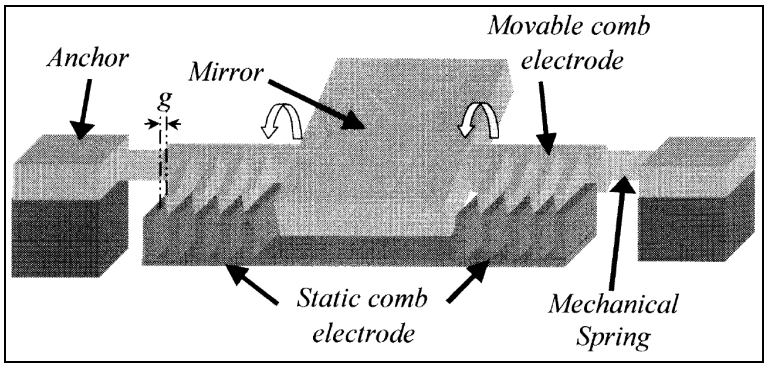

Figure 53: vertical electrostatic comb actuated mirror

Vertical comb drives make use of a set of interdigitated combs that are at different elevations. The upper set is supported by a torsional spring and contains the mirror surface, as shown in Figure 53. Static deflections of about 4 degrees were measured, and resonant deflections of 40 degrees can be achieved with an actuation voltage of 75 volts, at 5.6 KHz for this particular device.

2.4.2 Micro grating structures

Variable periodic structures with dimensions similar to the wavelength of the incoming light have a large number of applications including spectroscopy, displays, tunable filters, beam scanning, and collimation. In the case of linear gratings, most research has focused on the variation of the vertical height of individual elements, or the angle of the grating surface with respect to the incoming beam. In one case, a variable blaze grating was fabricated in which the individual elements could be tilted individually. More recently, in concurrence with the research presented here, the period of the grating has been varied to achieve tuning. To the best of the author's knowledge, there has been no MEMS progress in the area of 2-dimensional periodic structures with optical applications.

The geometry of micro fabricated gratings is limited by the critical dimensions achievable with lithography, and so the periods are usually ~5 um with most MEMS processes that have been available; however, the trend of decreasing minimum feature sizes and the availability of nanolithography techniques has made the fabrication of gratings with much smaller dimensions possible, making these designs practical. Another possibility would be the directed assembly of a ruled grating (with optimal geometry) onto a rotating MEMS actuator.

The grating light valve (GLV) developed by Silicon Light Machines is based on a diffraction effect controlled by vertical electrostatic actuation of an array of doubly clamped beams.[105] Initially all the beams are at the same vertical elevation, and when a pixel is actuated, every alternate beam is at a vertical displacement corresponding to $\lambda/2$ of the illuminating wavelength. This reduces the reflected light intensity and increases the diffracted intensity as shown in the simplified diagram in Figure 54.

This device has been used in commercially available projection displays and has been cycled over 210 billion times with no indication of ribbon fatigue. In some GLV prototypes, over 80% of the incident light can be collected in the +/- 1st diffracted order in the "bright state."

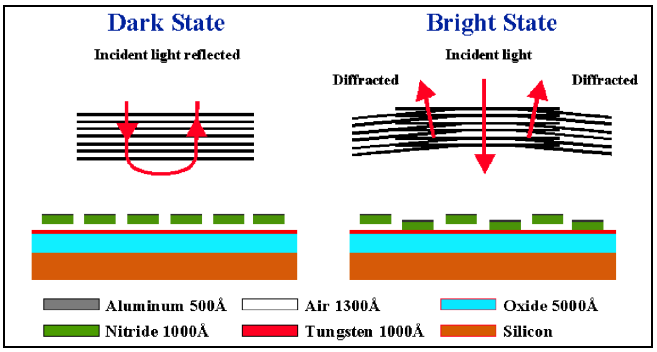

Figure 54: Grating light valve operating principle

Grating microscanners have been fabricated based on in plane rotation of a patterned surface. The rotating circular surface contains four quadrants with orthogonally oriented gratings. The quality of the surface of the gratings can be improved with chemical mechanical polishing (CMP) and bar code scanning applications have been implemented with the device in question.[106] These scanners suffer from drawbacks related to the micromotor reliability issues discussed above. Also, the direction of the scanning is limited by the single planar rotational degree of freedom that the motor can provide – each of the orders traces out an arc corresponding to its angle and the incident angle of the incoming beam.

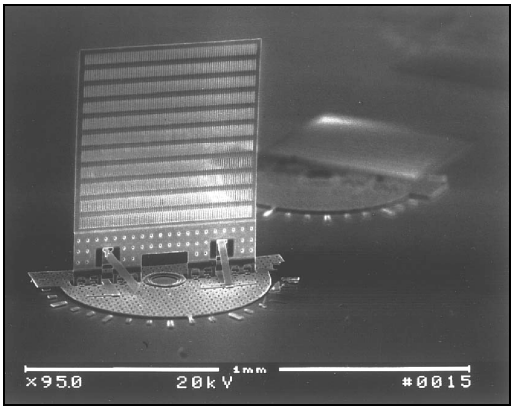

Figure 55: hinged grating assembled on rotating platform

Hinged gratings that are mounted on rotating platforms have been designed as well, and they have been used to adjust the absolute position of the far field patterns associated with the grating geometries. One example of this type of device is shown in Figure 55.[107] These devices suffer from the same drawbacks as the rotating mirrors that are based on the same design. The hinges, sliding contacts, and imprecise actuation mechanisms make such devices impractical for most applications. Recently, variable period optical gratings have been fabricated in which the grating can be compressed or expanded, since the elements are all interconnected with springs.[108] The far field pattern, which can be thought of as the Fourier transform of the grating geometry, is a sinc function whose spatial frequency is inversely proportional to the grating period. A more thorough discussion of these devices is included in the optics chapter below.

Chapter 3
Actuator Design

MEMS can interact with their environments by means of actuation. Methods of converting electrical signals to a desired motion are based on various physical phenomena, and the most practical transducers make use of the favorable scaling of forces into the micro domain. Some of the metrics used in order to compare actuator designs include efficiency, amplitude of displacement, force, operating voltage, footprint, reliability, simplicity of fabrication, and general robustness.
In some cases, the actuation principle is easily determined by the geometry of the device being designed. For instance, in the case of membrane capacitors used as RF switches, electrostatic actuation is a natural choice. However, in most cases there are several options of actuation methods that can all satisfy requirements to varying degrees, and the optimal choice is not always obvious. For the devices developed in this research, the most appropriate actuation mechanism was selected in a rational manner based on the metrics discussed above. Existing actuation methods were not able to provide the large angular and linear static displacements that were required. Furthermore, low actuation voltages, reliability, small footprints, and self-assembly capabilities were desired. The following tables illustrate the rationale behind the choice of electrothermal actuation, and justify the design of novel actuator geometries in order to meet the requirements shown in the tables.

Table 2: Requirements for in-plane linear actuation

Requirements for in-plane linear actuation	Approximate values
Large static displacements	30 um
High forces	100 uN
small footprints	largest dimension <500um
Low operating voltage	<10 V
Reliable	>100 million cycles
simple fabrication process	Standard materials, 1-2 layers, <5 masks
multiple degrees of freedom	x,y

Table 3: Qualitative comparison of linear actuation mechanisms

Actuation type	Advantages	Disadvantages
Comb drive	low power, simple structure, reliable, can be coupled to achieve x,y	high voltage, low force, large footprint, small static displacement (resonant displacements are much larger)
parallel plate	low power, simple structure, reliable, large forces possible	high voltage, low force, large footprint, small displacement, single degree of freedom,
scratch drive	low power, high force, long travel possible, simple geometry, small footprint	unreliable, high voltage, step size not consistent
single, double and triple arm u-shaped bimorphs	low voltage, small footprint, high force, moderate static displacement, simple geometry, reliable, multiple degrees of freedom	inefficient, moderate displacements
bent beam	low voltage, small footprint, high force, simple geometry, reliable, multiple degrees of freedom	small displacement
cascaded bent beam	low voltage, high force, simple geometry, reliable, multiple degrees of freedom, large displacement	large footprint, Increased power consumption
flexure-amplified bent beam	low voltage, high force, simple geometry, reliable, multiple degrees of freedom, large displacement, moderate footprint	Increased power consumption
impact drive	high force, long travel possible, simple geometry, small footprint	reliability data scarce, exotic processing, inefficient, large footprint due to mass, analog position control not possible
magnetic	large displacement, moderate forces, low voltage, reliable, small footprints possible	electromagnetic does not scale well, uncommon materials, direction of actuation determined by field (multiple DOF difficult), large footprints in some designs, in plane actuation less common than out of plane
piezoelectric	high force, simple geometry, low power, multiple degrees of freedom, reliable	small displacement, exotic materials, high voltage, often large footprints,
topology optimized electrothermal	low voltage, high force, simple geometry, reliable, multiple degrees of freedom, large displacement, moderate footprint	Increased power consumption

Table 4: Requirements for angular actuation

Requirements for in-plane linear actuation	Approximate values
Large static displacements	90 degrees
Self assembly to avoid contact with substrate	
small footprints	largest dimension <500um
Low operating voltage	<10 V
Reliable	>100 million cycles
simple fabrication process	Standard materials, 1-2 layers, <5 masks
multiple degrees of freedom	Theta, Phi

Table 5: Qualitative comparison of angular actuation mechanisms

Actuation type	pros	cons
resonant bimorph	Self assembly possible, small footprint, low voltage, reliable, simple fabrication, simple process, low power	large static deflection difficult, multiple decoupled DOF not demonstrated
torsional	Self assembly possible, small footprint, reliable, simple fabrication, low power	single axis, large static deflection difficult, high voltage
gimbal	Self assembly possible, small footprint, reliable, simple fabrication, dual axis, low power	large static deflection difficult, high voltage
tpda	Self assembly possible, small footprint, reliable, simple fabrication, dual axis, large static deflection	higher power for static deflection
electromagnetic	Self assembly possible, reliable, simple fabrication, large static deflection	larger footprint typical, dual axis difficult, requires magnetic materials in processing, high power required for external field
hinged	Self assembly possible, small footprint, simple fabrication, large static deflection	dual axis difficult, sliding contacts,
piezoelectric	precise control of angle, low power, reliable	Self assembly not demonstrated, small static deflections, large footprint, unconventional materials, high voltage
magnetostrictive	precise control of angle, reliable	Self assembly not demonstrated, small static deflections, large footprint, unconventional materials, high power

Although several types of actuators were designed, fabricated and characterized during the course of this research, most of the RF and optical devices were based on electrothermal actuation of some kind. A novel flexure-amplified bent beam structure was designed in order to provide large static displacements and high forces in x, y, and z directions. Large angular deflection was implemented using several TPDA (thermal plastic deformation assembly) designs, based on cascaded arrangements of bimorph beams of gold and polysilicon. The TPDA designs are self-assembled and subsequently actuated. This chapter focuses on the procedure that was developed in order to design electrothermal actuators.

3.1 Electrothermal Material Properties

The most crucial element governing the quantitative usefulness of FEA simulations of MEMS structures is a well-established set of material properties. In the case of electrothermal simulations, in order for an FEA solution to be in good agreement with measured results one must first establish accurate numerical values for material properties such as electrical and thermal conductivity, and then determine the nature of their temperature dependence.

For this reason, a considerable amount of effort has been placed on characterizing temperature dependant material properties in MEMS. The work presented in the following sections has been published in the literature,[109] and a summary has been included in the body of this thesis, since the author made extensive use of the results in the design of actuators and devices.
The following sections describe the method that was used to extract electrothermal material property values for polysilicon using a unique test structure.[109] These extracted values are used in a 3-D FEA model, which is compared to measured data for the flexure-amplified bent-beam structure.
First, the electrical and thermal conduction properties of polysilicon are investigated, and general parametric equations for these properties as a function of temperature are established.

3.1.1 Electrical Conduction

In general, for the low to moderate dopant levels ($< 10^{18}$ cm^{-3}) used in integrated circuit fabrication technology with single crystal silicon (SCS), a negative temperature coefficient of resistivity (TCR) is expected because increased temperature excites dopant electrons from the valence to the conduction band. This temperature dependent behavior can create an electrothermal instability called “thermal runaway” that is undesirable in thermal actuators.

To exemplify this behaviour we consider the simple example of a bimorph with a step input of constant electrical voltage. The joule heating resulting from the input voltage decreases the resistivity of the device (due to the negative TCR), and increases the current consumption. Concurrently, the power consumption increases (P=V*I) and the device temperature rises further. The uncontrolled increase in temperature can result in catastrophic burnout failure of the device under these conditions.

Thus, dopant levels for thermal actuators are generally high enough to ensure that electron and hole scattering from thermal vibrations dominate over the effects from increases in charge carrier concentration. The resulting positive TCR causes a linear increase in resistance, and has been used as a general resistivity model for SCS and polysilicon from 300 to 800K. [110,111]
The comprehensive model adopted here makes use of the thermal dependence of electron and hole mobilities in order to capture the variation of the TCR with respect to temperature, and neglects the effects of charge trapping at grain boundaries. The expression for resistivity in SCS is:

$$\frac{1}{\rho} = \rho|e|(\mu_e + \mu_h)$$

where ρ is the free electron concentration, e is the magnitude of electron charge and μ_e and μ_h are the electron and hole mobility, respectively. As mentioned previously the free electron concentration will increase with temperature; however, for high doping levels the effects from donor activation in silicon vanish due to the large number of electrons already in the conduction band. At these doping levels the temperature dependent behavior is dominated by mobility. Lattice and impurity scattering mobility, μ_L and μ_I respectively, significantly contribute to charge carrier mobility at high temperatures and impurity concentrations.[112,113] The lattice scattering term is found to have the form

$$\mu_L \propto T^a$$

where $-2.7 < a < -1.5$. In addition, the effect of ionized impurities has a similar form

$$\mu_I \propto T^b$$

where $1.5 < b < 2$. Using this rationale, a general equation for the temperature dependent resistivity within polysilicon and SCS is taken to be

$$\rho(T) = \alpha_1 + \alpha_2 T^{\alpha_3} \quad (1)$$

where α_1, α_2 and α_3 are parameters that will later be extracted from experimental data. This general equation is also fitted to experimental data obtained by Manginell.[112]

3.1.2 Thermal Conduction

Dopant concentration also influences the thermal conductivities of SCS and polysilicon. Furthermore, grain size within polysilicon contributes to thermal conductivity.[114]

Lattice phonon conduction carries most thermal energy within semiconductors, including silicon.[112],[115] If the material is considered to be isotropic, a general form of the thermal conductivity is given by the Boltzmann transport equation:

$$K \approx \frac{k_B}{2\pi^2 V}\left(\frac{k_B}{\hbar}\right)^3 T^3 \int_0^{\frac{\theta_D}{T}} \tau_c \frac{x^4 e^x}{\left(e^x - 1\right)^2} dx \tag{2}$$

where

k_B is the Boltzmann constant,

$\hbar$ is Planck's constant,

θ_D is the Debye temperature,

V is the average phonon velocity in silicon,

τ_c is the relaxation time, which has contributions from several factors discussed below.

Finally,

$$x = \frac{\hbar\omega}{k_B T}$$

is a nondimensional parameter where ω is the phonon frequency. This parameter gives rise to the frequency dependence of the Boltzmann transport equation.

The relaxation time τ_c has contributions from three significant factors that impede phonon transport:

$$\tau_u^{-1} = u e^{\frac{-\theta_d}{3T}} \omega^2 T$$

is the relaxation time that represents phonon-phonon scattering,

$$\tau_d^{-1} = d\omega^4$$

is the relaxation time that represents the contribution of dopants and

$$\tau_g^{-1} = g\omega^2$$

is the relaxation time that incorporates contributions from grain boundaries.

The parameters *u, d* and *g* control the shape of the thermal conduction function and will be extracted from experimental data.

Before proceeding with the parameter identification, we can simplify the transport equation into a closed form expression by considering the limits on the integral at high temperatures, and assuming that the range of x is fairly small.[116]

We can expand the integral to obtain:

$$\int_0^{\frac{\theta_D}{T}} \tau_c \frac{x^4 e^x}{\left(e^x-1\right)^2} dx \approx \int_0^{\frac{\theta_D}{T}} \tau_c \frac{x^4\left(1+x+...\right)}{\left(1+x+...-1\right)^2} dx \approx \int_0^{\frac{\theta_D}{T}} \tau_c x^2 dx.$$

Now, the time constants contributing to τ_c can be summed using Matthiessen's rule

$$\tau_c^{-1} = \tau_u^{-1} + \tau_d^{-1} + \tau_g^{-1}$$

such that they can be incorporated into the simplified transport equation as follows:

$$K(T) \approx \frac{k_B}{2\pi^2 V d}\left(\frac{k_B}{\hbar}\right)^{-1} T^{-1}\left(\frac{1}{\sqrt{\beta}}\tan^{-1}\left(\frac{\theta_D}{T\sqrt{\beta}}\right)\right)$$

where

$$\beta = \frac{ue^{\frac{\theta_D}{3T}} + g}{dT^2\left(\frac{k_B}{\hbar}\right)^2}$$

This expression is used to represent the thermal conductivity within SCS and polysilicon. This closed-form solution is also compared to the full numerical integration of the original form to validate the simplifying assumptions once the parameters are identified.

3.1.3 Specific Heat

For the purposes of transient thermal analysis, the specific heat of polysilicon is required. It is reasonable to assume that this value is close to that of SCS, and this has been confirmed with measurements and theory.[112] Since phonons dominate thermal energy transport in silicon, the heat capacity can be represented as a function of the vibrational modes within the crystal. The Debye specific heat is [116]

$$c_p = 9\frac{R}{A}\left(\frac{T}{\theta_D}\right)^3 \int_0^{\frac{\theta_D}{T}} \frac{x^4 e^x}{\left(e^x-1\right)^2} dx$$

where R is the gas constant and A is the atomic weight for silicon. This function is used to obtain the Debye heat capacity in the transient simulations that are performed later.

3.1.4 Other Material Properties

In addition to the electrical resistivity, thermal conductivity and specific heat, other physical properties that are required in electrothermal-structural simulations are listed below in Table 6. Since the dopant levels and grain boundaries found in our polysilicon material do not influence the CTE, values for SCS are used. Also, the Young's modulus and Poisson's ratio are not considered to vary as a function of temperature. Since the density is applied to the thermal-structural simulation after the thermal distribution is solved, its variation with temperature does not significantly affect the FEA results.

Table 6: Polysilicon material properties

Physical Property	Temperature (K)	Value
TCE (1/K)	300	2.5×10^{-6}
	400	3.1×10^{-6}
	500	3.5×10^{-6}
	600	3.8×10^{-6}
	700	4.1×10^{-6}
	800	4.3×10^{-6}
Young's Modulus		160 GPa
Density		2330 kg/m^3
Poisson's Ratio		0.22

3.1.5 Electrothermal Parameter Extraction from Measurements

This section describes the experimental techniques that were used in order to extract the parameters in the electrical and thermal conduction equations discussed above.

The first parameter extracted is the phonon-phonon scattering term u, since this parameter can be readily extracted from thermal conductivity data of SCS found in material properties handbooks.[117] We set the grain boundary parameter g to zero, the Debye temperature to 640K, and the average phonon velocity to 6.16×10^3 m/s, and plot the best fit parameters to the handbook data as shown in Figure 56. We thus obtain a phonon-phonon scattering parameter of 3.35×10^{19} s/K.

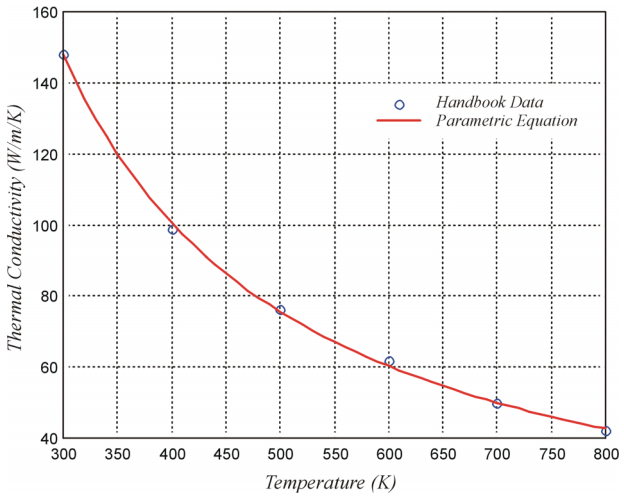

Figure 56:extraction of phonon-phonon scattering parameter

When extracting thermal conductivity from polysilicon, we can fix this value for *u* since only the dopant and grain boundary terms will vary between SCS and polysilicon.

The five parameters that remain to be determined are the dopant and grain boundary scattering parameters and the three electrical conductivity parameters in (1). A specially designed four-point-probe measurement device is introduced here in order to obtain measurements to extract these parameters. The device includes four 60 x 3 x 3.5 μm beams that support a central 40 x 9 x 3.5 μm beam at a vertical level of 2 μm above the substrate, as shown in Figure 57 below.

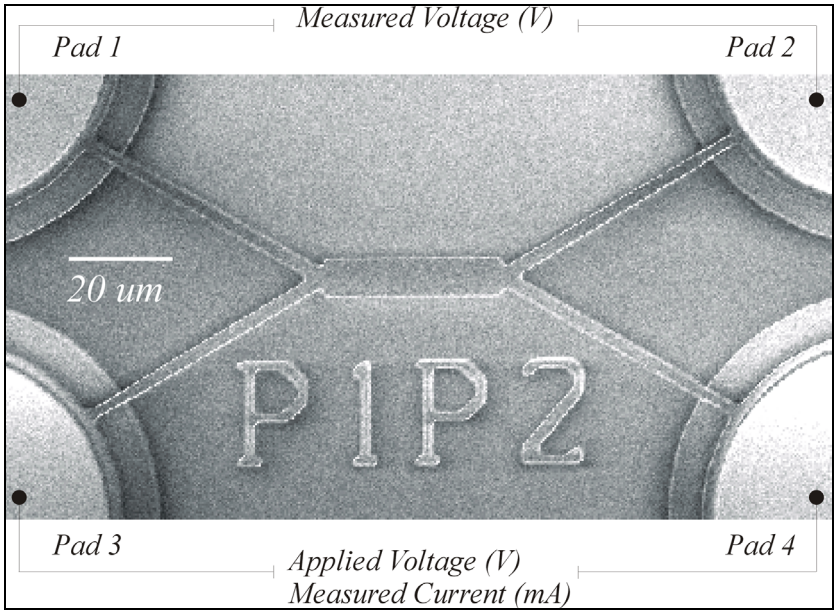

Figure 57: 4-probe test device

The device is fabricated using the MUMPs process, and consists of n-type heavily doped polysilicon. The current due to a constant applied voltage flows between pads 3 and 4, and the voltage is measured across pads 1 and 2.

The rationale behind the design of this structure is to increase the temperature within the main thermal mass by Joule heating, and measure its resistance as a function of temperature. FEA was performed to confirm that this geometry would result in a homogenous temperature distribution within the supported thermal mass. The results of this analysis are shown below in Figure 58. These results simply confirm that the geometry results in the displayed thermal distribution, and are not meant to be quantitative.

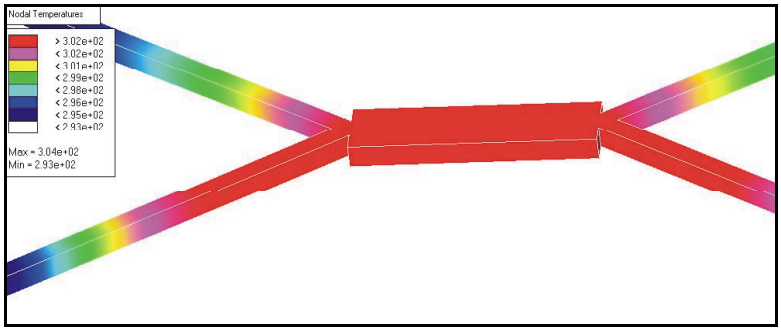

Figure 58: FEA results showing temperature distribution

Details of the iterative reduced order FEA model that was developed in order to extract the five parameters from four-point probe measurements can be found in the publication[109]. Table 7 lists the numerical values that were determined using this method.

Table 7: Parameters extracted from 4-point probe measurements

Parameter	Final Value
α_1	2.6×10^{-3}
α_2	8.16×10^{-9}
α_2	1.946
d	7.46×10^{-45}
g	8.14×10^{-17}

The values obtained in Table 1 were used in an optimized simulation, with results plotted against the measured experimental values in Figure 59 below. The extracted curves for temperature dependant resistivity and thermal conductivity are shown in Figure 59 below as well.

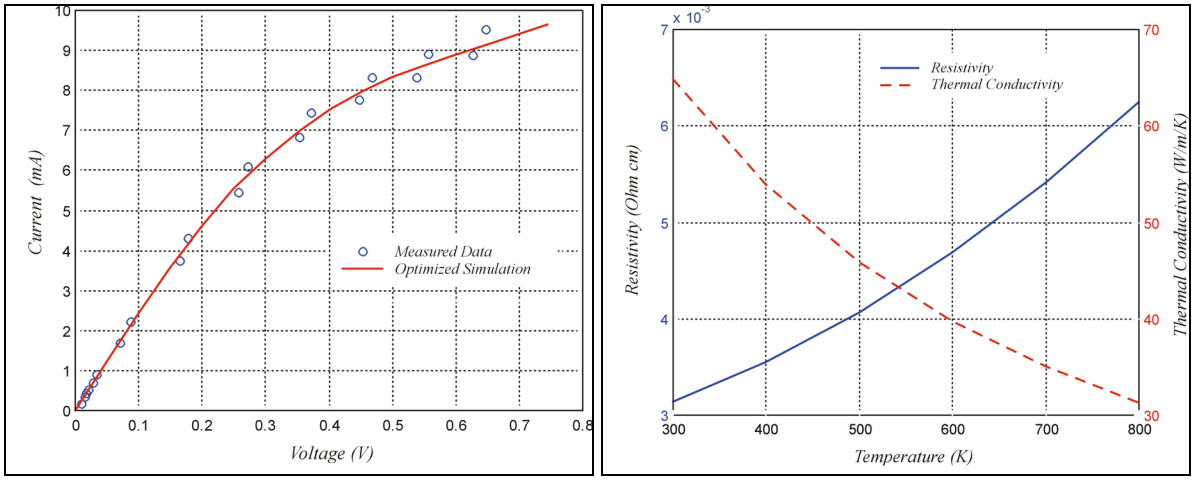

Figure 59: plots showing data fitted to IV curve, electrical resistivity and thermal conductivity

3.2 3D FEA method Applied to a novel Electrothermal Actuator

An effective 3-D modeling technique that considers convection and conduction is now used with the material properties developed in the preceding section. As evidenced by the contrast between vacuum and ambient measurements, the air surrounding the actuator plays a significant role in its performance.[118] This is due to convective and conductive heat transfer from the surfaces into the surrounding air. It has been determined that the viscous forces between the gaps and spaces in the actuator are significant enough to prevent air currents.[109] In the simulation, thermally conductive air elements are placed in these gaps as well as in the region between the substrate and the actuator. For the top surface, a temperature dependent convection coefficient is computed using FLOTRAN, a commercially available computational fluid dynamics (CFD) software. An example of the temperature distribution of a thermal bimorph in ambient conditions, and more details of its simulation are presented in [109].

3.2.1 Flexure-Amplified Bent Beam Geometry

The actuator discussed in this section makes use of a unique geometry in order to achieve the metrics specified in Table 1. Several embodiments of the flexure-amplified bent beam layout are shown below in Figure 60. These images are screen captures of the predicted performance of the

actuators using the FEA methods discussed above. Large static displacements are obtainable in or out of plane, by making use of a flexure to amplify the displacement provided by a standard bent-beam actuator bank. Among the geometries that have been designed, fabricated and characterized are the "push type", the "pull-type" and the out-of-plane type shown in Figure 60. Simulation results for the push type are presented here, and compared to measurements. The pull-type actuator provides a slightly larger displacement with the same input power, and this can be explained qualitatively with the following reasoning. The longer beam buckles under compressive loading, and detracts from the in-plane displacement in the case of the push type actuator - this occurs for the shorter beam in the case of the pull type actuator. Thus, the total displacement lost due to the buckling is lower in the case of the pull type actuator. A more comprehensive analysis of the system is provided by the FEA.

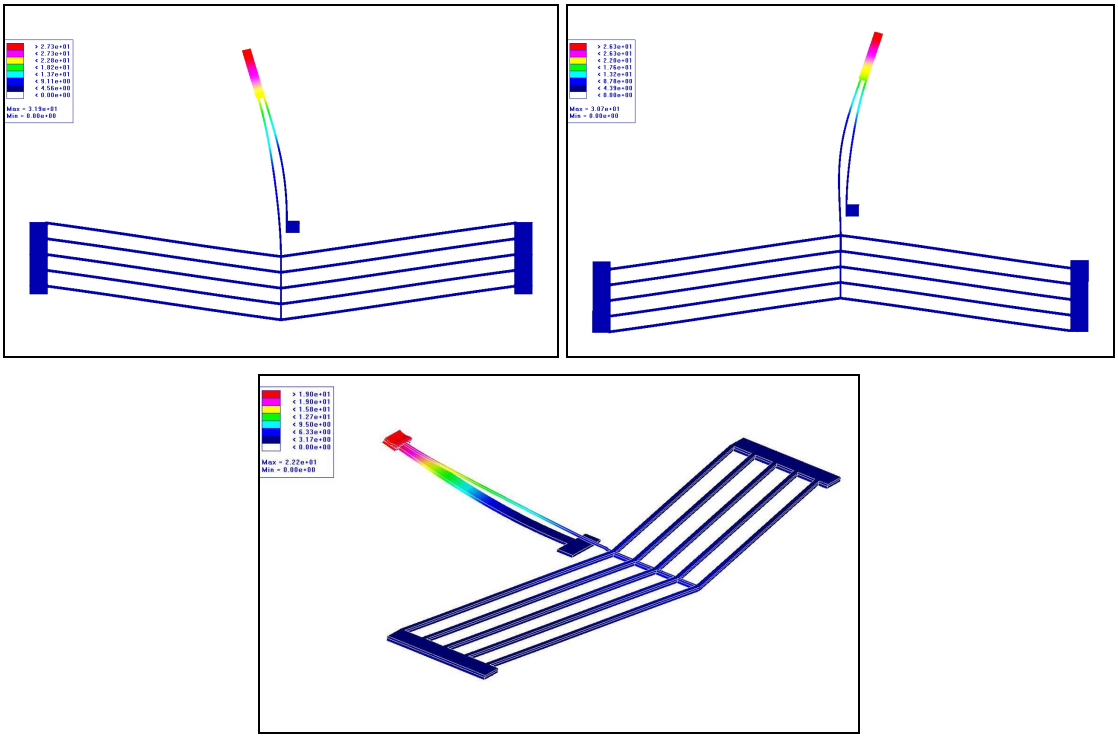

Figure 60: FEA of three flexure-amplified bent beam structures

The out-of-plane actuator has been characterized and produces similar displacements as well. An SEM picture of the push type amplified bent beam actuator that was simulated is shown below in Figure 61. The voltage is applied to the standard bent beam structure, which is electrothermally actuated. At the apex of the bent beams, a small displacement with high force is attainable. The displacement amplification structure labeled in the figure provides a geometric advantage of

approximately one order of magnitude. This structure extends 150 um above the apex and consists of a u-shaped arrangement of 2 beams that are 3 um wide and 3.5 um thick. The upward force at the base of the flexure gives rise to a counter-clockwise bending moment at the anchor and results in lateral motion of the tip towards the left in this diagram.

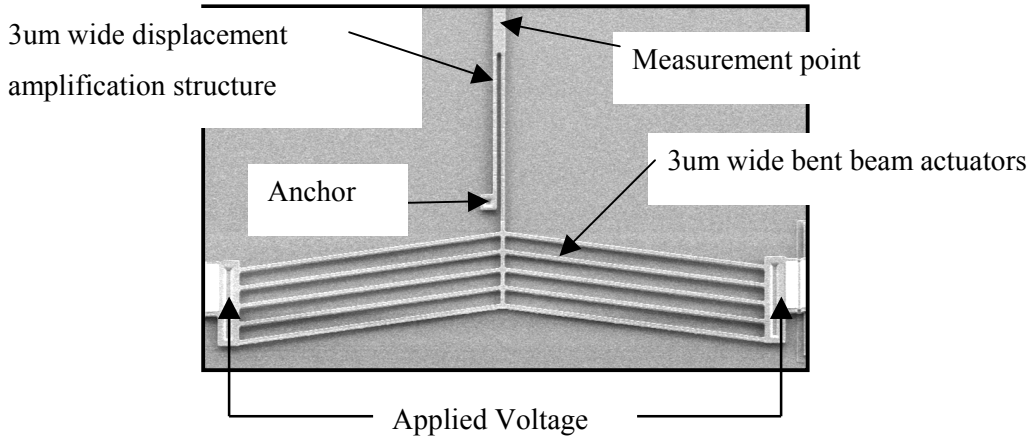

Figure 61: flexure-amplified bent beam geometry

Static measurements were performed using a 5Hz excitation while tracking the actuator tip motion to an applied voltage and monitoring current. The UMECH MEMS Motion Analyzer (see Appendix A) was used to obtain this data. Figure 62 (a) is a plot of the measured data compared with the 2 FEA simulations – one that includes the temperature-dependant electrothermal properties, and one that neglects them. It is apparent that the inclusion of temperature dependence yields a more accurate simulation. Figure 62 (b) shows compares the measured transient response of the actuator to those simulated. The measurements were conducted using a 7 V square pulse at 1 kHz, applied with 10, 20 and 30 % duty cycles.

The simulation results agree well with the static and transient displacements of several types of electrothermal actuators. Measured static power vs. displacement curves are within 10% of the simulated values, indicating that the rate of thermal energy conducted from the device is accurately predicted. This validates the temperature-dependent thermal conductivity equations, and the corresponding extracted parameters. In addition, the transient response of electrothermal actuators is shown to have a good correlation with simulations. This indicates that the temperature dependent

resistivity equation and extracted parameters are appropriate for the polysilicon used here. The shape of the simulated transient response also justifies the use of Debye specific heat equations for SCS when modeling polysilicon.

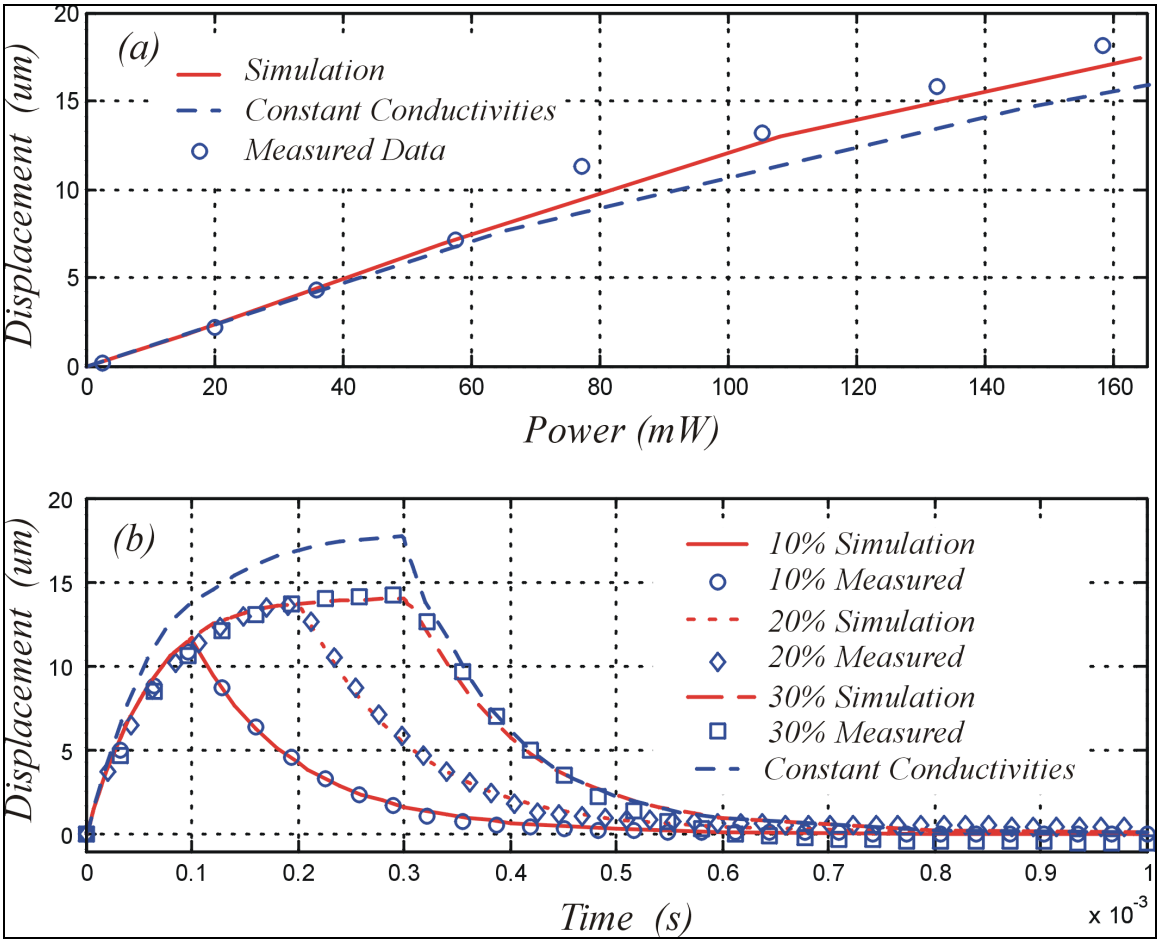

Figure 62: Data showing excellent agreement between measurements and simulations

Due to the fact that this actuator adequately meets the requirements listed in Table 1, it has been used extensively in the author's design of optical and RF structures, and in several designs of high force, large displacement tweezers that are in use in the development of microassembly technology at Zyvex. Another application of this actuator is shown below in Figure 63. This X-Y stage consists of four flexure-amplified bent beam actuators arranged orthogonally and connected to a central stage with mechanically-decoupling flexures. The stage has a range of 20 microns in X and Y, and has been characterized with the UMECH system. Differential and quadrant capacitive detection schemes were included in the design of the stages for closed-loop positional feedback.

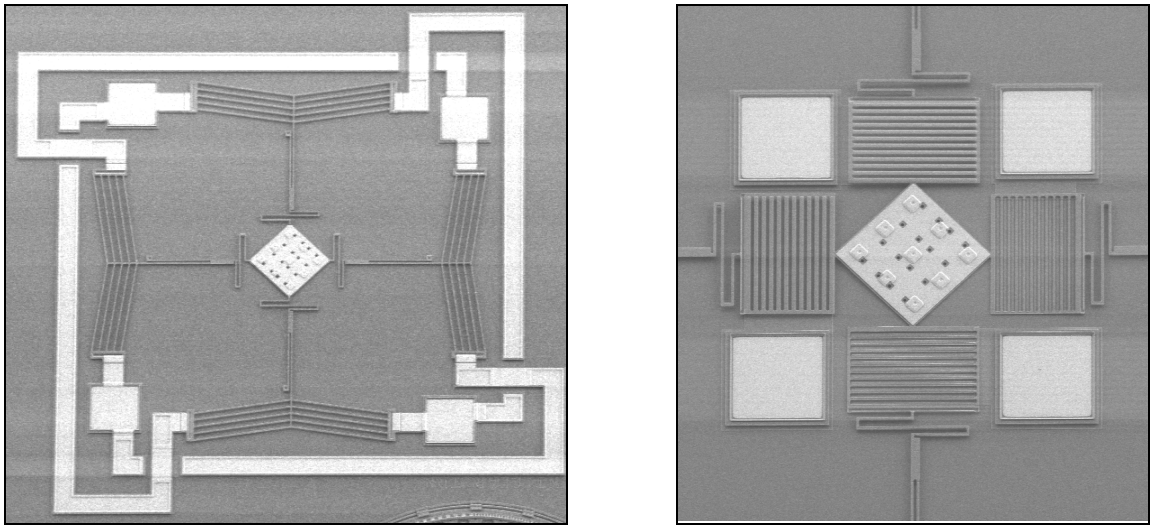

Figure 63: XY flexure stage (left) and differential capacitive positional feedback scheme (right)

Due to the flexure design and symmetric placement of the actuators, the mechanical coupling between the axes is negligible. Figure 64 shows that the coupling between the motion axes is below the resolution of the motion analysis system.

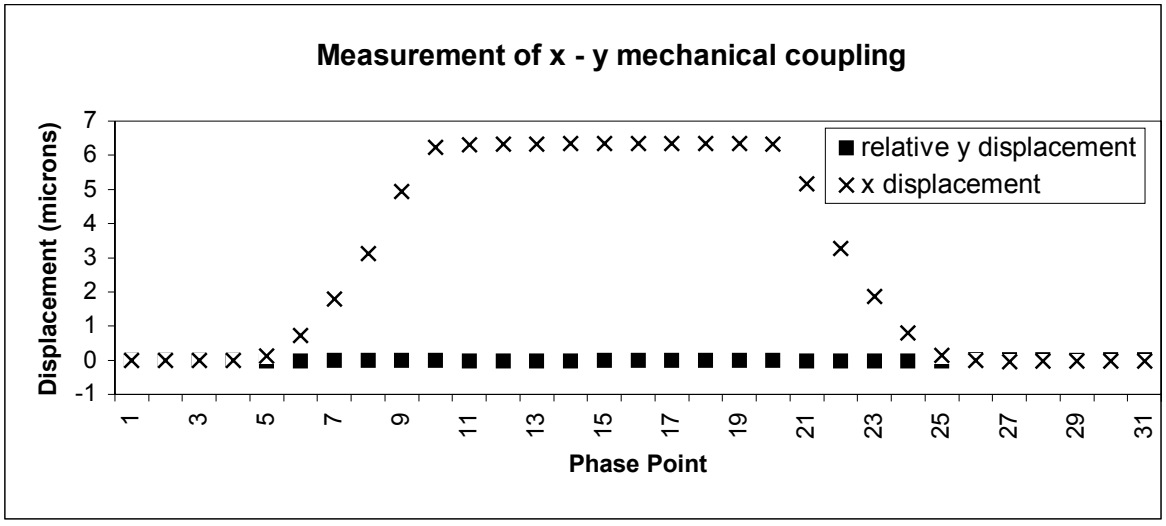

Figure 64: UMECH measurements showing low coupling between X and Y axes

This data was taken using a sloped square wave input to the x axis of the stage, and measuring the position in X and Y of a central region of interest on the stage. 32 measurements are taken over the period of 1 cycle, and this measurement was repeated at several Y offsets, and no increase in coupling was observed with increasing voltage offset.

3.3 Material Properties for Thermal Plastic Deformation Assembly

True three-dimensional geometries are difficult to obtain with surface micromachining due to the planar nature of the associated microfabrication processes. Hinges have been used in controlled assembly operations to obtain structures that are normal to the surface of the wafer.[119] In some cases the use of actuators, such as scratch drive actuators[120], can replace hand assembly that is common with fold-up polysilicon optical systems. Similarly, polysilicon reshaping techniques have been used to self-assemble complex 3D structures.[121] In general, it is desirable to simplify the assembly process and reduce the number of sliding contacts in all MEMS. Plastic Deformation Magnetic Assembly (PDMA) has been used to simultaneously erect devices out-of-plane in an elegant batch process[122]; however, it is difficult to actuate devices following the assembly step and independent assembly of nearby structures to varying angles is challenging as well. Interlayer stress resulting from the MUMPs fabrication process has been used to self-assemble inductive structures upon release[123]. Unfortunately, the stress mismatch between the layers is not consistent, and large angles of deformation require large structures. Directed assembly of complex microsystems using external micromanipulators has been proposed as well, and is a technology currently under development.[124]

The thermal plastic deformation assembly (TPDA) technique was initially developed in order to meet the proposed requirements for rotational actuation listed in Table 4 above. The first design was a serpentine geometry that achieved over 90 degrees of mechanical rotation in a small footprint. Subsequent to this design, several geometries have been conceived to provide a large range of motion in x, y, z, θ and φ. These designs also offer the ability to self-assemble structures to arbitrary positions through *permanent* plastic deformation, a feature that allows for tuning of RF devices, steering of optical beams, and designing of 3-D structures in general. This section begins with a description of the TPDA process implemented in polyMUMPs, which relies on the behaviour of gold under high stresses and at high temperatures. The relevant material properties are extracted using another unique test structure,[125] in order to develop a model for the plastic deformation process. These measurements are also used in a 3-D FEA model that is compared to the measured data for a TPDA device. The various geometries that have been implemented are then listed and discussed.

3.3.1 TPDA Basics

Figure 65 below graphically depicts the principle behind TPDA. Initially, a bimorph of gold and polysilicon fabricated using the MUMPs surface micromachining process assumes a planar geometry. When the temperature is increased, the difference in thermal expansion coefficients results

in a deflection of the bimorph in the direction shown. At high temperatures (~200 C) the metal layer yields under large compressive stresses from actuation. Upon relaxation as the temperature is lowered, the bimorph assumes a new geometry due to plastic deformation. When a current is passed through the beam, joule heating actuates the bimorph to return to its initial position.

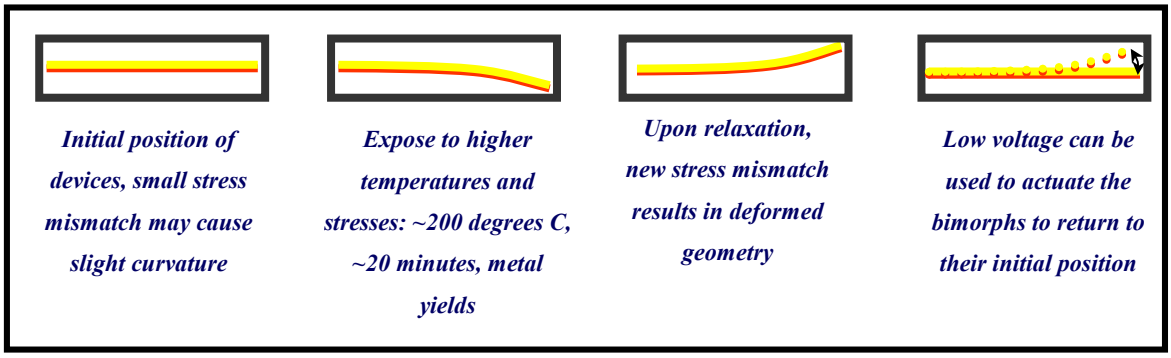

Figure 65: graphical depiction of TPDA process

The geometry shown below in Figure 66 provides a large out-of-plane rotation with a small footprint, and can be actuated with low voltages (~10V) to rotate 90 degrees in less than 1 millisecond. This is accomplished by cascading several of the bimorphs discussed above using a staggered helical geometry. The deflected tip of a bimorph is connected to another bimorph using a passive beam, and this process is repeated in order to obtain the desired motion by adding the deflections in series. In this figure, the payload of the actuator is a small (100 um x 200 um x 2 um) plate.

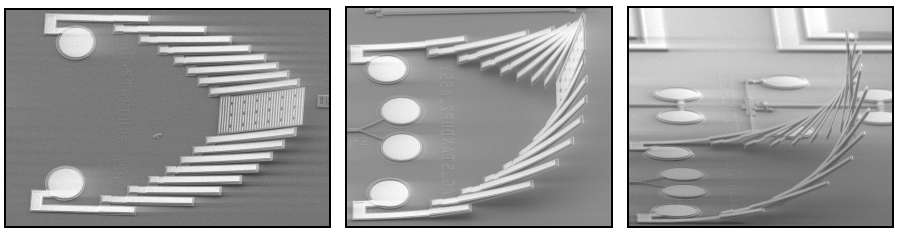

Figure 66: cascaded rotary actuator in initial position (left), partially self-assembled position (center), and fully deformed position (right).

An alternate method for self-assembly of these structures is to actuate them with an overdriving voltage instead of placing them in the oven. A series of voltage pulses can be used in order to assemble the device to varying deformed positions. Each voltage pulse can be controlled in amplitude and duration to tune the device's final rest position. Although this method can be carried

out in a single one second pulse, the drawback is that the device is not uniformly heated. Thermal conduction into the substrate maintains the bimorphs adjacent to the anchors of the device at a lower temperature than the bimorphs adjacent to the payload. This results in greater deformation towards the center of the device. Heating the entire substrate and actuator in an oven is a more time-consuming post-fabrication step; however, the equithermal nature of this method results in homogenous deformation throughout the device, and larger amplitudes of motion. Table 8 below lists the rest angle as a function of pulse amplitude and duration. Subsequent to the deformation process, a 9 volt pulse can be used to actuate the device through 90 degrees of mechanical motion to return it to its initial, as fabricated position.

Table 8: Self Assembly using joule heating

PULSE TRAIN FOR SELF ASSEMBLY			
Pulse Number	Voltage	Duration	Final Angle
1	12	1 second	40 degrees
2	12	1 second	45 degrees
3	14	1 second	60 degrees
4	14	1 second	65 degrees
5	16	1 second	90 degrees

3.3.2 Experimental Procedure and Analysis

A single bimorph of gold and polysilicon was used to characterize the plastic deformation process. This beam is fully released so that it can be removed from the wafer and packaged such that it is suspended in air. A u-shaped polysilicon heater is used to conductively heat the 200um x 20 um bimorph. The gold layer in polyMUMPs is 0.5 um thick, and the polysilicon layer is 1.5um thick. The actual procedure involves heating the bimorph using controlled voltage pulses and subsequently measuring its power-off position. Measurements were taken in vacuum in an SEM and in air with the UMECH. Figure 67 below shows an image of the measurement device, and an FEA capture of the simulated temperature distribution within the device, as well as a SEM picture of a vacuum measurement.

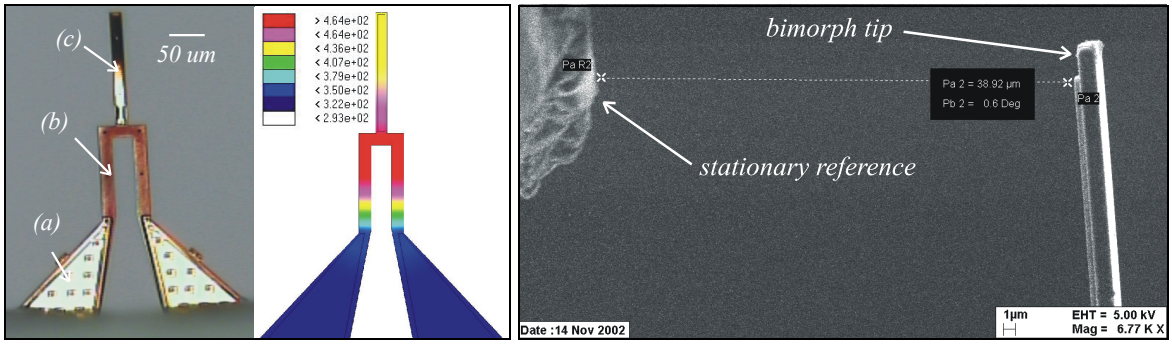

Figure 67: measurement device to capture plastic deformation

In the vacuum measurements, the contributions of convective cooling are negligible, so it is reasonable to assume that the temperature distribution along the bimorph is constant, so the stress and strain can be predicted using the tip deflection and the analytical techniques given in Finot et al.[126] A finite element model is used to predict the temperature based on the applied power and the data is then used to identify parameters in a creep model for gold.

The form of this model is

$$\dot{\varepsilon}_{cr} = C_1 \sigma^{C_2} \varepsilon_{cr}^{C_3} e^{-C_4/T}$$

where ε_{cr} is the creep strain, σ is the stress in MPa, T is the temperature in K, and the parameters $C_{1\text{-}4}$ control the shape of the function.[127] The creep model used in the FEA makes use of a reduced form of this equation that was found to represent the experimental data better (see reference [125] for details).

$$\dot{\varepsilon}_{cr} = C_1' \sigma^{C_2} \varepsilon_{cr}^{C_3} e^{-C_4/T}$$

The table of extracted values for these constants is shown below, along with a table of temperature dependant values for C_1'.

Table 9: Extracted creep parameters

Parameter	Value
C_1	2.6×10^{-3}
C_2	8.16×10^{-9}
C_3	1.946
C_4	7.46×10^{-45}

Table 10: Temperature dependant values for C1'

Temperature (K)	Parameter Value
386.69	2.69×10^{-14}
411.12	2.60×10^{-14}
447.60	9.84×10^{-14}
482.78	1.37×10^{-14}
535.03	6.14×10^{-16}
597.92	7.38×10^{-18}
640.52	1.04×10^{-17}

In general the plastic deformation mechanism is attributed to temperature, stress and strain dependent behaviour. The model used here incorporates temperature and strain hardening effects, and the correspondence between simulation and experiment indicates that this model captured significant portions of the plastic deformation mechanisms within the gold. The data is illustrated in Figure 68 below.

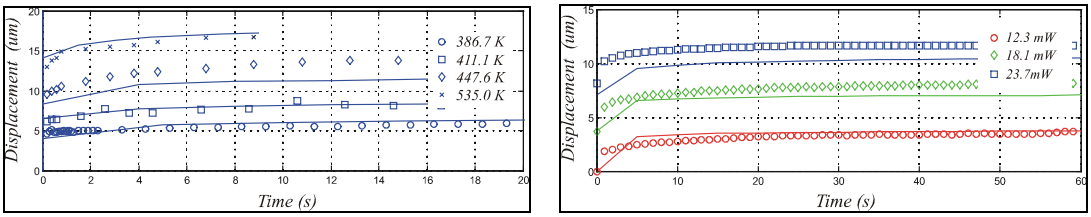

Figure 68: comparison of simulation and data for TPD process

3.4 TPDA Actuator geometries

The method discussed above was applied in the simulation and design of several TPDA actuators that make use of geometric patterns to achieve large displacements in a small footprint. The patterns all make use of alternating beams that are cascaded in order to sum the displacements of individual bimorphs and achieve linear and angular displacements that in some cases are larger than the actuators themselves.

The geometries can be categorized based on certain repeated design patterns. The entire class of TPDA actuators can be broadly divided into serpentine, helical, and S-Shaped geometries. Within

each of these categories, the bimorphs elements themselves can be curved or straight. The actuators can further be distinguished based on whether the bimorphs are cascaded in a symmetric or staggered pattern. Finally, in order to reduce the series resistance of the actuators for the purposes of minimizing losses in RF devices, the entire current path can be covered with gold and mechanically reinforced selectively, or it can consist of alternating segments that are not covered with gold. All these classifications are listed below in Figure 71, along with some SEM images of particular versions of the actuators.

Figure 71 a shows the initial as-fabricated position of the serpentine, symmetric, straight, half-metallized TPDA actuator. This design can rotate a payload about a central axis with a large angular displacement. In order to prevent parts of the device from interfering with the substrate, the device is removed from the substrate and bonded to a printed circuit board (PCB). The unit cell consists of a U-shaped arrangement of a bimorph and a single-material beam connected together at one end. This unit cell provides a small angular deflection, and can be connected mechanically and electrically in series with other cells to increase the overall deflection. Figure 69 below illustrates the procedure of cascading several unit cells into a device to amplify the angular deflection in the final device.

An image taken under an optical microscope of the packaged device is shown as well.

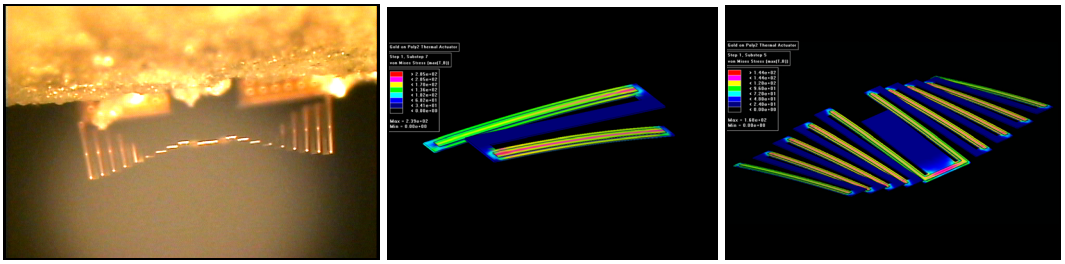

Figure 69: Packaged symmetric serpentine actuator (left), simulation of actuated unit cell (center) and simulation of entire device (right).

The previous geometry has the disadvantage that it requires a post-fabrication assembly and packaging step in order to prevent contact with the substrate. This issue is remedied by the staggered helical geometry shown in Figure 71 b. In this case, the lengths of the beams are varied so that they are always above the underlying substrate, and a large angle of rotation can be achieved following the deformation step. Figure 70 below shows FEA and an SEM image of this TPDA device, which can rotate over 90 degrees with a 9-volt input. The geometry of this actuator follows a helical path, and one turn of the helix consists of a poly2-gold bimorph, a via, and a straight beam of poly1 directly

underneath the bimorph. This turn is the unit cell of the device, and is cascaded serially several times in order to achieve an additive effect.

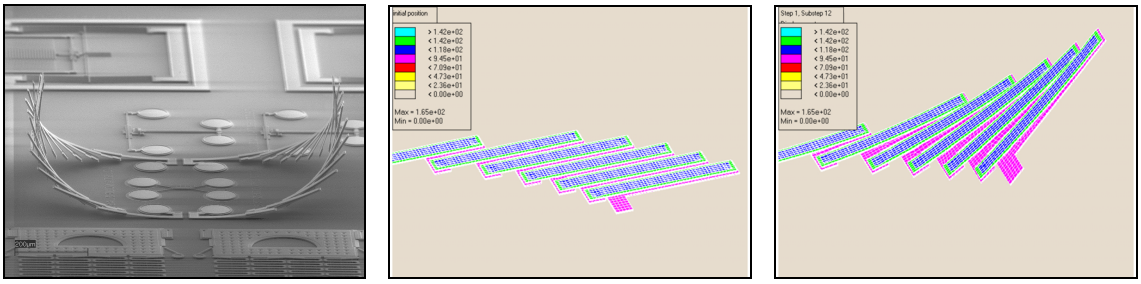

Figure 70: staggered helical TPDA design after deformation (left), simulation of initial position (center) and partially deformed position (right).

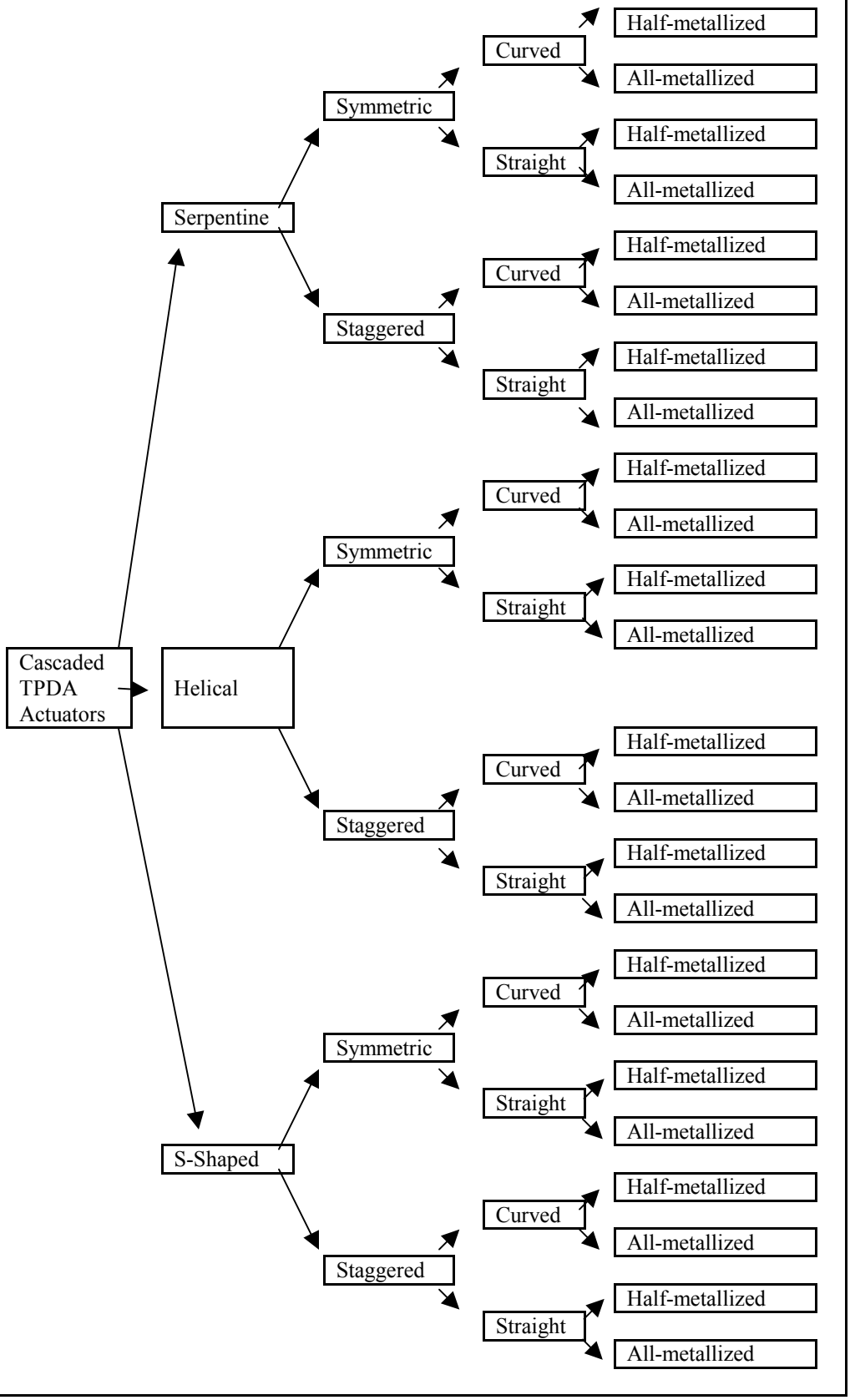

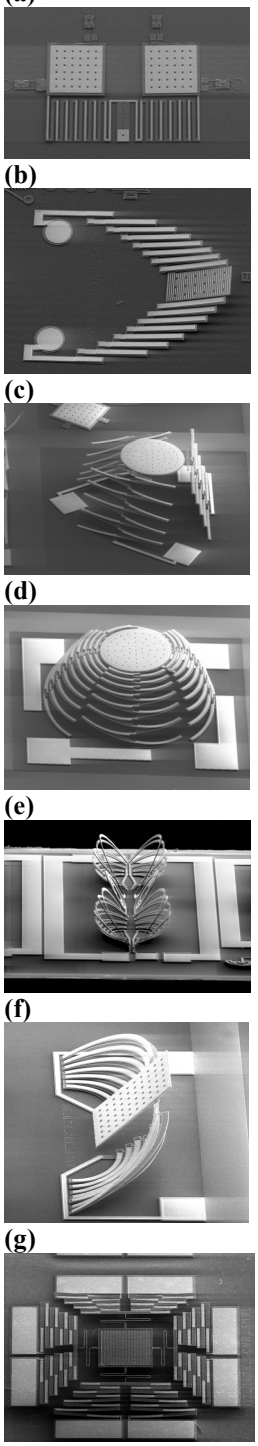

Figure 71: Geometric categorization of TPDA actuators

Both of the previously described geometries were designed to provide large rotation angles about a single axis. The device of Figure 71 c consists of three vertical actuators that are arranged isometrically to attain multiple degrees of freedom. The actuator itself is S-shaped and its tip deflects purely in the z-direction. A bimorph on the poly-2 layer is further extended by a straight beam in the poly 1 layer, connected together by the poly12via layer. This straight beam is then connected to an antiparallel bimorph segment of equal length. The two bimorph segments are oriented such that the resultant displacement at the tip of an S-shaped unit cell is completely in the z-direction. A single actuator can achieve over 250 um of displacement with 10 volts, and the isometric arrangement can achieve 90 degrees of rotation in any direction. Figure 72 below shows the device before and after HF release and plastic deformation. An orthogonal system of S-shaped actuators is shown as well, and consists of 4 actuators attached to a central plate.

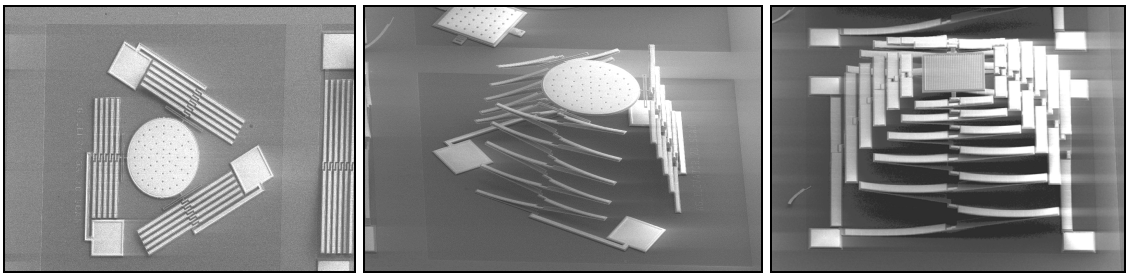

Figure 72: S-shaped geometry in isometric (3 actuators) and orthogonal (4 actuators) arrangements

The actuator depicted in Figure 71 d is also S-shaped, but it occupies a smaller footprint due to the curved geometry of the beams in its unit cell. The version shown above consists of four actuators placed orthogonally, and the version of shown below consists of three actuators placed isometrically.

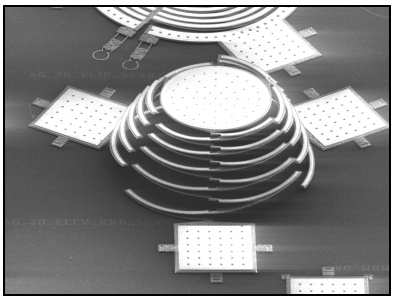

Figure 73: curved S-shaped actuators in isometric arrangement

In some cases, the series resistance of the actuator should be minimized in order to reduce parasitic losses that can occur at high frequencies. In order to accomplish this, the entire actuator must be covered with gold and selectively reinforced. The device depicted in Figure 71 e is an RF coupler with a curved serpentine geometry. Segments of the actuator that are intended to deflect consist of Poly2 and gold bimorphs. The segments that are intended to remain straight include a poly1 beam with the same footprint as the poly2 and gold above, resulting in a cross section that is thicker, as shown below in Figure 75. Figure 74 is a screen capture of the deformed mesh as it was simulated using ANSYS.

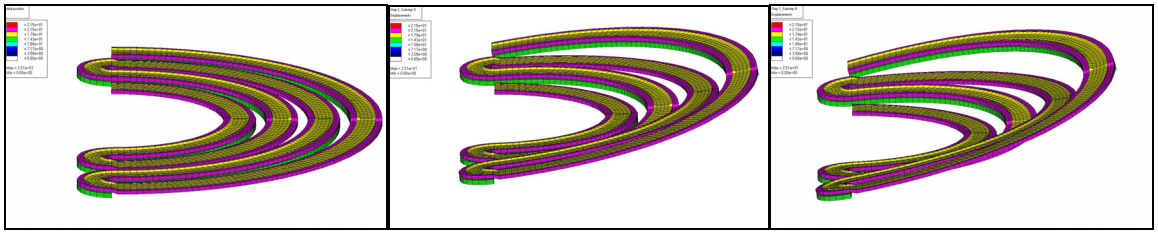

Figure 74: deformed mesh after FEA of curved serpentine actuator with full metallization

The actuators in Figure 71 e and f have the advantage that they rotate about a fixed axis, which is desirable for 1-D optical beam scanning applications discussed later, since the illumination axis is fixed. The staggered geometries rotate and translate simultaneously when they are actuated.

Figure 75: partially deformed actuator (left) and detailed view of reinforced segment (right)

Figure 76 below is a detailed view of the helical and S-shaped geometries that are based on curved beams.

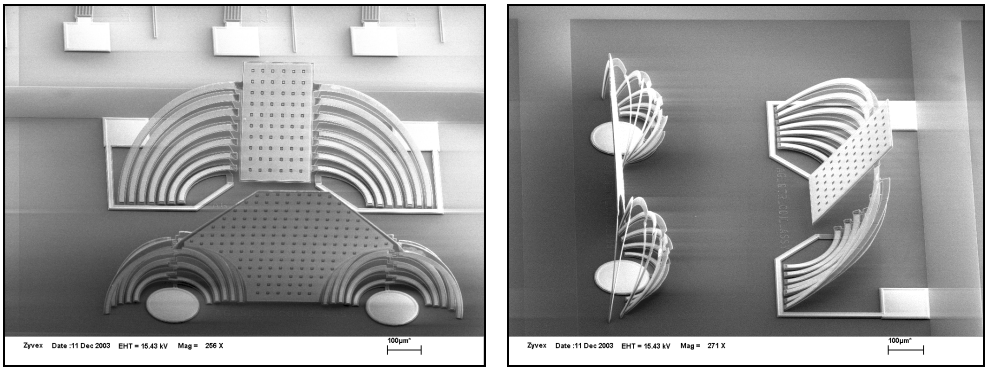

Figure 76: detailed view of helical and s-shaped geometries based on curved beams

The serpentine geometry shown in Figure 71 g was designed to provide linear translation in the z-direction. The particular device shows 4 z-actuators that are coupled orthogonally to a central payload. The actuator itself consists of bimorphs interconnected by passive beams, very similar to the S-shaped geometry of Figure 71 c. SEM images of just the actuator taken from two perspectives illustrate the linear deflection that is produced.

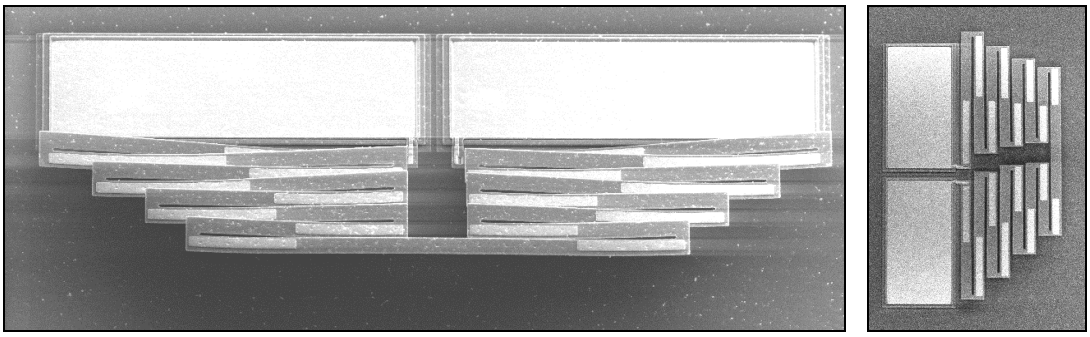

Figure 77: serpentine geometry provides linear translation in z-direction

A large number of geometries based on the TPDA method have been successfully implemented to achieve different assembled shapes and actuation directions using several cascading techniques. Different arrangements of beams can result in rotational or translational motion, depending on the method in which they are interconnected by passive members. Curved beams and straight beams have both been used in S-shaped, helical, and serpentine cascaded structures that provide large static and dynamic rotational or translational displacements. This chapter focused on the design methodology and the various geometries that have been implemented. Detailed

characterization of the actuation amplitudes and frequencies were measured using optical techniques, and are discussed in the following chapters.

Chapter 4
RF MEMS

One of the most expensive and labor intensive post-fabrication steps in the manufacturing process of any RF circuit is tuning. Tolerances associated with current fabrication techniques for RF circuits have necessitated the incorporation of tunable elements in order to compensate for differences between the designed and fabricated devices. The incorporation of tunable MEMS components that can be deformed to assume desired values could reduce the costs associated with this step. TPDA actuators can be *permanently* tuned during an in-circuit calibration step, without requiring the labor-intensive processes and bulky form factors that are associated with tuning screws. Since the deformation process can be controlled with an applied voltage, the tuning process can be carried out in conjunction with the RF characterization process, by applying a DC bias along with the RF signal. Furthermore, the devices can be actuated back to their initial position following deformation, providing some *variable* or active tuning during the operation of the circuit.

Four RF devices that are based on the methods of actuation developed in the previous chapter are discussed here. The first device is a 2-port RF coupler based on a curved, semi-circular, serpentine TPDA actuator. The second device makes use of a large conductive plate that can be actuated in the z-direction over a range of 300um. This plate and its actuators are removed entirely from the MEMS substrate and bonded to a separate substrate with the RF circuit to be tuned. Also, an interdigitated variable capacitor based on an in-plane actuator with a mechanical latching device is presented along with simulation and measurements. A single-turn tunable inductor based on the TPDA process is presented as well.

All the data that is presented here was obtained using the Agilent 8722 ES vector network analyzer (VNA) calibrated in the frequency range of interest.

4.1 TPDA Variable Coupler

The device shown below in Figure 78 consists of a symmetrical arrangement of 2 electrically separated TPDA actuators. The initial position and self-assembled positions are separated by approximately 60 degrees in this figure, and 90 degrees of plastic deformation has been achieved by further deforming the device with voltage pulses. Each port in the 2-port device is connected to one of the actuators, and the entire current path is covered with a 0.5 um layer of gold to reduce the series resistance. This is an example of a fully metallized TPDA structure, in which certain segments are selectively reinforced with the addition of the poly-1 layer. Adjusting the proximity of the lines to one another by rotating the actuators varies the coupling between the lines. A bias-T was used to apply the current required for joule heating, and a CPW interface is included for measurement purposes.

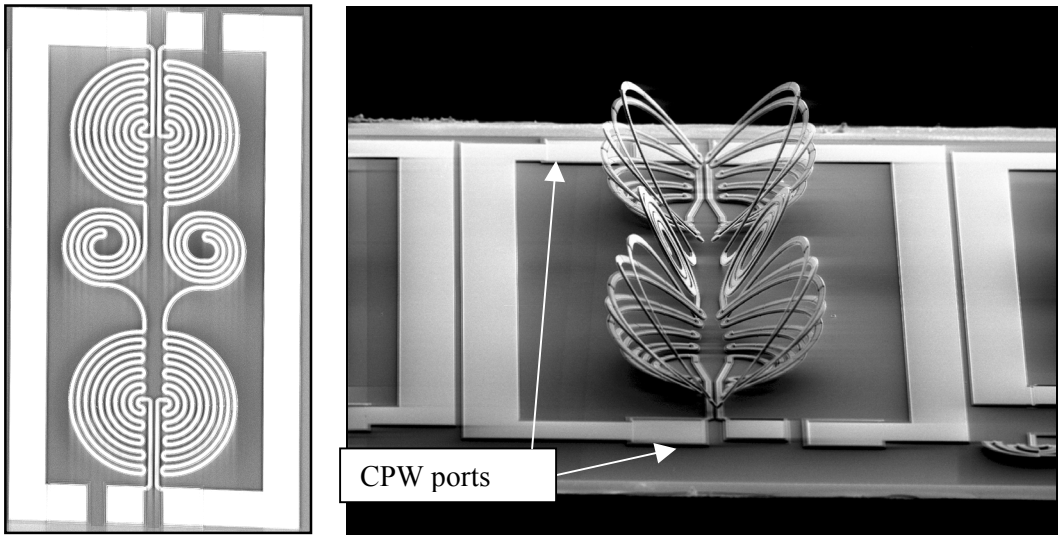

Figure 78: TPDA coupler in initial position (left) and deformed position (right)

The MUMPs process uses a high conductivity silicon substrate and a very thin metallization layer, resulting in lossy measurements. However, the tunability of the circuit is demonstrated in the S12 curve, showing a 25 dB variation in coupling between the ports at 19 GHz with 0-10 volts of applied potential.

Each half of the TPDA structure behaves as a variable inductor, mostly due to the self-inductance of the conductor. The mutual inductance is assumed to be negligible, since the direction of the current in any pair of adjacent lines is opposite. As the inductor is assembled away from the

substrate, the substrate losses are reduced and the inductance increases, as well as the self-resonant frequency. This is illustrated below in Figure 79.

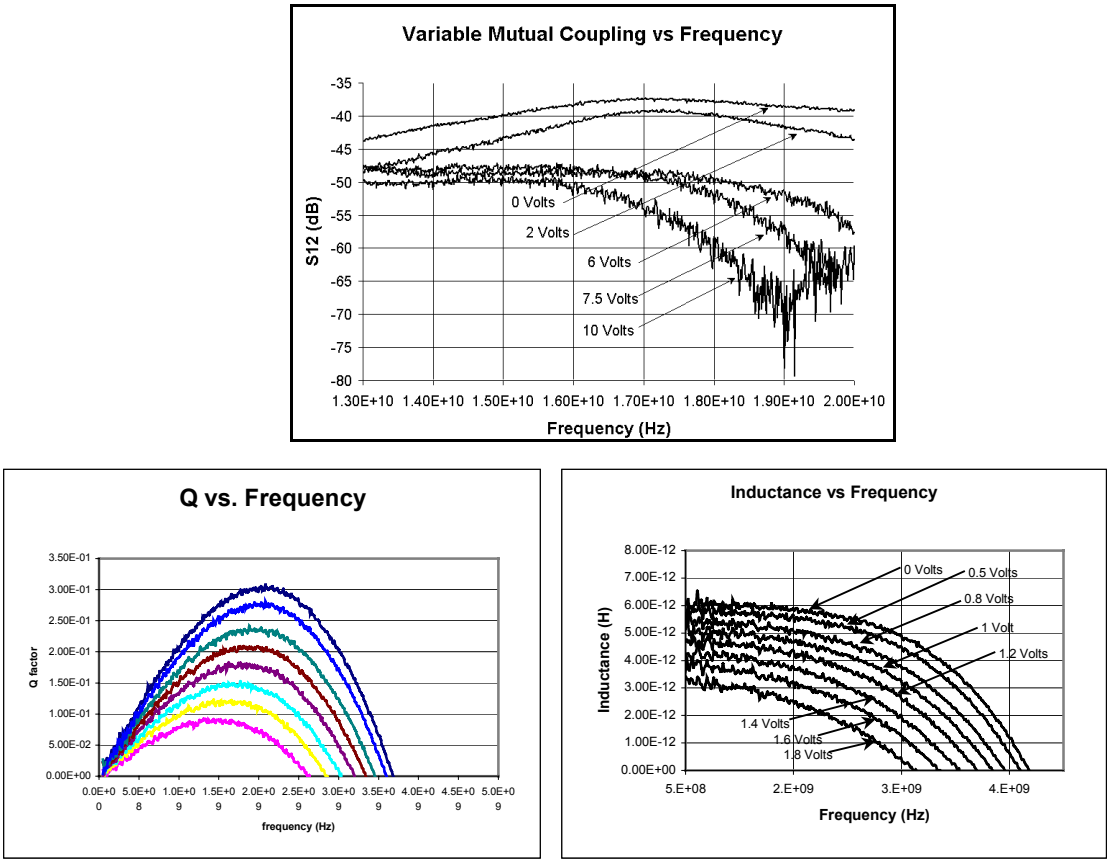

Figure 79: top, coupling between the electrically isolated ports as a function of actuation voltage; left, Q of a single inductive branch of the coupler as a function of actuation voltage; right, inductance of a branch of the coupler.

4.2 TPDA Variable Capacitor

The lossy nature of the MUMPs process is mainly due to the thin metallization layer of gold that is laminated onto a lower conductivity polysilicon layer, overlying a high conductivity silicon substrate. This restricts the performance of capacitive devices with respect to their Q. The alternative approach suggested here consists of an interdigitated capacitive structure fabricated on a lower loss alumina substrate. A metallized plate fabricated in the MUMPs process is then bonded to the RF circuit, and actuated with S-shaped vertical TPDA actuators that have a large z-deflection capability. A metallized plate that was designed for this application is shown below, anchored to the MUMPs chip. The version of the actuator that is intended for use with the capacitive circuit is fully released from the substrate, and has not yet been released.

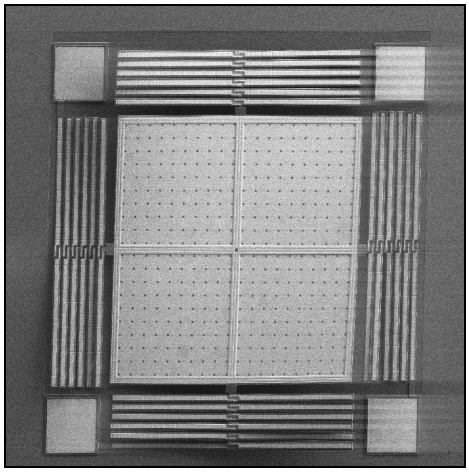

Figure 80: metallic plate with large range TPDA vertical actuator

The proposed device has been simulated in Sonnet using the interdigital layout depicted in Figure 81, consisting of 40 um lines and spaces and a CPW interface. The MUMPs device is simulated as a flat plate of gold that is 0.5um thick and parallel to the alumina substrate, and its proximity to the circuit is adjusted with a DC voltage used for actuation. The simulations indicate that a large tuning range can be expected, which is reasonable since the plate has a far greater motion range than any electrostatic parallel plate device. Another significant advantage of this configuration is the power-off tuning capability that can be achieved using TPDA.

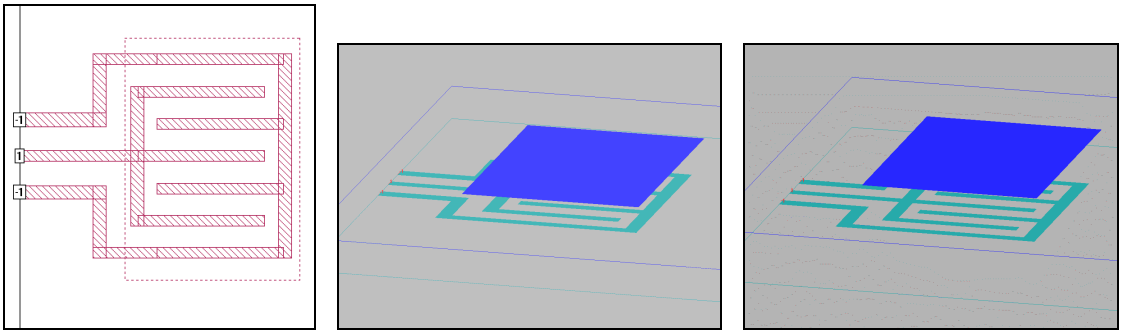

Figure 81: Sonnet screen captures of layout of interdigital structure (left) and 3-D simulation of metallic plate in proximity to substrate.

A plot showing the self-resonant frequency of the capacitor as a function of plate spacing is shown below in Figure 82, along with a plot of capacitance vs frequency with various gap sizes. As the gap is decreases, the self resonant frequency decreases and the capacitance increases, which is to be expected since the geometry resembles a parallel plate capacitor, where $C = \frac{\varepsilon_0 A}{d}$.

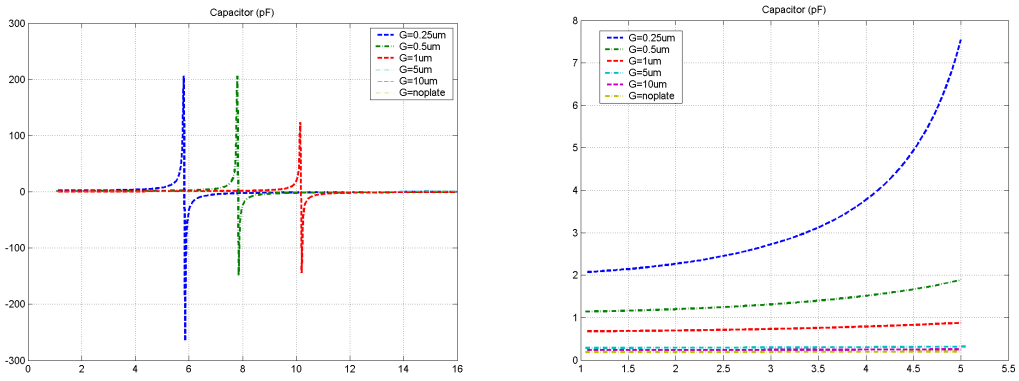

Figure 82: Capacitance (pF) as a function of frequency (GHz) with various gaps between circuit and capacitive plate

4.3 Mechanically Latched Variable Capacitor

The devices that have been presented in this chapter have been designed to reduce the effects of the losses that are inherent to the MUMPs process. In the case of the coupler, the entire circuit path was covered with gold in order to minimize the series resistance and avoid placing any polysilicon in series. In the case of the capacitor presented above, the RF circuit is placed on an alumina substrate, and the MUMPs device is to be assembled to it using flip-chip bonding. In the device presented below, the circuit path is again covered with a thin layer (0.5 um) of gold; however in this case, the actuators are not part of the circuit, so no selective reinforcement is required. Amplified bent beam actuators are used in this design instead of TPDA actuators. Also, a latching mechanism is used in order to eliminate any quiescent power consumption while the device is not being tuned. The overall layout of the device and a detailed view of the latching mechanism adopted from Geisberger[128] are shown below in Figure 83.

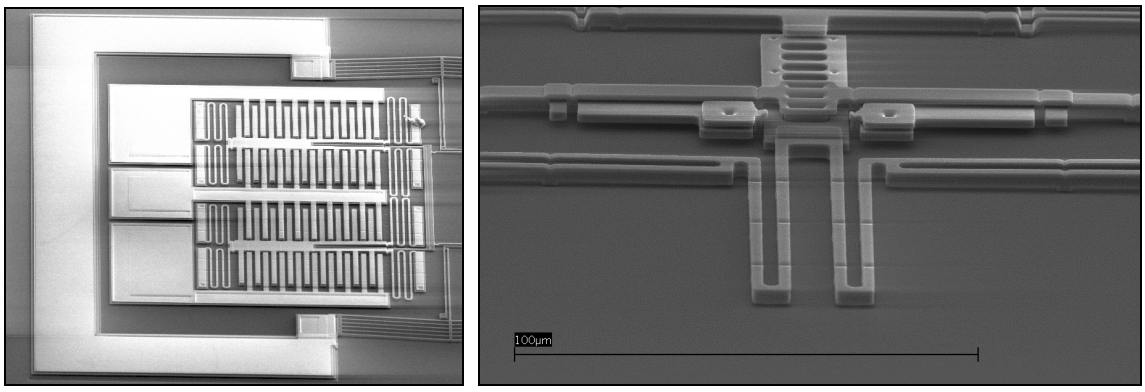

Figure 83: Laterally actuated interdigital capacitor (left) and latching mechanism (right)

The device geometry shown above is a repeated structure that consists of a unit cell with the following geometry (Figure 84). This cell is reflected symmetrically about the signal line in the CPW interface, and so one half is shown here. The capacitance between the signal and ground lines is adjusted by means of a floating conductor that acts as an intermediate parallel plate as shown in Figure 80.

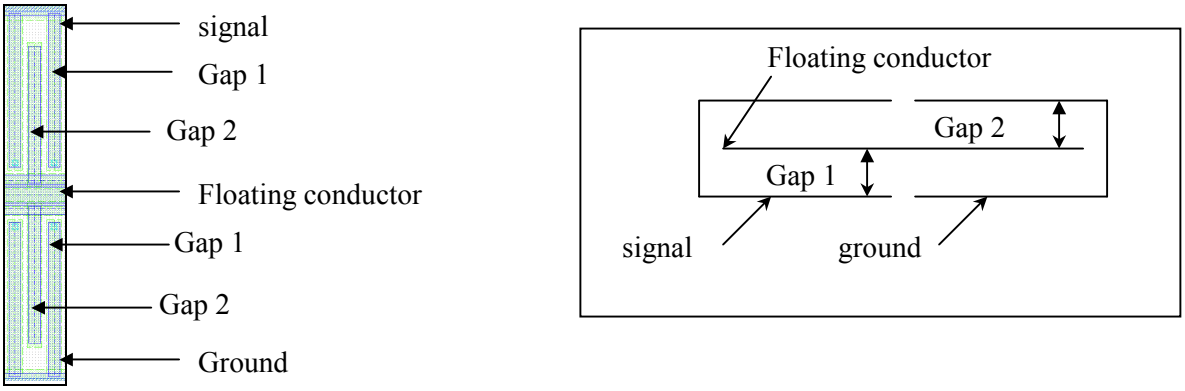

Figure 84: layout screen capture of device (left) and pictorial depiction of geometry (right)

The floating shuttle is initially located symmetrically between two sets of ground and signal conductors. As the shuttle is translated towards one pair and away from the other, the net capacitance seen at the CPW port increases. Neglecting the fringe field contributions, the following expressions are used to determine the general behaviour of the capacitance as a function of gap spacing and frequency. We first model the symmetric arrangement of plates shown in Figure 84 with 4 capacitances in the following arrangement (Figure 85)

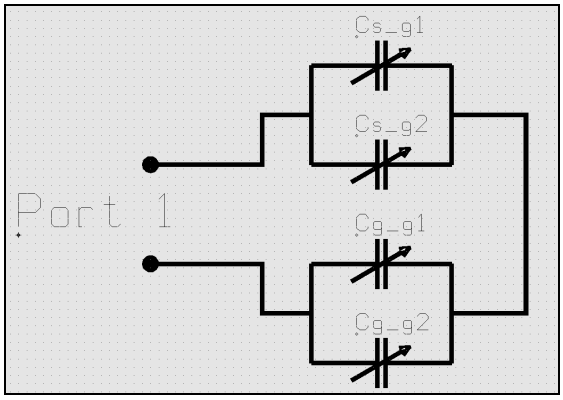

Figure 85: schematic diagram of capacitances

In this arrangement, $C_s g_1$ represents the capacitance between the signal line and the shuttle over the gap g_1, $C_s g_2$ represents the capacitance between the signal line and the shuttle over the gap g_2, $C_g g_1$ represents the capacitance between the ground line and the shuttle over the gap g_1, and

$C_g g_2$ represents the capacitance between the ground line and the shuttle over the gap g_2. The CPW version that was implemented includes 2 circuits identical to this one that are reflected about the signal line. The analysis is simplified here by virtue of symmetry about the central axis of the CPW port, and is further simplified because we consider one unit cell of the capacitor, which is repeated 18 times in the design.

To illustrate the tuning behaviour of the device, the expression for total capacitance as a function of the gap is investigated. The gap can be varied by translating the shuttle over a 3 micron lateral distance. The expressions for calculating the gap dimensions are simply:

$$g_1 = 3 - x_a$$

$$g_2 = 3 + x_a$$

and of course,

$$g_1 + g_2 = 6$$

where g_1 and g_2 are the gaps and x_a is the actuation displacement. All quantities are in microns, and the 27 micron motion of the actuator is scaled down to the 3 um range of the shuttle by motion reduction springs. This is particularly advantageous as it allows the latching mechanism to operate over the entire range of the actuators with 6 um increments, and the locked positions are scaled down to the fit within the 3um range of the shuttle.

The capacitances $C_s g_1$, $C_s g_2$, $C_g g_1$ and $C_g g_2$ are calculated using the basic expression for a parallel plate capacitor, neglecting the fringing fields.

$$C_s g_1 = \frac{\varepsilon_0 A}{g_1}$$

$$C_s g_2 = \frac{\varepsilon_0 A}{g_2}$$

$$C_g g_1 = \frac{\varepsilon_0 A}{g_1}$$

$$C_g g_2 = \frac{\varepsilon_0 A}{g_2}$$

In these expressions, A is the area of the lateral cross-section of the beams, 100um x 4 um. The total capacitance is taken as the parallel combination of $C_s g_1$ and $C_s g_2$ added in series with the

parallel combination of $C_g g_1$ and $C_g g_2$ as shown in the schematic:

$$C_{total} = \left(C_s g_1 \| C_s g_2\right) + \left(C_g g_1 \| C_g g_2\right).$$

This expression can be simplified,

$$C_{total} = \frac{1}{2}\left[\frac{\varepsilon_0 A(g_1 + g_2)}{g_1 g_2}\right].$$

The capacitance can be expressed in terms of the actuation displacement:

$$C_{total} = \frac{1}{2}\varepsilon_0 A\left[\frac{(3 - x_a) + (3 + x_a)}{(3 - x_a)(3 + x_a)}\right]$$

$$C_{total} = \frac{1}{2}\varepsilon_0 A\left[\frac{6}{9 - x_a^{\,2}}\right]$$

A graph of the capacitance as a function of actuator displacement is shown below. Note that the actuator displacement has a range of 30 microns in this graph; this motion is scaled down to the 3 um range of the shuttle by a motion reduction spring.

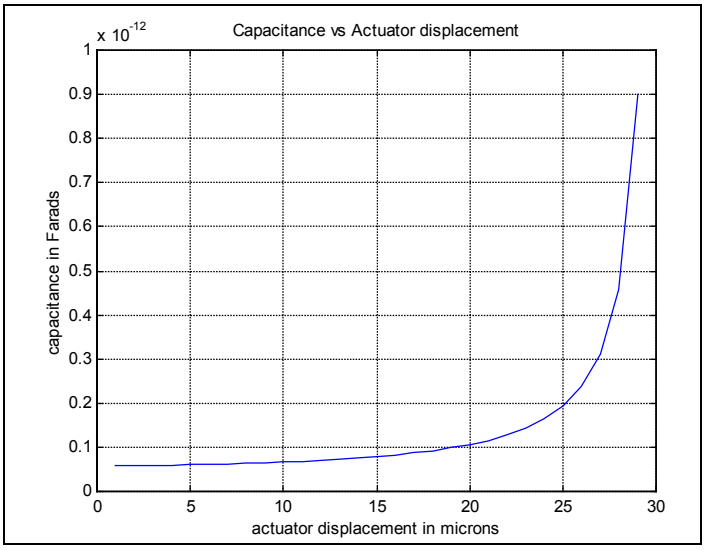

Figure 86: analytically calculated capacitance as a function of actuator displacement

The data that was obtained for this MUMPs device is presented below. S11 is plotted on the Smith chart for the frequency range of 1 GHz to 15 GHz, and the curve's proximity to the unity circle is indicative of low losses, as indicated by the Q-factor plot below. The capacitance value predicted by the model (~1pF) is also in proximity to the measured value (~1.5 pF).

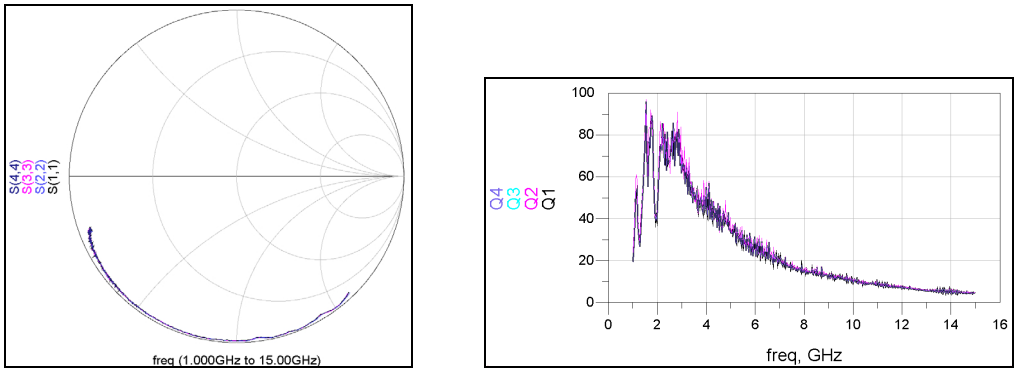

Figure 87: Measured Smith Chart and Q values for interdigitated geometry

The simple electrostatic analysis of the capacitance variation presented above assumes a parallel plate configuration. In fact, the fringe fields in the prototype presented here are dominant for several reasons. First of all, the metallization layer is restricted to a 0.5 um thin film at the top of the beams that must be inset from the poly edge by 2 um due to design rules related to the liftoff process. Also, the aspect ratio of the signal, ground and shuttle beams is approximately 1:1. Finally, the sidewall roughness of the stacked geometry makes is difficult to obtain large flat surfaces in close proximity to one another.

Two processes are excellent candidates to implement this structure and obtain parallel plate behaviour. The Metal MUMPs process contains a high aspect-ratio nickel layer that is 20 um thick, and a bulk etch is used to reduce the effect of substrate losses. An even better candidate is the SU8 molding and copper electroplating process that was used to create the structures shown in Figure 88 below, which are 140 um tall. Both of these processes should yield a capacitor with large tuning ranges as predicted by the model. Since the materials used are less lossy than the silicon of the MUMPs process, it is reasonable to assume that the Q's will remain high. The increased area of overlap that is provided by the thicker beams (35 times thicker) will also increase the capacitance value.

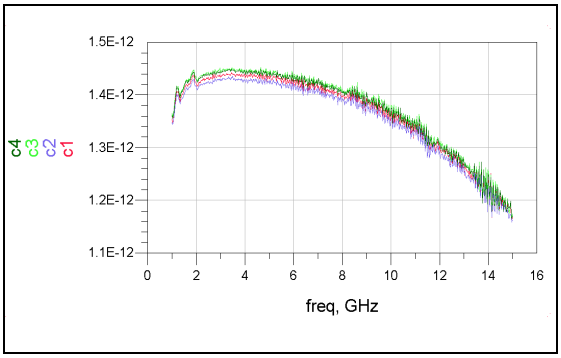

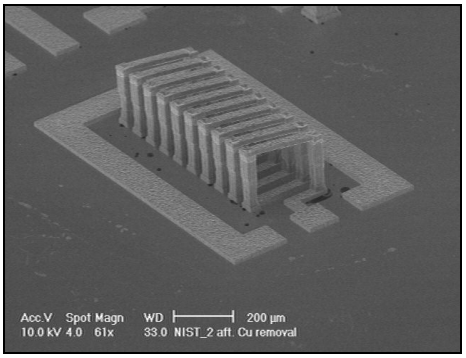

Figure 88: measured capacitance of interdigitated structure (left) and 3-layer copper electroplating process used to fabricate inductors (right).

4.4 Variable inductor

Rapid increases in the levels of integration in modern mobile communication equipment along with decreases in fabrication costs of the front-end of microwave transceivers will necessitate high-Q (quality factor) inductors with self-resonant frequencies (SRF) in excess of 10 GHz. Unfortunately, inductor coils that are in proximity to conductive substrates suffer from excessive losses at frequencies above 1GHz, and the parasitic capacitance between the conductor and the substrate limits the self-resonant frequency that can be achieved. Furthermore, continuous inductance variation is desirable for fine tuning the frequency of resonant circuits or for accurately matching impedances.[129]

Several approaches have been pursued to minimize parasitic effects and achieve moderate tuning ranges. Bulk micromachining techniques such as anisotropic KOH etching have been used to remove the substrate directly underneath inductors, increasing the Q and the SRF.[130,131] Self-assembly of inductors to a position orthogonal to the substrate has been demonstrated using PDMA (plastic deformation magnetic assembly),[132] SDAs (scratch drive actuators),[133] solder self-assembly,[134] and stress mismatches between thin films deposited in surface micromachining processes.[129] MEMS solenoid inductors fabricated using thick photoresist lithography have been demonstrated as well.[135] The inductors depicted below in Figure 89 make use of TPDA structures to tune their position with respect to the substrate. The device on the left was adopted from Lubecke[129] to incorporate a CPW interface and has similar performance, with the added feature of power-off tunability using TPDA. The device on the right has also been characterized, and measurement data is included in figure 91 The low Q resulting from the substrate and conductor losses is apparent in the data. However, the increase in Q as a result of separation from the substrate is clearly visible in the smith chart, and a variation in inductance occurs as well, validating this approach. Similar structures can be fabricated with a bi-metal process and placed on an alumina substrate to improve RF performance while maintaining the tuning characteristics and power-off tunability of TPDA devices.

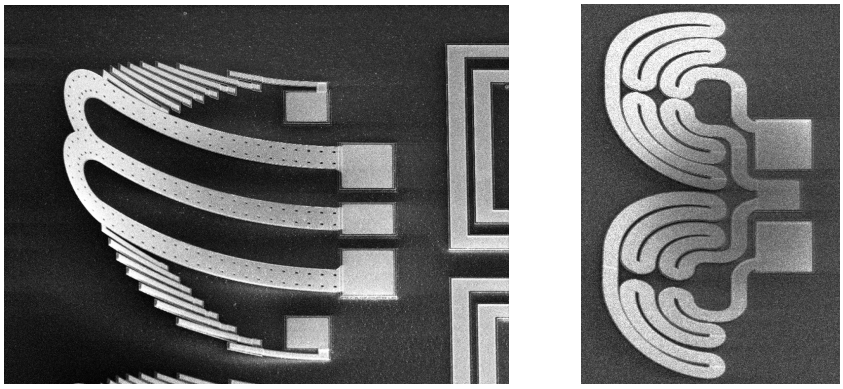

Figure 89: SEM Of inductive geometries

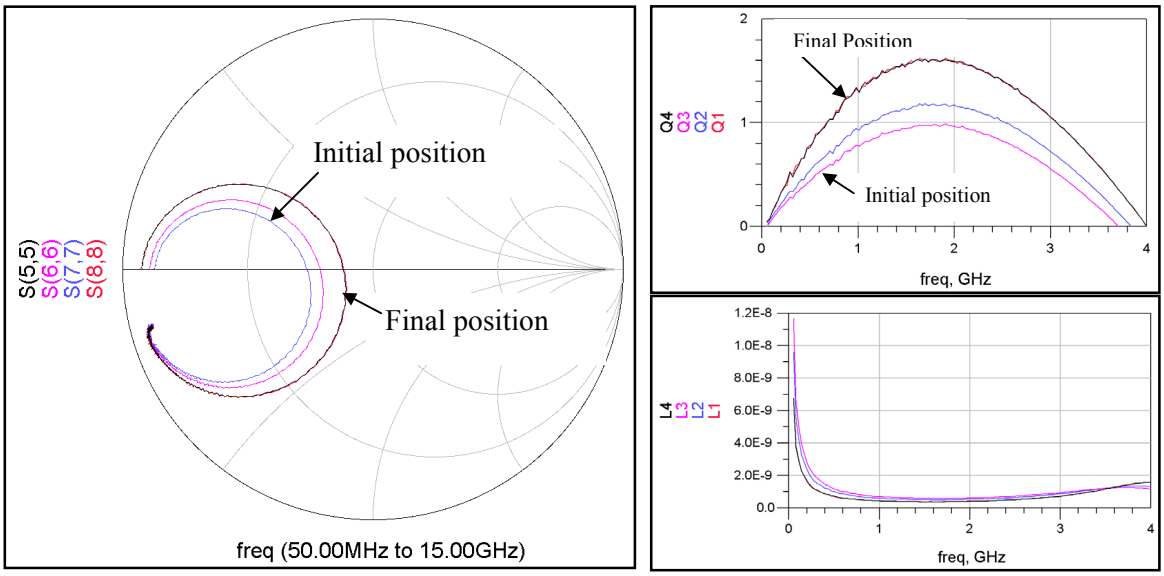

Figure 90: Smith chart, Q and inductance of TPDA structure with various actuation voltages

Some further observations that were deduced from Sonnet simulations by Lubecke et al[129] were confirmed with this geometry as well. These parametric simulations indicate that ohmic losses dominate at low frequencies (2GHz), which is expected due to the skin depth at these frequencies and the thin (0.5 um) metallization layer. Losses due to the parallel resistance of the of the structural polysilicon layer come into play in the middle frequencies, and above that, the parasitic capacitance associated with the substrate ultimately dominates. A thicker metal layer also improves the low

frequency Q, but the benefits are less significant beyond a thickness of about two skin depths (3um at 2 GHz). Reducing the local substrate conductivity would further increase the Q as well.

Chapter 5
OPTICAL MEMS

The burgeoning area of optical MEMS, often referred to as Micro Optical Electro Mechanical Systems (MOEMS), has been the central focus of several well-established conferences, large research initiatives, and textbooks.[136] Its applications include micromirror and micro grating display devices, adaptive optics, beam scanning and steering, imaging and spectroscopy systems, optical switches, variable optical attenuators, passive fiber alignment structures, tunable filters, lasers and detectors.
The research presented in this chapter involves optical applications for the actuation and self-assembly methods discussed above. More specifically, micromirrors based on TPDA structures have been developed for wide-angle beam steering applications. *Variable* periodic structures such as 1-D arrays of reflective beams (gratings) and 2-D arrays of reflectors (treated as optical phased arrays) have been designed as well. The parameters that are varied are the spacing of the reflectors (the period) and the phase of the array elements (reflectors) with respect to the impinging field.
The original motivation for the development of TPDA structures was to provide large angle motion for micromirror devices. A micromirror with 90 degrees of mechanical motion is useful for 1-D scanning and imaging applications such as bar code scanning, profilometry, or 1xN optical switching. This capability in two axes (θ,ϕ) can steer a beam to any point within a hemisphere, which is useful for displays, imaging systems, laser tracking systems and telecommunications, among other applications. Although some designs have been reported to produce such large deflections, they either must be actuated in resonance, or they require complex systems of hinges and sliding contacts that are inherently unreliable. A flexure-based design that is capable of producing *static* displacements of this magnitude at low operating voltages has been implemented with TPDA geometries.
Variable period gratings that are actuated with flexure-amplified bent beams and SDA's (scratch drive actuators) are presented as well. Each period of the grating consists of a reflective beam and a pair of springs that connects it to the adjacent period. The spring network can be designed to provide an arbitrary spacing between the elements that is conserved upon actuation (chirped, constant space, fresnel, etc.)

Optical phased arrays have also been implemented using TPDA actuation. If a periodic structure is placed near the waist of a Gaussian beam, the incident field can be approximated as a plane wave. If the Raleigh range of the beam is much larger than the dimensions of the array, a linear phase distribution can be assumed across the elements when the array is tilted. These assumptions are made in order to model actuated 1-D and 2-D arrays using antenna array methods.

5.1 Large angle single-axis Scanning Mirrors

Micromirrors that can provide large beam steering angles with low input voltages are attractive for many applications. When actuated at resonance, a high frequency scan can be used in profilometry, bar code scanning, or proximity sensing by sweeping a collimated laser beam over an arbitrary surface. A mirror that can maintain a fixed angular deflection corresponding to an analog input voltage can be used in optical switch systems, free-space optical data links on mobile platforms, and motion tracking systems. The TPDA mirrors have mechanical resonant frequencies of several kilohertz and static deflection capabilities of up to 90 degrees.

Several geometries that have been fabricated using TPDA were tested in beam steering experiments to characterize the static and dynamic actuation properties, reliability, power consumption, and stability of the mirrors. The staggered serpentine geometry in Figure 91 achieves 90 degrees of mechanical deflection, which can steer a beam over 180 degrees. This geometry is not optimal since the mirror translates as it rotates in order to prevent contact with the substrate. The symmetric and semi-circular geometries discussed earlier can produce rotation about a fixed axis, so a stationary collimated beam can be deflected to a desired position.

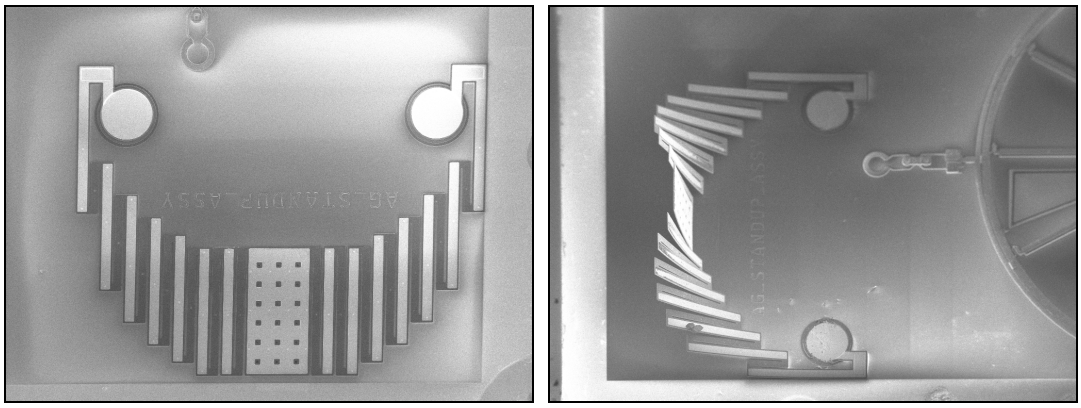

Figure 91: 1-D scanning mirror in initial (left) and self assembled (right) position

A HeNe laser was used in the simple layout depicted in figure 94. A neutral density filter is used to reduce the intensity of the beam and thus reduce the effective spot size at the beam waist. A slow lens focuses the beam down to a 80 um spot at the mirror, where it is reflected onto a cylindrical screen. At the observation point, a ccd is used to record the position of the beam on the screen.

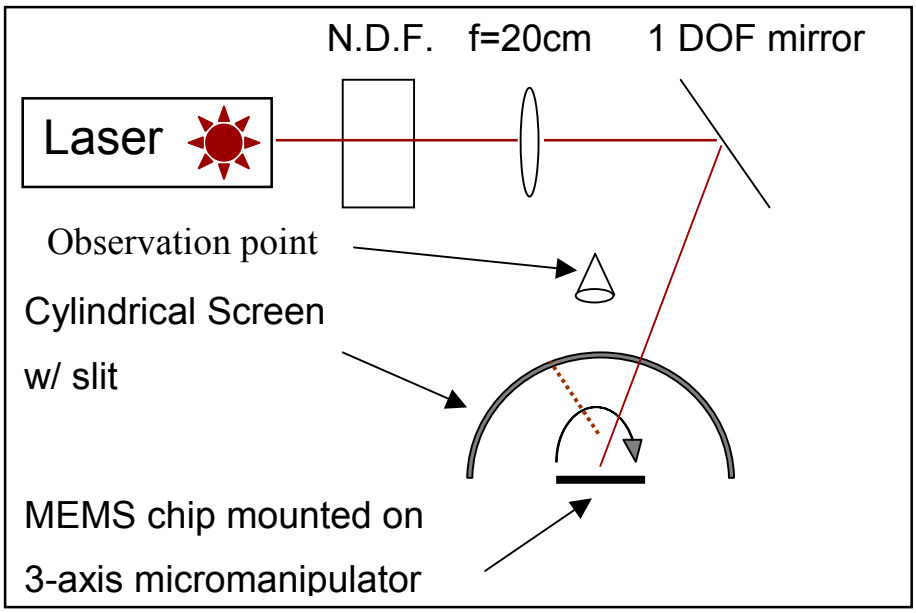

Figure 92: Characterization setup

Figure 93 is a typical image of a scanned beam on the cylindrical screen. The brightest point at the right in the image is the reflection from the substrate, corresponding to 0 degrees when the mirror is flat. The static deflection and frequency sweep data is included in figure 95 for the staggered serpentine geometry.

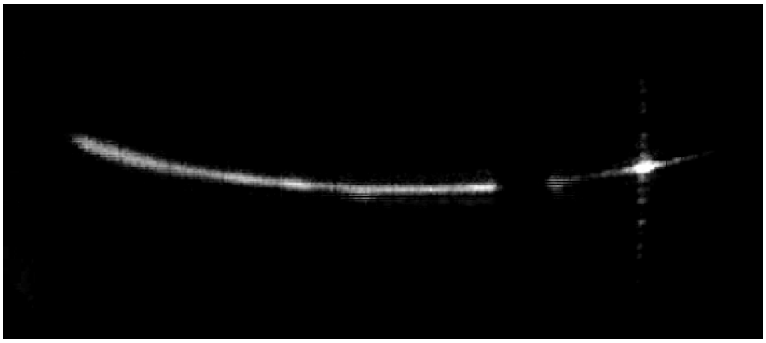

Figure 93: captured image of beam scanned across cylindrical screen

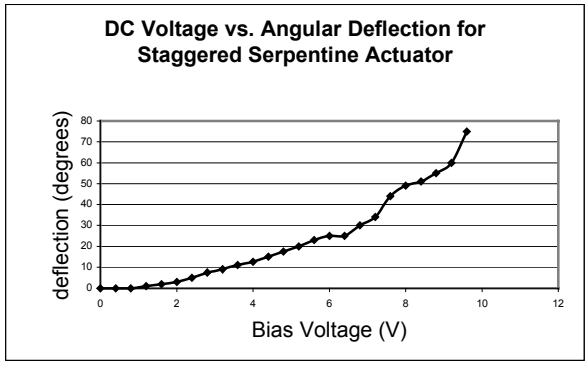

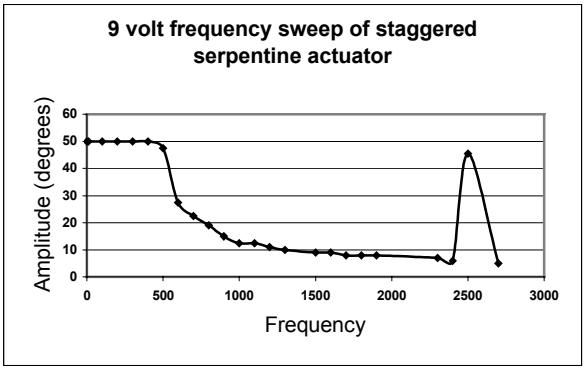

Figure 94: Static and dynamic characterization of staggered serpentine actuator

A static deflection of 75 degrees is obtained at 9.5 volts, and the onset of plastic deformation occurs at 12 volts. The first mechanical resonance occurs at 2.5 kHz, and operation at resonance is shown in figure 95 above. It is important to note that there are several design tradeoffs that can be considered in order to obtain a desired deflection magnitude or resonant frequency. The actuators in Figure 95 can be designed to provide 90 degrees of static mechanical deflection at lower voltages, but their mechanical resonances occur at 1.6 – 1.8 KHz. Increasing the number or cascaded unit cells will result in a more compliant structure with a lower resonant frequency, a higher operating voltage due to the increased series resistance, and of course a larger static displacement capability. Decreasing the number of beams results in the opposite changes. The series resistance of the 1-D TPDA structures presented so far ranges from 1 to 5 kilo-ohms, which corresponds to a steady state power consumption of 20 -100 mW at the fully actuated position.

Figure 95: scanning micromirrors with s-shaped and helical geometries

5.2 2-D scanning mirrors for displays and imaging systems

The first MEMS-based scanning displays were based on two separate 1-D scanners arranged orthogonally to obtain a raster-scan pattern. Typically, one of the mirrors would operate at resonance and the other would be actuated at the refresh rate of the display. This approach has been replaced by gimbal mechanisms that are used in commercially available electrostatic scanning mirrors. Unfortunately the actuation angles are severely limited and the operating voltages are quite high (30 – 200 V). These and other types of MEMS displays are discussed in the literature review section.
The approach used here makes use of TPDA actuators that produce large (>100 um) displacements in the z-direction, with no translation in x or y. These z-actuators can be placed isometrically or orthogonally about a mirror surface as shown in Figure 96 and used to achieve 90 degrees of mechanical rotation in 2 axes with less than 10V. In designs with lower actuation angles such as the orthogonal scanner in Figure 96 the resonant frequency increases to 4.2 kHz and the scan angle decreases to 15 degrees. The mirror surface does not translate as it rotates for any of these mirrors, so the incoming collimated beam remains centered on the reflective surface. The actuators were powered using three sinusoidal waveforms with arbitrary frequency and phase in order to obtain lissajou patterns projected onto a planar surface. These patterns were captured using a digital camera with a timed exposure of 33ms. The images demonstrate that a full motion raster-scanned video display can be implemented with one axis in resonance and the other axis at the refresh rate.

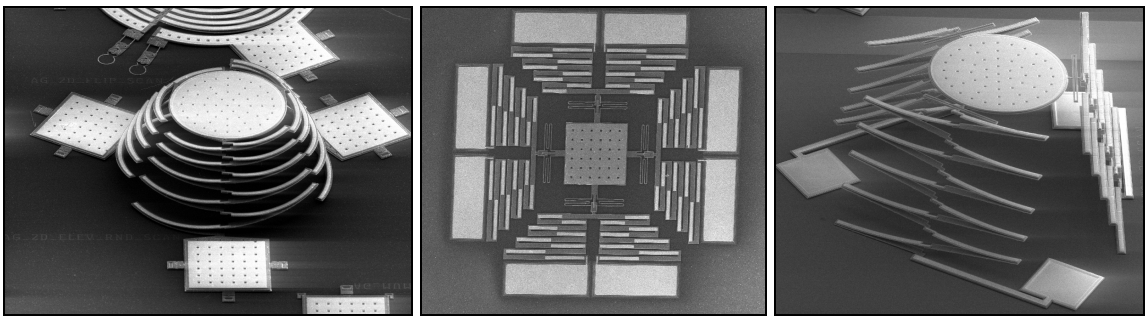

Figure 96: Isometric and orthogonal 2-D scanning micromirror devices

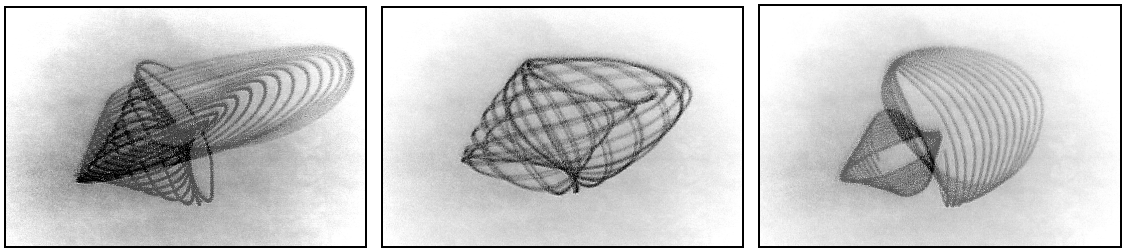

Figure 97: frames with 33 ms duration captured using a CCD – laser reflected of the micromirrors was projected onto a flat screen.

In order to accurately measure the voltage vs. deflection characteristics of the mirror and to determine their stability over time, an autocollimator as shown in Appendix A will be used. Although the shape of the curves is similar to the 1-D mirror curves shown above, this instrument has a higher resolution (<0.05 degrees) and can provide insight into the coupling between the axes.

5.3 Variable period grating

The remainder of the optical devices discussed in this chapter are periodic structures that are geometrically modified using MEMS actuation. Optical phased array methods were chosen for the analysis of these structures, and have shown excellent agreement with measured results.

In the case of the variable period grating, the surface of the grating is at a fixed angle with respect to the incoming beam, and so a simple grating formula is used to explain the effects of varying the spacing of the grating elements.

The well-known expression for the location of the maxima in the far field pattern of a grating is

$$d \sin\theta = m\lambda$$

where d is the distance between the grating elements, θ is the angle that the maximum makes with the normal to the grating surface, m is the order of the maximum, and λ is the wavelength of the illuminating source. Under the far-field approximation, the position of the order when projected onto an x-y plane is

$$y \approx \frac{m\lambda D}{d}$$

where D is the distance between the observation point and the grating. Thus, the spacing of the grating elements is related to the location of the maxima. A grating can be rotated in order to position the maximum for a wavelength of interest onto a fixed detector in order to provide some filtering. Here, we use an actuator to vary the period of the grating in order to modify the far-field pattern.

Each of the grating elements is a reflective beam, and the illumination source is a HeNe laser with a wavelength of 632.8nm. Each beam is connected to its adjacent neighbors using a pair of springs as shown in Figure 99. As the actuator pulls on one end of the grating, the force is distributed evenly along the entire structure and the period of the grating changes uniformly. For a 15 element grating, the motion of the actuator is scaled down by a factor of 15, thus the 80 micron displacement obtained with the SDA results in a change in the period of over 5 um. Aperiodic structures such as chirped gratings or 1-D fresnel lenses (Figure 98) can be designed by calculating the stiffness of each interconnection spring individually.

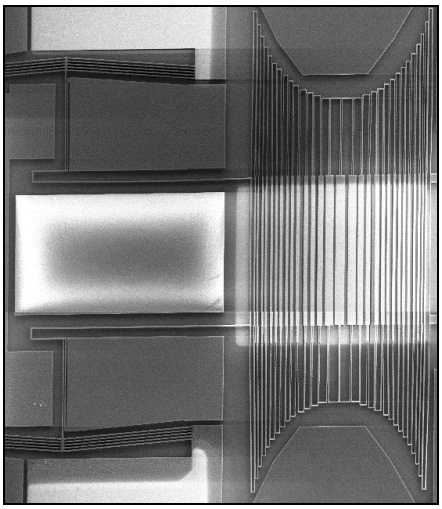

Figure 98: Cylindrical Fresnel lens with spring network demonstrating an aperiodic structure

Since the minimum feature size in the fabrication process is restricted by lithography, the period of the grating is large (6um). The design shown in Figure 100 makes use of a flexure-amplified bent-beam structure to *compress* the grating instead of expanding it, in order to obtain a period that is smaller than the minimum feature size and *decrease* the spatial frequency of the far field pattern, as shown in Figure 100. Unfortunately, this technique results in buckling of the spring structure and does not preserve the far-field pattern's geometry.

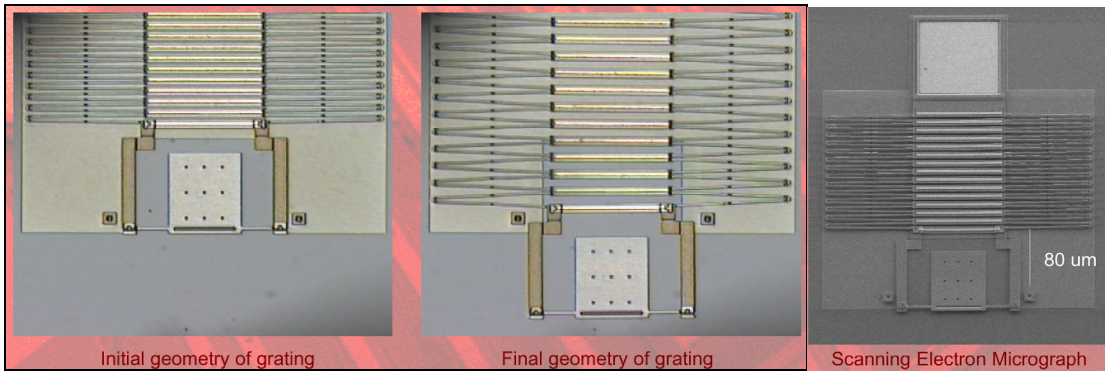

Figure 99: Scratch Drive Actuated grating in the initial position (left) and actuated position (right). SEM shows 80 um range.

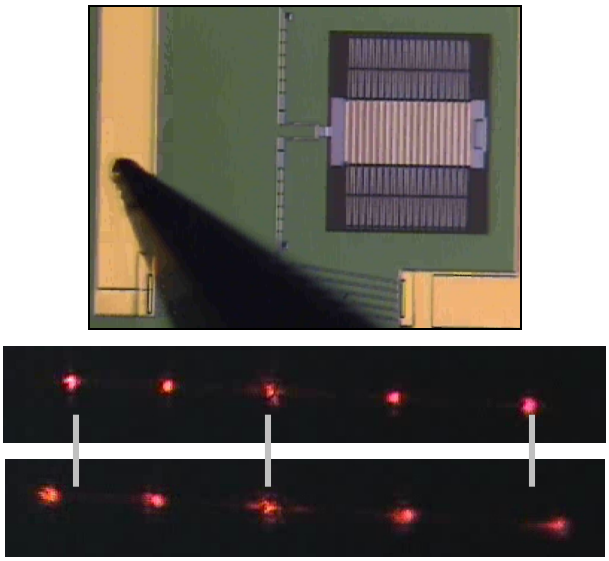

Figure 100: amplified bent beam actuated grating (top) and far field pattern in initial (center) and compressed (bottom) states of actuator. Note the increased spacing of the orders when actuated. Also note that far-field pattern is projected onto inclined surface.

Although the minimum feature size in the MUMPs process is much larger than the operating wavelength of the laser, and the planarity of this surface micromachining process limits the efficiency of the grating, the far field pattern is nevertheless modified as predicted and the concept can be used for wavelength filtering. Several commercially available multi-user processes offer sub-micron patterning, and some have minimum feature sizes of $\approx \frac{\lambda}{2}$. Blazing angles can also be obtained by

electrostatic actuation, as demonstrated by Bright.[136] These process variations may enable higher efficiency variable period gratings with applications in filters and spectrometers.

5.4 1-D Scanning gratings

Varying the angle at which the incoming field impinges on the reflective surface also changes the far-field pattern of a periodic structure. In this case, the spatial frequency of the far-field pattern remains constant but the locations of the maxima are scanned across the screen as the angle changes. In this particular design, a grating is patterned onto the payload of a staggered helical TPDA actuator (Figure 101). Other geometries that can rotate about a fixed axis have been fabricated as well.

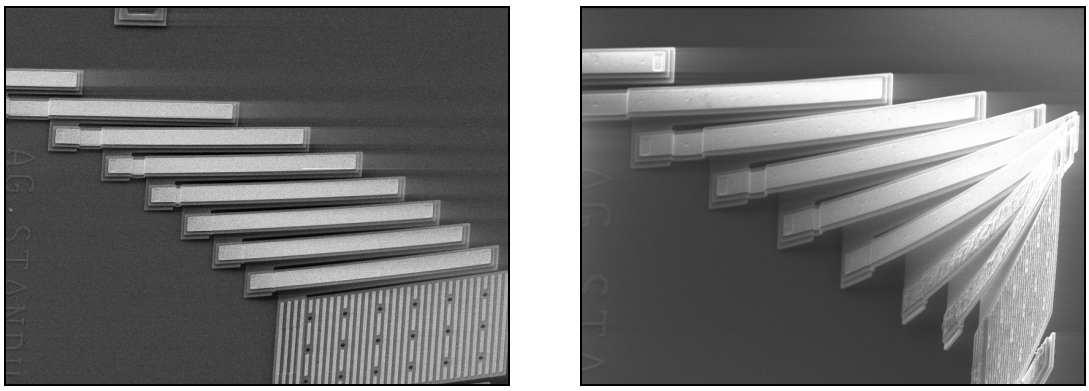

Figure 101: 1-d scanning grating in initial (left) and deformed (right) positions.

As the grating is rotated, the fixed incoming beam experiences a phase shift between the reflectors in the grating. Since the grating is placed at the beam waist, we can approximate the incoming radiation as a plane wave. This means that the phase difference between elements is a linear function of the grating angle. The 1-D and 2-D periodic structures are analyzed using optical phased array techniques. Previous work on 1-D optical phased arrays has generally focused on the use of liquid crystal materials or other variable index materials in order to introduce the phase difference between adjacent elements, with limited beam steering capability.[137] The grating presented here can scan the far-field pattern over 180 degrees since it can be deflected mechanically over 90 degrees.
Figure 102 shows the far field patterns that are projected onto a cylindrical screen when the grating is illuminated by the laser source. When the actuator itself is at the focus of the beam, the far field pattern consists of several vertical sinc functions that are cascaded horizontally. Each of the reflective gold bimorph beams in the actuator can be modeled as a square wave. Under the far field or paraxial approximation, the Fourier transform of the aperture distribution represents the far field pattern, which in this case is a sinc function. Each beam projects a sinc function onto the cylindrical

screen at its own angle with respect to the incoming field, so one can observe 8 distinct sinc patterns corresponding to the 8 beams in the actuator.

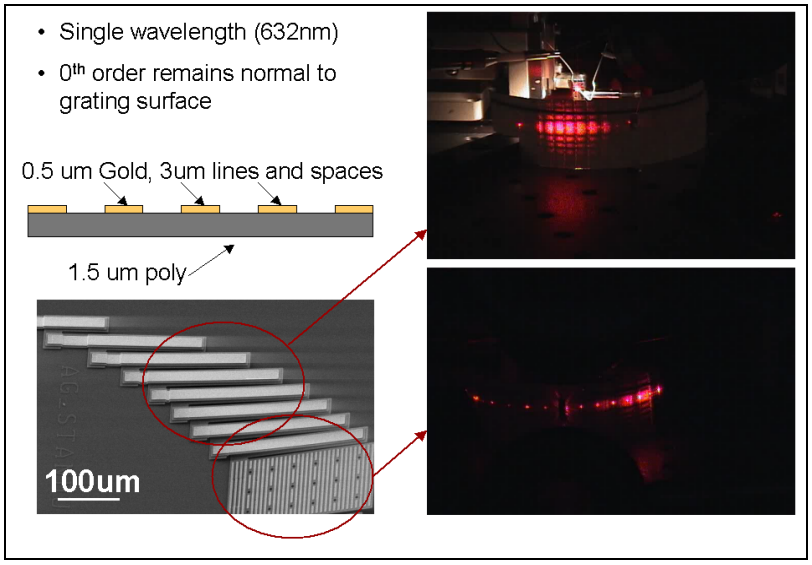

Figure 102: Scanning grating images. Far field pattern when actuator is illuminated (top right) and when grating is illuminated (bottom right).

The methods used to calculate far field patterns for microwave and RF antenna arrays[138] are used here to analyze optical gratings. For a 1-D grating, we assume that each of the reflectors has a phase difference corresponding to its position in the grating and the angle that the grating surface makes with the incoming beam.

The array factor is calculated based on this uniform linear phase distribution.

$$AF(\theta,\varphi) = A_0 \sum_{m=0}^{N-1} I_m e^{jm\alpha + jk_0 md\cos\theta}$$

Here, the term α represents the progressive phase shift between the reflectors that is caused by tilting the grating. Denoting $w = e^{j\alpha + jk_0 d\cos\theta}$ and using the well-known relation:

$$\sum_{n=0}^{N-1} w^n = \frac{1-w^N}{1-w}$$

we obtain:

$$AF(\theta,\varphi) = A_0 e^{j(N-1)(\alpha+k_0 d\cos\theta)/2} \frac{\sin\{[N/2](\alpha+k_0 d\cos\theta)\}}{\sin[(\alpha+k_0 d\cos\theta)/2]}$$

or,

$$\left|AF(\theta,\varphi)\right| = A_0\left|\frac{\sin\{[N/2](\alpha + k_0 d\cos\theta)\}}{\sin[(\alpha + k_0 d\cos\theta)/2]}\right|$$

The position of the main lobe is expressed here as a function of the grating period and the phase factor.

$$\theta_0 = \cos^{-1}\left(-\frac{\alpha}{k_0 d}\right)$$

These expressions are used to calculate the far field patterns for various geometries and compare them with measured results. The three graphs in Figure 103 show the pattern obtained with normal incidence, 30 degree incidence angle, and 15 degree incidence angle. The pattern shifts as expected, and the number of periods in the grating is shown to increase the directivity of each order in the pattern. These results agree well with the measured response as recorded with a CCD in the far field.

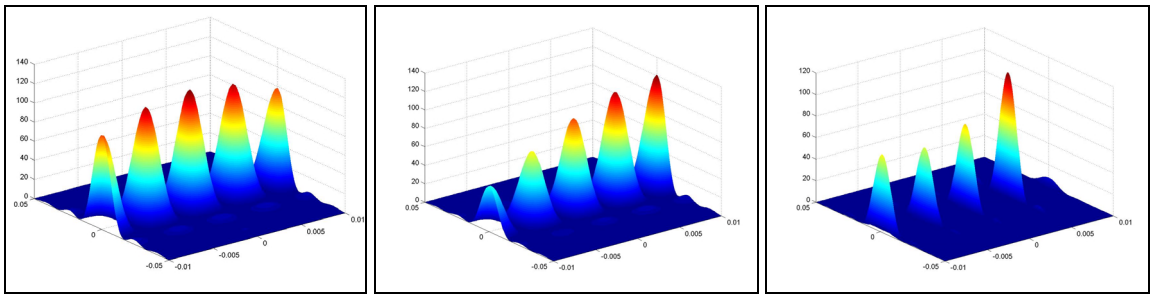

Figure 103: simulation of far field pattern using antenna array approach. Illumination at 0 degrees incidence angle (left), 15 degrees incidence angle (center) and 30 degrees incidence angle with larger number of grating periods (right).

5.5 2-D Scanning gratings

The pattern multiplication principle can be used to extend the analysis of 1-D periodic structures to predict the far-field patterns of 2-D arrays of antennas. Previous work with optical phased arrays to collimate and direct a beam in 2 axes make use of 2 separate linear arrays that are arranged orthogonally.

This approach consists of a planar array of reflectors that is placed on a polysilicon plate. The plate is connected to 3 or 4 vertical TPDA structures that can position to an arbitrary angle with respect to the incoming beam. The structure in Figure 104 can accomplish this with low voltage (~5 V) at high

frequencies. Due to the constraints that are placed on the minimum spacing and line width in the metal layer, the period of the array is 6um, almost 10 λ. This is why a large number of orders is visible in the far field pattern (Figure 104). The array is excited using 2 sinusoidal signals with arbitrary phase and frequency in order to obtain the lissajou patterns that are observed here.

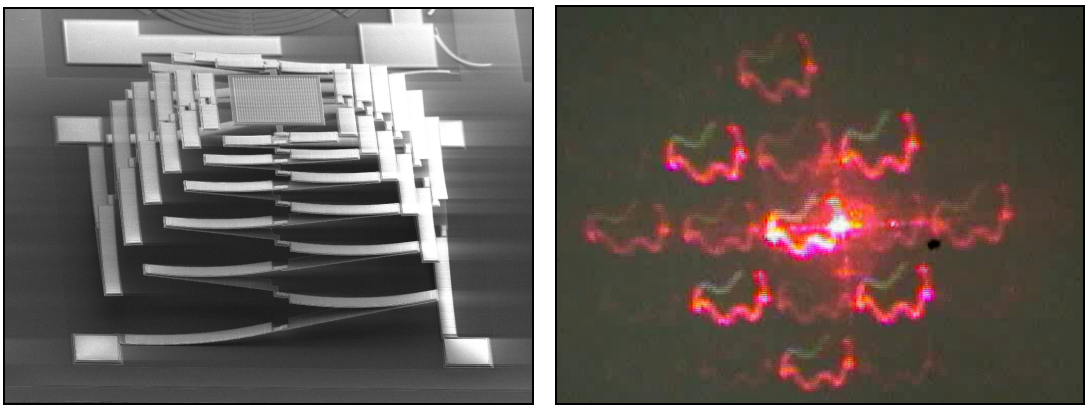

Figure 104: 2-D scanning grating (left) and corresponding far field lissajou pattern from actuated structure (right).

In this case, the array factor for an N x M array of reflectors is expressed as follows:

$$\left|AF(\theta,\varphi)\right| = A_0\left|\frac{\sin\{[N/2](k_0 d\sin\theta\cos\varphi+\alpha)\}}{\sin[(k_0 d\sin\theta\cos\varphi+\alpha)/2]}\right|\times\left|\frac{\sin\{[M/2](k_0 d\cos\theta+\beta)\}}{\sin[(k_0 d\cos\theta+\beta)/2]}\right|.$$

The principle maximum of the far field pattern, or the location of the zero order, is calculated with the following expressions:

$$\begin{aligned} k_0 d\sin\theta_0\cos\varphi_0 &= -\alpha \\ k_0 d\cos\theta_0 &= -\beta \end{aligned}.$$

In the xy plane, the half power beamwidth and the beam width between first nulls are calculated as follows:

$$HPBW_{xy} \approx 0.886\frac{\lambda}{Nd}$$

$$BWFN_{xy} \approx \frac{2\lambda}{Nd}$$

These expressions are also used in the yz plane:

$$HPBW_{yz} \approx 0.886\frac{\lambda}{Md}$$

$$BWFN_{yz} \approx \frac{2\lambda}{Md}$$

Finally, the directivity of the beam can be expressed as follows:

$$D \approx \frac{4\pi}{2 \times HPBW_{xy} HPBW_{yz}} \approx \frac{8MNd^2}{\lambda_0^2} = 8\frac{A}{\lambda_0^2}$$

A matlab program was written to calculate the far-field patterns of 2-D periodic structures using these expressions, and some of the results are presented here (Figure 105).

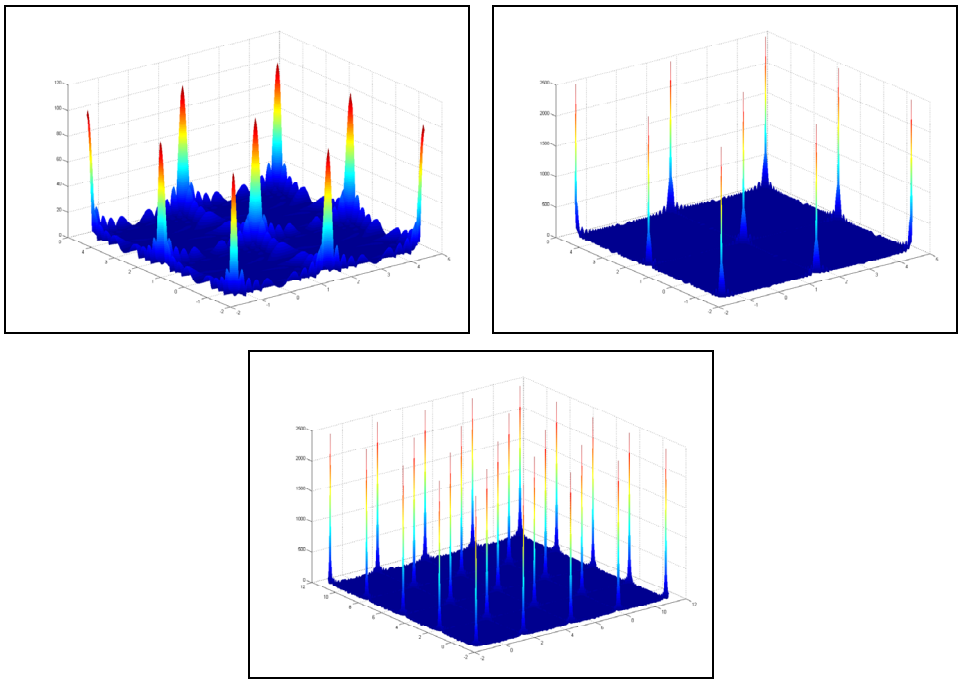

Figure 105: simulated far-field patterns of 2-D grating structures. Top left: pitch = 2 lambda, N=100, M=10; top right: pitch = 2 lambda, N=100, M=100; bottom: Pitch = 4 lambda, N=10, M=10.

The simulated results demonstrate the effects that the grating structure has on the far field pattern. Increasing the number of reflective elements improves the directivity of the beams, as expected based on the directivity equation above. Increasing the spacing or pitch of the individual reflectors "compresses" the far field pattern, or increases its spatial frequency.

As the minimum feature sizes are reduced, the higher orders will be eliminated from the far field pattern and an efficient grating can be designed in order to achieve good directivity and large steering angle. This periodic structure can then be used to collimate and redirect a beam simultaneously to an arbitrary position in φ and θ.

Chapter 6 Conclusions and Future Work

Research in MEMS is continuing to advance at rates that are commensurate with the IC industry, as evidenced by the rapidly growing number of relevant publications, conferences, large research initiatives, and corporate and academic research groups whose efforts are focused on the area. Mature MEMS products have been incorporated in consumer electronics (ink jet printers, displays), automotive (accelerometers) and aerospace applications (various sensors). Several fabrication processes are becoming widely available to researchers at reasonable costs and turnaround times.

Due to the planar nature of most MEMS fabrication processes, it is difficult to obtain truly three-dimensional structures without some form of assembly. The TPDA (thermal plastic deformation assembly) technique developed here is a proposed method of obtaining devices with complex structure that can be assembled in a controlled batch process.

High forces and large displacements are often required to alter the geometry of a device significantly. For instance, in optical devices such as beam steering mirrors, large angular deflections are beneficial. Large displacement linear actuators are also desirable since they can increase the tuning range of RF devices such as variable capacitors and optical devices such as variable period gratings. Several geometries of TPDA actuators and amplified bent beam actuators have been developed to provide this functionality.

Finally, power consumption is a significant characteristic of any electronic device, and many of the actuation techniques that are commonly used in MEMS require high voltages or large currents to generate large displacements. MEMS that are useful for tuning (in RF devices) or microalignment (in optical devices) usually require constant voltages or currents to maintain a desired static deflection. The TPDA and mechanical latching methods that were developed here could reduce quiescent power consumption in some applications.

Future work in RF MEMS will involve the use of TPDA structures as tuning elements in RF circuits that are fabricated on suitable substrates with appropriate conductors. The devices presented in the RF MEMS section have demonstrated the use of novel actuation techniques and TPDA to achieve tunable RF devices that can maintain a desired position without any quiescent power consumption. Although the functionality of these devices was confirmed and the tuning concepts

were successfully validated, the RF performance was compromised by materials selection and fabrication process details.

As was the case with the design of actuators, material properties are of critical importance in RF design. Conductors with low resistive losses and sufficient thickness are essential to obtain reasonable Q. Substrates with sufficiently high dielectric constants should be used to eliminate parasitic losses associated with eddy currents and capacitive coupling, among other factors. These considerations make most commercially available MEMS processes impractical due to the use of silicon substrates and thin conductors. If RF MEMS devices with high Q's are desired, one must begin with materials selection and define an appropriate fabrication process. The SU8 molding and copper electroplating process that is carried out on Pyrex substrates is a good candidate for the fabrication of inductors and the latched capacitor design discussed above. A proposed TPDA process that would yield higher Q's while providing TPDA functionality is described in figure 107 below. This process would be appropriate for the coupler and variable inductor structures described above, and could also be used to fabricate other three dimensional RF structures such as helical inductors.

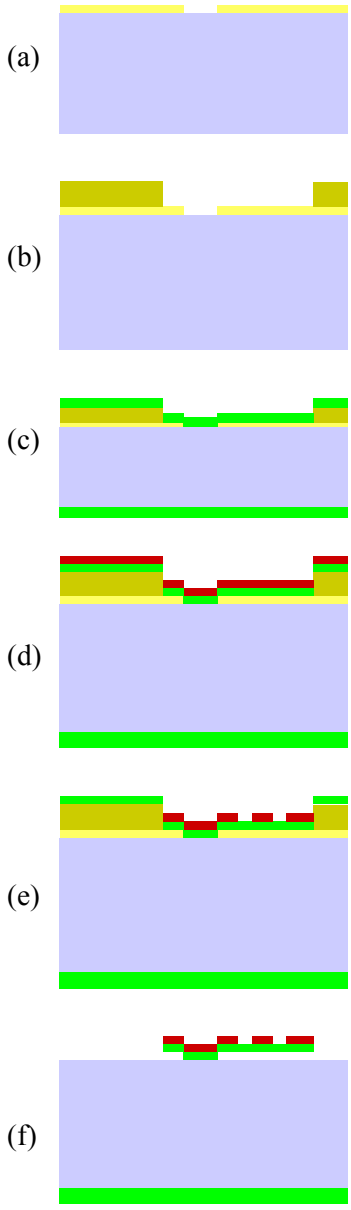

Start with dielectric substrate (ie. alumina), spin sacrificial photoresist and pattern anchors

Spin and pattern thick photoresist for liftoff

Deposit thin film of metal1 using evaporation, sputtering or plating. Deposit ground plane on backside of substrate.

Deposit thin film of metal2

Pattern metal1

Perform liftoff and remove sacrificial layers (release step)

Figure 106: process flow for RF applications of TPDA

Future work in optical MEMS will focus on the incorporation of scanning micromirrors and gratings in displays and imaging systems. Periodic structures with 3-D geometry such as variable curvature gratings have been fabricated, and simulations of these devices are underway as well. Since the minimum feature sizes in MEMS fabrication processes are approaching dimensions that are closer to optical wavelengths, these devices will become more practical for filtering and beam steering applications.

Appendix A
Research Instrumentation

UMECH MEMS Motion Analyzer

The Umech system was used in order to obtain detailed measurements of the MEMS actuators presented here. It can provide motion analysis in 3 dimensions over the frequency range of 1Hz – 10MHz, with nanometer resolution. The datasheet for this instrument is included below.

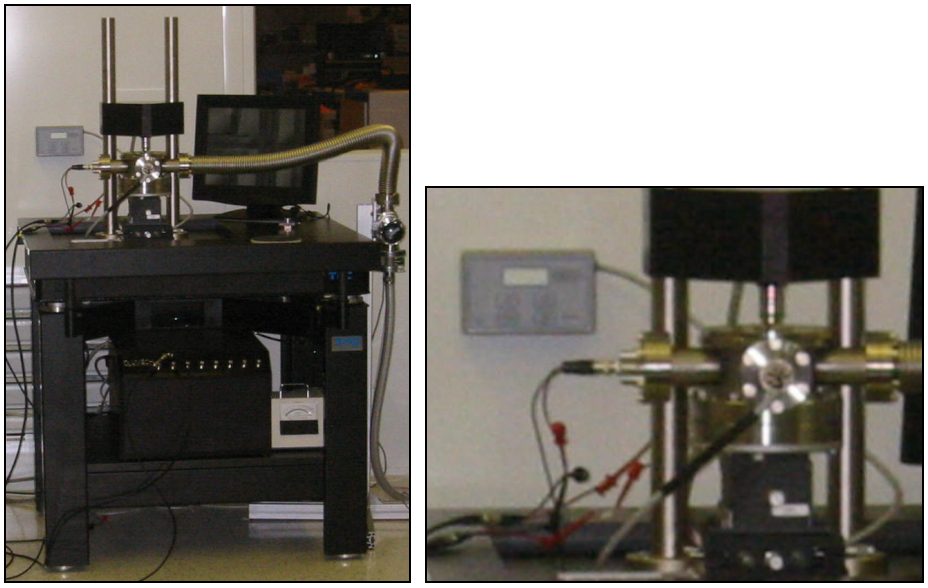

Figure 107: Umech system with vacuum attachment (left) and close-up of sample chamber (right)

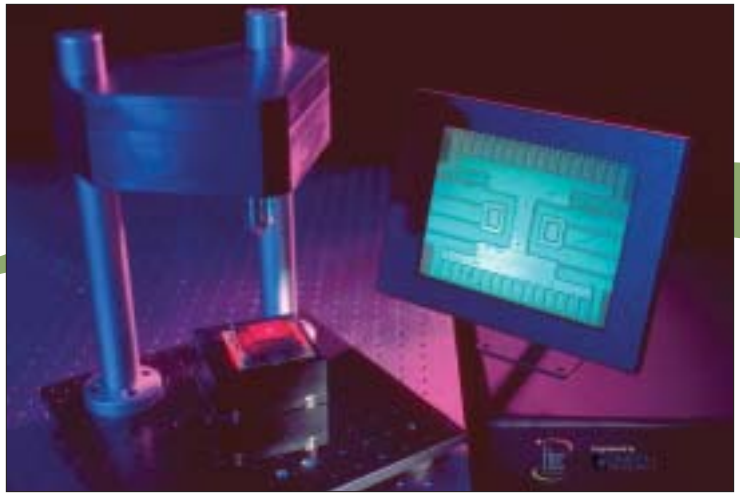

- Test and characterize the motions of virtually any MEMS/MOEMS device, including VOA's, OXC's, Optical Switches, 2-D and 3-D micro-mirrors
- Measure an individual microstructure, or arrays of microstructures simultaneously
- A precision instrument ideal for the MEMS development lab. Can also be integrated with Etec's M/STeP-o™ system for volume production applications
- Measure in-plane and out-of-plane motions with nanometer resolution, at frequencies from 1Hz to 10MHz
- Analyze resonant behavior, transient response, settling time, switching time, and complex motion profiles; all with point and click operation
- Powerful data analysis and report generation tools enable clear presentation of complex motion data
- Optional built-in profilometer for static measurements such as mirror curvature and surface roughness

MEMS Motion Analyzer

The MEMS Motion Analyzer is a turnkey system for characterizing the complex motions of MEMS/MOEMS. This fully integrated system includes a high performance imaging system, drive electronics, data acquisition, and data analysis software. A powerful report generator provides highly detailed information in a format ideal for MEMS researchers. Real-time slow motion video provides a visual display of the MEMS motion in 3-dimensions.

The system can measure motions in 3-dimensions (6 degrees-of-freedom) at frequencies from 1Hz to 10MHz with nanometer resolution. The MEMS Motion Analyzer combines video microscopy, stroboscopic illumination, and proprietary algorithms to analyze the motions of individual microstrucures or arrays of MEMS structures simultaneously.

Summary Specifications

Software specifications

User interface	Java applet running on user's computer
Raw data format	1280x1024 pixel array
Analyzed data format	Java graphical interface
User access to raw data format	Tab delimited text, GIF (images)

Arbitrary waveform generator specifications

Frequency range	1Hz –10MHz
Sample rate	40MHz
Memory depth	8k
Resolution	10-bit
Channels	1 to 15
Output	±10V@10mA ±100V@10mA (optional)

Included accessories

Vibration isolation system and optical bench, built-in video microscope, xyz positioner, server PC, and report generator

Optical and motion analysis specifications

Objective lens	5x	10x	20x	50x
Numerical aperture	0.13	0.25	0.4	0.6
In-plane motion resolution	40nm	20nm	10nm	4nm
Out-of-plane motion resolution	0.5nm	0.5nm	0.5nm	0.5nm
X Field of view	1.6mm	0.8mm	0.4mm	0.16mm
Y Field of view	1.2mm	0.6mm	0.35mm	0.12mm
Maximum tilt angle motion range	±2.5˚	±5˚	±10˚	±15˚
Working distance	20mm	15mm	12mm	4mm

Custom optical solutions available.

Facilities requirements

Electrical	115/230 VAC, 50/60 Hz, 15A
Compressed air	80 psi
Footprint	Optical table,30" x 36"
Host computer	Customer provided PC with monitor

All specifications are subject to change without prior notification.

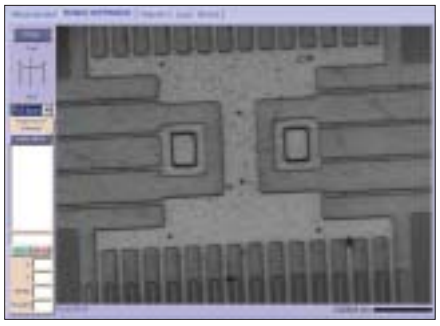

Built-in data animator provides quick and convenient data verification and visualization.

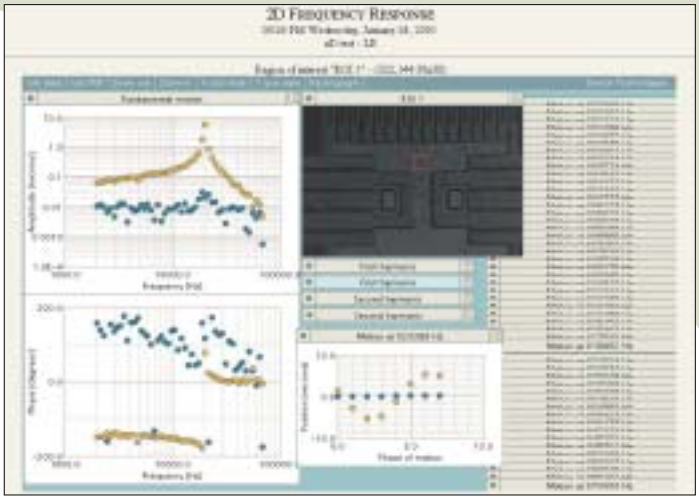

Reports summarize frequency response and motion data for in-plane and out-of-plane motion.

LASERLIGHT
1 mW at 658 nm
DO NOT STARE INTO BEAM OR VIEW
DIRECTLY WITH OPTICAL INSTRUMENTS

CDRH CLASS II LASER PRODUCT
IEC/EN CLASS 3A LASER PRODUCT

Engineered by UMECH TECHNOLOGIES

Protected by patents issued and/or pending.

Etec, Inc. ❙ 83 Pine Street ❙ Peabody, MA 01960
Toll Free 800-992-ETEC ❙ T 978-535-7683 ❙ F 978-535-7003 ❙ www.etec-inc.com ❙ info@etec-inc.com ❙

LEO 1550 SEM

This instrument was used to capture most of the images of MEMS devices that are presented here. It has a large sample chamber that accommodates a 4-probe nanomanipulator in order to allow vacuum SEM measurements on the device under test. The maximum magnification is 800 000x and the resolution of the instrument can be as high as 1 nm; however, for the purposes of imaging MEMS devices, the requirements of magnification and resolution are far below the instrument's capabilities.

Figure 108: LEO 1550 Scanning Electron Microscope

S100 Nanomanipulator

The Zyvex S100 Nanomanipulator fits in the LEO sample chamber and provides DC probes that allow the user to power MEMS devices in vacuum under the high magnification of the SEM. Measurements on electrothermal devices under vacuum conditions can be compared to simplified FEA models, since the convective effects that are present in ambient conditions can be neglected. Also, the resonant amplitudes of devices are larger since the squeeze film damping effects are no longer present.

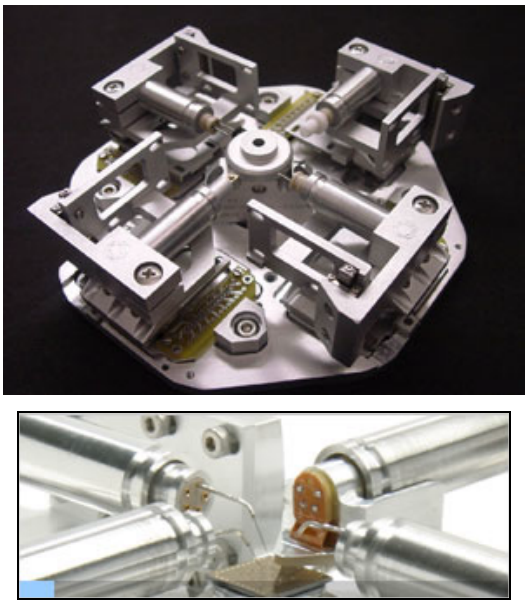

Figure 109: S100 4 probe nanomanipulator (top) and close-up of MEMS probing (bottom)

DC and RF Probe Stations

Most of the routine characterization of actuators was performed on a DC probe station with multiple micromanipulator-mounted probes. During the testing of optical devices, or when a large number of electrical interconnects was required (>6), the device was placed on a cerdip or can package and a wirebonder was used for electrical interconnect. The DC power is supplied by a MEMS driver station capable of providing arbitrary waveforms from 0-250V, with 0-4A per channel. A miniaturized MEMS driver station with a lower voltage limitation (30 V) is suitable for driving electrothermal devices.

For high frequency measurements, the probe station is equipped with RF probes that have a CPW interface. For frequencies ranging from 300kHz to 50 MHz, the data was obtained using the Agilent 8714ES VNA, and at higher frequencies (50 MHz – 20 GHz) the Agilent 8722ES was used.

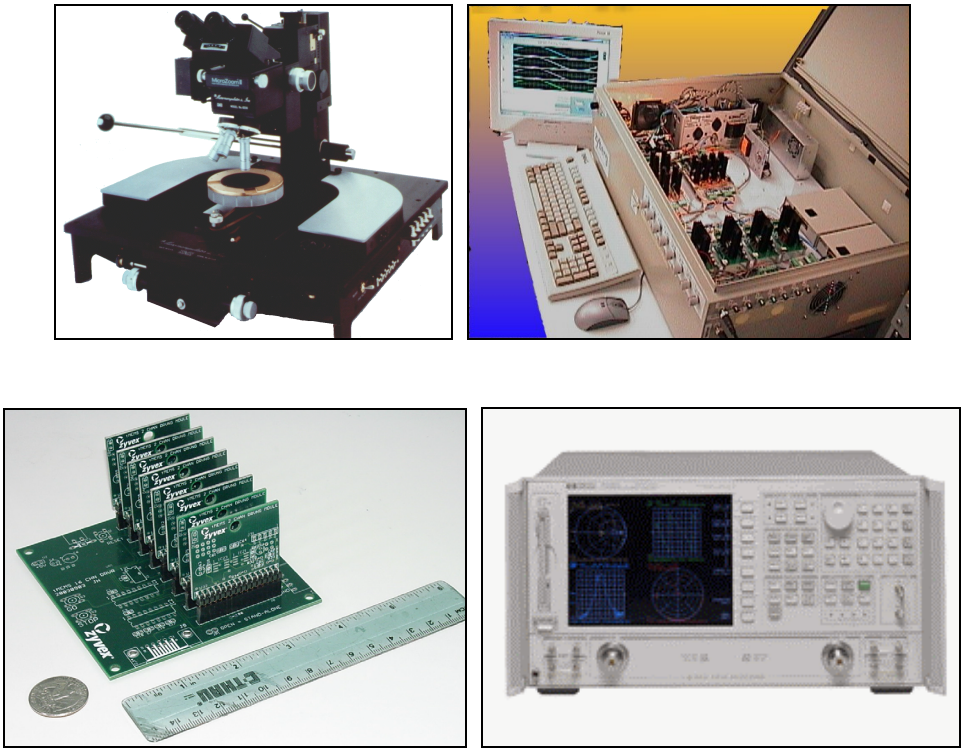

Figure 110: Wafer probing system (top left), MEMS driver station (top right), tMEMS miniature driver station (bottom left), VNA (bottom right)

Autocollimator

This instrument was custom-built by Dr. Greg Magel in order to obtain precise angular measurements between MEMS devices. It can also be used to measure the stability, drift, and angular deflection of micromirrors over small angular ranges with a resolution better than 0.0001 degrees.

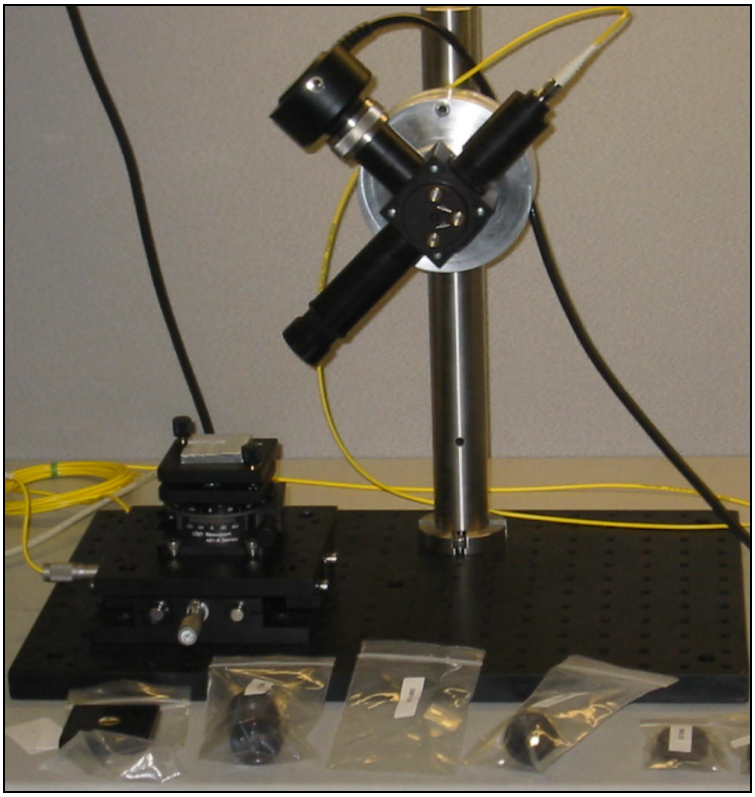

Figure 111: autocollimator

Software

The following software was used for design, layout and simulation of the actuators and devices that are reported.

LASI for layout and GDS file generation.

ZYRIC for design rule checking and mask file generation.

Memulator for process simulation, now available as part of Coventor.

Hypermesh for pre and post processing in FEA problems.

Ansys for FEA solver.

Matlab code for antenna array calculations.

HPADS and Sonnet for simulations of planar RF structures.

Some screen captures from the software listed above are included here.

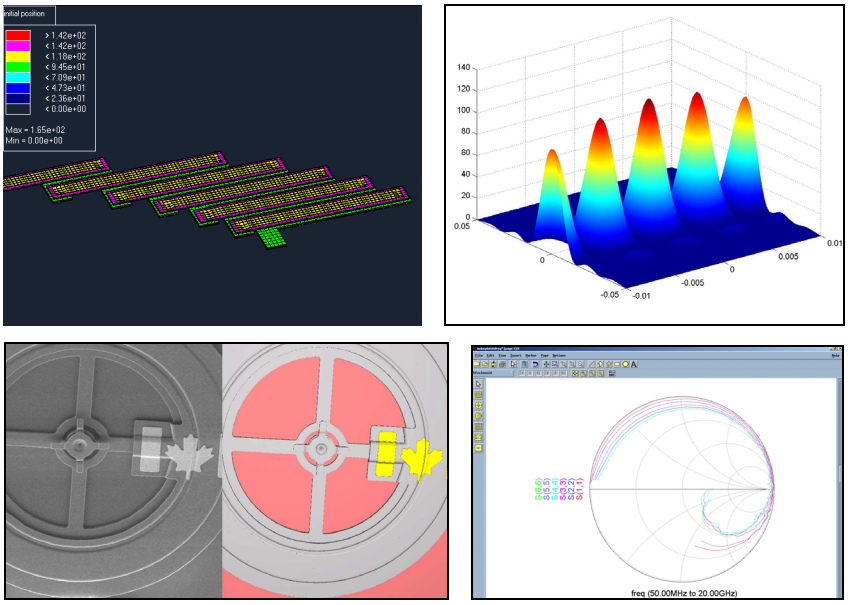

Figure 112: top left, Hypermesh; top right, Matlab far-field simulation; bottom left, Memulator; bottom right, HPADS.

Bibliography

[1] Moore, Gordon E., "Cramming more components onto integrated circuits," Electronics, Volume 38, Number 8, April 19, 1965.

[2] Kovacs, Gregory T.A., "Micromachined Transducers Sourcebook," McGraw-Hill, p.3, 1998

[3] Petersen, Kurt E. "Silicon as a Mechanical Material," Proceedings of the IEEE, Vol 70(5), pp. 420-457, May 1982.

[4] Madou, M., "Fundamentals of Microfabrication," CRC Press, 1997.

[5] S.M. Sze , VLSI Technology, McGraw-Hill 1988

[6] Bustillo, J., Howe, Roger R.T., Muller, R.S., "Surface Micromachining for Microelectromachanical Systems," *Proceedings of the IEEE,* ***Vol.86, No. 8,*** August 1998, pp. 1552-1574.

[7] Howe, Roger T., Muller, Richard S., Gabriel, Kaigham J., and Trimmer, William S. N., "Silicon micromechanics: sensors and actuators on a chip." IEEE Spectrum, July 1990. pp 29-35.

[8] Tas, N Sonnenberg, T Jansen, H Legtenberg, R and Elwenspoek, M. "Stiction in Surface Micromachining," *J. Micromech. Microeng.* **6** (1996) 385-397

[9] Maboudian, R., Ashurst, W., Carraro, C., "Self-Assembled monolayers as anti-stiction coatings for MEMS: characteristics and recent developments," *Sensors and Actuators* **v.82,** (2000) pp.219-223.

[10] Israelachvili J N 1992 *Intramolecular and Surface Forces* (London: Academic)

[11] Tas, N., Sonnenberg, T., Jansen, H., Legtenberg, R., Elwenspoek, M., "Stiction in surface micromachining," *J Micromech. Microeng.* **vol. 6, No. 4** (1996) 385-397.

[12] Stengl R, Tan T and Gosele U, "A model for the silicon wafer bonding process," *Japan. J. Appl. Phys.* **vol. 28** (1989) pp. 1735-41.

[13] Mastrangelo C. H., Hsu, C. H., "A simple experimental technique for the measurement of the work of adhesion of microstructures," *Proc. IEEE Solid-State Sensors and Actuators Workshop (Hilton Head Island, SC, 1992)* pp. 208-12.

[14] C.J. Kim, UCLA extension course on MEMS.

[15] Abe T and Reed M, "Control of liquid bridging induced stiction of micromechanical structures," *J. Micromech. Microeng.* **v. 6** (1996) 213-217.

[16] Smith B, Sniegowski J, LaVigne G. and Brown G, "Thin Teflon-like films for eliminating adhesion in released polysilicon microstructures," *Sensors and Actuators A,* **70** (1998) pp.159-163.

[17] P.F. Man, B.P. Gogoi, C.H. Mastrangelo, "Elimination of post-release adhesion in microstructures using thin conformal fluorocarbon coatings," *J. Microelectromech. Stst.,* **vol. 6** (1997) pp. 25-34.

[18] Schwartz, D., "Mechanisms and Kinetics of Self Assemble Monolayer Formation," *Annu. Rev. Phys. Chem.* (2001) **vol. 52** pp. 107-37.

[19] Kim, B. J., Kim, G.M., Liebau, M., Huskens, J., Reinhoudt, D.N., Brugger, J., "SAMs meet MEMS: Surface modification with self-assembled monolayers for the dry-demolding of photoplasmic MEMS/NEMS," *IEEE MEMS 2001 conference proceedings,* pp.106-109.

[20] Ashurst, W. "Alkene based monolayer films as anti-stiction coatings for polysilicon MEMS," *Berkeley Sensors and Actuator Center internal publication.*

[21] Fujita, Hiroyuki, "Microactuators and Micromachines," *Proceedings of the IEEE,* **vol 86, no 8,** (1998) pp. 1721-1732.

[22] Arokia Nathan, Henry Baltes, "Microtransducer CAD, Physical and Computational Aspects," Vienna: Springer-Verlag, Vienna, 1999, chapter 8.

[23] Bright, V.M., Comtois, J.H., "Applications for surface-micromachined polysilicon thermal actuators and arrays," *Sensors and Actuators A,* **Vol. 58,** (1997) pp. 19-25.

[24] Long Que; Jae-Sung Park; Gianchandani, Y.B., "Bent-Beam electro-thermal actuators for high force applications," in *Proc. IEEE MEMS '99, International Conference on Micro Electro Mechanical Systems,* Orlando, FL, 1999, pp. 31-36.

[25] Long Que; Jae-Sung Park; Gianchandani, Y.B., "Bent-beam electrothermal actuators-Part I: Single beam and cascaded devices," *Journal of Microelectromechanical Systems,* **vol. 10, no. 2,** June 2001, pp. 247 - 254.

[26] Long Que; Jae-Sung Park; Gianchandani, Y.B., "Bent-beam electrothermal actuators-Part II: Linear and Rotary Microengines," *Journal of Microelectromechanical Systems,* **vol. 10, no. 2,** June 2001, pp. 255 - 262.

[27] Tuantranont, A., Liew, L., Bright, V., Zhang, W., Lee, Y.C., "Phase-only micromirror array fabricated by standard CMOS process," *Sensors and Actuators A,* **Vol. 89,** (2001) pp. 124-134.

[28] Chen, W., Chu, C., Hsieh, J., Fang, W., "A reliable single-layer out-of-plane micromachined thermal actuator," *Sensors and Actuators A,* **Vol. 103,** (2003) pp. 48-58.

[29] T. Akiyama, K. Shono, "Controlled Stepwise Motion in Polysilicon Microstructures," *Journal of Microelectromechanical Systems,* **vol. 2, no. 3,** Sept 1993, pp. 106 - 110.

[30] R. Linderman, V.M. Bright, "Nanometer precision positioning robots utilizing optimized scratch drive actuators," *Sensors and Actuators A,* **vol. 91** (2001) pp. 292-300.

[31] Tang, W.C.; Nguyen, T.-C.H.; Howe, R.T., "Laterally driven polysilicon resonant microstructures," *proceedings, An Investigation of Micro Structures, Sensors, Actuators, Machines and Robots*. IEEE, 20-22 Feb. 1989 pp. 53 –59.

[32] Ye, W., Mukherjee, S., MacDonald, N., "Optimal Shape Design of an Electrostatic Comb Drive in Microelectromechanical Systems," *Journal of Microelectromechanical Systems,* **vol. 7, no. 1,** March 1998, pp. 16-26.

[33] Nemirovsky, Y., Bochobza-Degani, O., "A Methodology and Model for the Pull-In Parameters of Electrostatic Actuators," *Journal of Microelectromechanical Systems,* **vol. 10, no. 4,** Dec 2001, pp. 601 - 615.

[34] Nadal-Guardia, R., Dehe, A., Aigner, R., Castaner, L., "Current Drive Methods to Extend the Range of Travel of Electrostatic Microactuator Beyond the Voltage Pull-in-Point," *Journal of Microelectromechanical Systems,* **vol. 11, no. 3,** June 2002, pp. 255 - 263.

[35] Hisanaga, M.; Koumura, T.; Hattori, T., "Fabrication of 3-dimensionally shaped Si diaphragm dynamic focusing mirror," Micro Electro Mechanical Systems, 1993, MEMS '93, Proceedings 'An Investigation of Micro Structures, Sensors, Actuators, Machines and Systems'. IEEE. , 7-10 Feb. 1993, Page(s): 30 –35.

[36] Goldsmith, C.; Tsen-Hwang Lin; Powers, B.; Wen-Rong Wu; Norvell, B., "Micromechanical membrane switches for microwave applications," Microwave Symposium Digest, 1995., IEEE MTT-S International , 16-20 May 1995 Page(s): 91 -94 vol.1.

[37] M. Shikida, K. Sato, T. Harada, "Fabrication of a S-Shaped Microactuator," *Journal of Microelectromechanical Systems,* **vol. 6, no. 1,** March 1997, pp. 18-24.

[38] M. Yamaguchi, S. Kawamura, K. Minami, M. Esashi, "Control of Distributed Electrostatic Microstructures," *J. Micromech. Microeng.,* **Vol. 3,** (1993) pp. 90-95.

[39] Van Kessel, P., Hornbeck, L., Meier, R., Douglass, M., "A MEMS-Based Projection display," *Proceedings of the IEEE,* **Vol. 86, No. 8,** Aug 1998, pp. 1687 – 1704.

[40] T. Higuchi, Y. Yamagata, K. Furutani, and K. Kudoh, "Precise Positioning mechanism utilizing rapid deformations of piezoelectric elements," in *Proc. IEEE Micro Electro Mechanical Syst. Workshop (MEMS '90),* Feb. 1990, pp. 222-226.

[41] O. Ohmichi, Y. Yamagata, T. Higuchi, "Micro Impact Drive Mechanisms Using Optically Excited Thermal Expansion," *Journal of Microelectromechanical Systems,* **vol. 6, no. 3,** Sept 1997, pp. 200 - 207.

[42] Y. Yamagata, T. Higuchi, N. Nakamura, and S. Hamamura, "A micro mobile mechanism using thermal expansion and its theoretical analysis," in *Proc. IEEE Micro Electro Mechanical Syst. Workshop (MEMS '94),* Feb. 1994, pp. 142-147.

[43] Johnson, D., "Vacuum-deposited TiNi shape memory film: characterization and applications in microdevices," J Micromech. Microeng. **1** (1991) 34-41.

[44] Krulevitch, P., Lee, A., Ramsey, P., Trevino, J., Hamilton, J., Northrup, A., "Thin Film Shape Memory Alloy Microactuators," *Journal of Microelectromechanical Systems,* **vol. 5, no. 4,** Dec 1996, pp. 270 - 282.

[45] Niarchos, D., "Magnetic MEMS: Key issues and some applications," *Sensors and Actuators A,* **Vol. 106,** (2003) pp. 255-262.

[46] Judy, J., Muller, R., Zappe, H., "Magnetic Microactuation of Polysilicon Flexure Structures," *Journal of Microelectromechanical Systems,* **vol. 4, no. 4,** Dec 1995, pp. 162 - 169.

[47] Yan, D., Khajepour, A., Mansour, R., "Modeling of two-hot-arm horizontal thermal actuator," *J. Micromech. Microeng.,* **Vol. 13,** (2003) pp. 312-322.

[48] M. Mermelstein, *UMECH Manual:* UMECH Technologies LLC, 2001.

[49] Ellis, M., Skidmore, G., Sarkar, N., "Finite Element Analysis and Vacuum Testing of Thermal Bimorph Actuators," presented at *TEXMEMS III, Dallas, TX, 2001.*

[50] Kota, S.; Hetrick, J.; Zhe Li; Rodgers, S.; Krygowski, T., "Synthesizing high-performance compliant stroke amplification systems for MEMS," *Micro Electro Mechanical Systems, 2000. MEMS 2000. The Thirteenth Annual International Conference on* , 23-27 Jan. 2000
Page(s): 164 -169

[51] Jonsmann, J.; Sigmund, O.; Bouwstra, S., "Compliant electro-thermal microactuators," *Micro Electro Mechanical Systems, 1999. MEMS '99. Twelfth IEEE International Conference on ,* 17-21 Jan. 1999, Page(s): 588 -593

[52] Guangya, Z., Dowd, P., "Tilted folded beam suspension for extending the stable travel range of comb-drive actuators," *J. Micromech. Microeng.,* **Vol. 13,** (2003) pp. 178-183.

[53] Jensen, B., Mutlu, S., Miller, S., Kurabayashi, K., Allen, J., "Shaped Comb Fingers for Tailored Electromechanical Restoring Force," *Journal of Microelectromechanical Systems,* **vol. 12, no. 3,** June 2003, pp. 373-383.

[54] Tang, W., Lim, M., Howe, R., "Electrostatic Comb Drive Levitation and Control Method," *Journal of Microelectromechanical Systems,* **vol. 1, no. 4,** Dec 1992, pp. 170-178.

[55] Li, K., Cho, Y., "Laterally Driven Electrostatic Repulsive-Force Microactuators Using Asymmetric Field Distribution," *Journal of Microelectromechanical Systems,* **vol. 10, no. 1,** March 2001, pp. 128 - 136.

[56] Petersen, K.E., "Dynamic Micromechanics on silicon: Techniques and Devices," *IEEE Transactions on Electronic Devices,* **Vol. ED-25, no.10.,** Oct. 1978, pp. 1241-1250.

[57] Nadal-Guardia, R., Dehe, A., Aigner, R., Castaner, L., "Current Drive Methods to Increase the Range of Travel of Electrostatic Microactuators Beyond the Voltage Pull-in-Point," *Journal of Microelectromechanical Systems,* **vol. 11, no. 3,** June 2002, pp. 255 - 263.

[58] Akiyama T, Collard D and Fujita H, Scratch drive actuator with mechanical links for self-assembly of three-dimensional MEMS *J. Microelectomech. Systems,* **6** 10-17

[59] Miki, N., Shimoyama, I., "Dynamics of a Microflight Mechanism With Magnetic Rotational Wings in an Alternating Magnetic Field," *Journal of Microelectromechanical Systems,* **vol. 11, no. 5,** Oct. 2002, pp. 584 - 591.

[60] Lagorce, L., Brand, O., Allen, M., "Magnetic Microactuators based on Polymer Magnets," *Journal of Microelectromechanical Systems,* **vol. 8, no. 1,** March 1999, pp. 2-9.

[61] Judy, J., Muller, R., Zappe, H., "Magnetic Microactuation of Polysilicon Flexure Structures," *Journal of Microelectromechanical Systems,* **vol. 4, no. 4,** December 1995, pp. 162-169.

[62] Bourouina, T., Lebrasseur, E., Reyne, G., Debray, A., Fujita, H., Ludwig, A., Quandt, E., Muro, H., Oki, T., Asaoka, A., "Integration of Two Degree-of-Freedom Magnetostrictive Actuation and Piezoresistive Detection: Application of a Two-Dimensional Optical Scanner," *Journal of Microelectromechanical Systems,* **vol. 11, no. 4,** August 2002, pp. 355-361.

[63] Nam, H., Kim, Y., Cho, S., Yee, Y., Bu, J., "Low Voltage PZT Actuated tilting micromirror with hinge structure," *IEEE/LEOS International Conference on Optical MEMS, 2002.* Aug. 2002, pp. 89-90.

[64] Hoivic, N., Lee, Y., Bright, V., "Flip Chip High Q MEMS Capacitor of RF Applications," *Proceedings of the Pacific RIM/ASME International Electronic Packaging Technical Conference and Exibition,* July 2001, IPACK2001-15545.

[65] Masters, N., Howell, L., "A Self-Retracting Fully Compliant Bistable Mechanism," *Journal of Microelectromechanical Systems,* **vol. 12, no. 3,** June 2003, pp. 273-280.

[66] Gomm, T., Howell, L., Selfridge, R., "In-plane linear displacement bistable microrelay," *J. Micromech. Microeng.,* **Vol. 12,** (2002) pp. 257-264.

[67] Vangbo, M., Backlund, Y., "A Lateral Symetrically Bistable Buckled Beam," *J. Micromech. Microeng.,* **Vol. 8,** (1998) pp. 29-32.

[68] Designed by Matthew Ellis at Zyvex corporation

[69] US patent pending, filed by Aaron Geisberger

[70] Pister, K., Judy, M., Burgett, S., Fearing, R., "Microfabricated Hinges," *Sensors and Actuators,* **Vol. A33, no. 3,** (1992) pp. 249-256.

[71] Hui, E., Howe, R., Rodgers, M., "Single Step Assembly of Complex 3-D Microstructures*," Micro Electro Mechanical Systems, 2000. MEMS 2000. The Thirteenth Annual International Conference on*, 23-27 Jan. 2000 Page(s): 602 –607.

[72] Wu, M., Lin, L., Lee, S., Pister, K., "Micromachined free-space integrated micro-optics," *Sensors and Actuators,* **Vol. A 50,** (1995) pp. 127-134.

[73] Tien, N., Solgaard, O., Kiang, M., Daneman, M., Lau, K., Muller, R., "Surface-Micromachined Mirrors for laser-beam positioning," *Sensors and Actuators,* **Vol. A 52,** (1996) pp. 76-80.

[74] Lai, K., Hui, A., Li, W., "Non-Contact Batch Micro-Assembly by Centrifugal Force," *Micro Electro Mechanical Systems, 2002. MEMS 2002. The Fifteenth Annual International Conference on*, Jan. 2002.

[75] Kaajakari, V., Lal, A., "Thermokinetic Actuation for Batch Assembly of Microscale Hinged Structures," *Journal of Microelectromechanical Systems,* **vol. 12, no. 4,** Aug. 2003, pp. 425-432.

[76] Green, P., Syms, R., Yeatman, E., "Demonstration of Three-Dimensional Microstructure Self-Assembly," *Journal of Microelectromechanical Systems,* **vol. 4, no. 4,** Dec. 1995, pp. 170-176.

[77] Syms, R., Yeatman, E., Bright, V., Whitesides, G., "Surface Tension-Powered Self-Assembly of Microstructures – The State-of-the-Art," *Journal of Microelectromechanical Systems,* **vol. 12, no. 4,** Aug. 2003, pp. 387-417.

[78] Srinivasan, U., Liepmann, D., Howe, R., "Microstructure to Substrate Self-Assembly Using Capillary Forces," *Journal of Microelectromechanical Systems,* **vol. 10, no. 1,** March 2001, pp. 17-24.

[79] Zou, J., Chen, J., Schutt-Aine, J., "Plastic Deformation Magnetic Assembly (PDMA) of Out-of-Plane Microstructures: Technology and Application," *Journal of Microelectromechanical Systems,* **vol. 10, no. 2,** June 2001, pp. 302-309.

[80] Yao, J., "RF MEMS from a device perspective," *J. Micromech. Microeng.,* **Vol. 10,** (2000) pp. R9-R38.

[81] Katehi, L., Harvey, J., Brown, E., "MEMS and Si Micromachined Circuits for High-Frequency Applications," *IEEE Transactions on Microwave Theory and Techniques,* **Vol. 50, No. 3,** March 2002.

[82] Goldsmith, C.; Tsen-Hwang Lin; Powers, B.; Wen-Rong Wu; Norvell, B., "Micromechanical membrane switches for microwave applications" *Microwave Symposium Digest, 1995., IEEE MTT-S International*, 16-20 May 1995, Page(s): 91 -94 vol.1.

[83] Goldsmith, C., Malczewski, A., Yao, Z., Chen, S., Ehmke, J., Hinzel, D., "RF MEMS variable capacitors for tunable filters," *International Journal of RF and Microwave Computer-Aided Engineering,* **Vol. 9, No. 4.,** 1999, pp. 362 – 374.

[84] Harsh, K., Su, B., Zhang, W., Bright, V., Lee, Y.C., "The realization and design considerations of a flip-chip integrated MEMS tunable capacitor," *Sensors and Actuators,* **Vol. A 80,** (2000) pp. 108-118.

[85] Borwick, R., Stupar, P., DeNatale, J., Anderson, R., Tsai, C., Garret, K., "A High Q, Large Tuning Range, Tunable Capacitor for RF Applications," *Sensors and Actuators,* **Vol. A 103,** (2003) pp. 33-41.

[86] Yoon, J., Nguyen, C., "A High-Q Tunable Microelectromechanical Capacitor with Movable Dielectric for RF Applications," *Technical Digest, IEEE Int. Electron Devices Meeting,* San Francisco, CA, (2000), pp.489-492.

[87] Arcioni, P., Castello, R., Perregrini, L., Sacchi, E., Svelto, F., "An Innovative Modelization of Loss Mechanism in Silicon Integrated Inductors," *IEEE Transactions on Circuits and Systems II – Analog and Digital Signal Processing,* **Vol 46, No. 12.,** Dec. 1999, pp. 1453 – 1460.

[88] Chang, J.Y.-C.; Abidi, A.A.; Gaitan, M., **"**Large suspended inductors on silicon and their use in a 2-μm CMOS RF amplifier," *Electron Device Letters, IEEE ,* **Volume: 14 Issue: 5**, May 1993 Page(s): 246 -248

[89] Zhou, S., Sun, X., Carr, W., "A Micro Variable Inductor Chip Using MEMS Relays," *Transducers '97, 1997 International Conference on Solid-State Sensors and Actuators, Proceedings,* June 16-19,1997. pp. 1137-1140.

[90] Fan, L., Chen, T., Nespola, A., and Wu, M.C., "Universal MEMS Platforms for Passive RF Components: Suspended Inductors and Variable Capacitors," *Micro Electro Mechanical Systems, 1998. MEMS 98. Proceedings., The Eleventh Annual International Workshop on,* 25-29 Jan. 1998 Page(s): 29 –33.

[91] Saidani, M., Gijs, M., "Cubic Millimeter Power Inductor Fabricated in Batch-Type Wafer Technology," *Journal of Microelectromechanical Systems,* **vol. 12, no. 2,** April 2003, pp. 172-178.

[92] Yoon, J., Choi, Y., Kim, B., Eo, Y., Yoon, E., "CMOS Compatible Surface-Micromachined Suspended-Spiral Inductors for Multi-GHz Silicon RF Ics," *IEEE Electron Device Letters,* **Vol. 23, No. 10,** Oct. 2002, pp. 591 – 593.

[93] Lubecke, V.M.; Barber, B.; Chan, E.; Lopez, D.; Gross, M.E.; Gammel, P. "Self-assembling MEMS variable and fixed RF inductors" *IEEE Transactions on Microwave Theory and Techniques*, **Volume: 49 Issue: 11**, Nov. 2001, Page(s): 2093 –2098.

[94] Victor M. Bright, "Selected Papers on Optical MEMS," *SPIE Milestone Series,* Volume MS 153, 1999.

[95] Younse, J., "Mirrors on a Chip," *IEEE Spectrum,* **Vol. 30(11),** Nov. 1993, pp. 27-31.

[96] Machalicek, M., Sene, D., Bright, V.M., "Advanced Modeling of Micromirror Devices," *International Conference on Integrated Micro/Nanotechnology for Space Applications,* pp. 214-229, (1995).

[97] A. Tuantranont, V. M. Bright, L. A. Liew, W. Zhang, and Y. C. Lee, "Smart Phase-Only Micromirror Array Fabricated by Standard CMOS Process," *Proceedings of the 2000 IEEE International Conference on Microelectromechanical Systems (MEMS 2000),* Miyazaki, Japan, pp. 455-460, January 23-27, 2000.

[98] Bifano, T., Mali, R., Dorton, J., Perreault, J., Vandelli, N., Horenstein, M., Castanon, D., "Continuous-Membrane surface-micromachined silicon deformable mirror," *Optical Engineering,* **Vol.36 No. 5,** pp.1354-1360, May 1997.

[99] Reid, J.R.; Bright, V.M.; Comtois, J.H., "A surface micromachined rotating micro-mirror normal to the substrate," *Advanced Applications of Lasers in Materials Processing, 1996/Broadband Optical Networks/Smart Pixels/Optical MEMs and Their Applications, 1996. IEEE/LEOS 1996 Summer Topical Meetings: ,* 5-9 Aug. 1996, Page(s): 39 –40.

[100] Meng-Hsiung Kiang; Solgaard, O.; Muller, R.S.; Lau, K.Y., "Surface-micromachined electrostatic-comb driven scanning micromirrors for barcode scanners," *Micro Electro Mechanical Systems, 1996, MEMS '96, Proceedings. IEEE, The Ninth Annual International Workshop on ,* 11-15 Feb. 1996, Page(s): 192 –197.

[101] Su, G., Toshiyoshi, H., and Wu, M., "Surface-Micromachined 2-D Optical Scanners with High-Performance Single-Crystalline Silicon Micromirrors," *IEEE Photonics Technology Letters,* **Vol. 13 (6),** June 2001, pp. 606-618.

[102] McCarthy, B.; Bright, V.M.; Neff, J.A., "A solder self-assembled large angular displacement torsional electrostatic micromirror*," Micro Electro Mechanical Systems, 2002. The Fifteenth IEEE International Conference on,* 20-24 Jan. 2002, Page(s): 499 -502

[103] Judy, J., Muller, R., "Magnetically Actuated, Addressable Microstructures," *Journal of Microelectromechanical Systems,* **vol. 6, no. 3,** Sept. 1997, pp. 249-256.

[104] Garnier, A.; Bourouina, T.; Fujita, H.; Orsier, E.; Masuzawa, T.; Hiramoto, T.; Peuzin, J.-C., "A fast, robust and simple 2-D micro-optical scanner based on contactless magnetostrictive actuation," *Micro Electro Mechanical Systems, 2000. MEMS 2000. The Thirteenth Annual International Conference on,* 23-27 Jan. 2000 Page(s): 715 –720.

[105] Bloom, D.M., "The Grating Light Valve: revolutionizing display technology," *Silicon Light Machines publication.*

[106] Yasseen, A.A.; Smith, S.W.; Mehregany, M.; Merat, F.L., "Diffraction grating scanners using polysilicon micromotors," *Micro Electro Mechanical Systems, 1995, MEMS '95, Proceedings. IEEE* **,** 29 Jan.-2 Feb. 1995, Page(s): 175-180.

[107] S. S. Lee, L. Y. Lin, and M. C. Wu, "Surface-micromachined free-space micro-optical systems containing three-dimensional microgratings," *Applied Physics Letters*, October 9, 1995, Volume 67, Issue 15, pp. 2135-2137.

[108] Shih, W., Wong, C., Jeon, Y., Kim, S., Barbastathis, G., "Electrostatic and Piezoelectric Analog Tunable Diffractive Gratings," *Proceedings of CLEO 2002,* pp. 75-76.

[109] Geisberger, A., Sarkar, N., Ellis, M., and Skidmore, G., "Electrothermal Properties and Modeling of Polysilicon Microthermal Actuators," *Journal of Microelectromechanical Systems,* **vol. 12, no. 4,** August 2003, pp. 513-523.

[110] Huang, Q., Lee, N., "Analysis and Design of Polysilicon Thermal Flexure Actuator," *J. Micromech. Microeng.,* **Vol. 9,** (1999) pp. 64-70.

[111] Lott, C., McLain, T., Harb, J., and Howell, L., "Thermal Modeling of a surface-micromachined linear thermomechanical Actuator," *Model. Simulation Microsyst.,* pp 370-373, 2001.

[112] Manginell, R., "Physical properties of polysilicon," PhD. Thesis, University of New Mexico, 1997.

[113] Suarez, J., Johnson, B., El-Kareh, B., "Thermal Stability of polysilicon resistors," *IEEE Trans. Components, Hybrids, Manufact. Technol.,* **vol.15, no.3,** pp. 386-392, 1992.

[114] Arx, M., Paul, O., Baltes, H., "Process-dependent thin-film thermal conductivities for thermal CMOS MEMS," *Journal of Microelectromechanical Systems,* **vol. 9,** March 2000, pp. 136-145.

[115] Kotchetkov, D., Zou, J., Balandin, A., Florescu, D., and Pollak, F., "Effects of dislocations on thermal conductivity of GaN layers," *Appl. Phys. Lett.,* **vol.79, no. 26**, pp. 4316-4318, 2001.

[116] McQuarrie, D., "Statistical Thermodynamics," Mill Valley, CA: University Science Books, 1973.

[117] Lide, D. R., "Handbook of Chemistry and Physics," Ann Arbor, MI: CRC, 1994.

[118] Ellis, M., Skidmore, G., Sarkar, N., "Finite Element Analysis and Vacuum Testing of Thermal Bimorph Actuators," presented at *TEXMEMS III, Dallas, TX, 2001.*

[119] Pister, K., Judy, M., Burgett, S., Fearing, R., "Microfabricated Hinges," Sensors and Actuators, vol. A33, no. 3, pp. 249 - 256, June 1992.

[120] Fan, L, Wu, M., Choquette, K., Crawford, M., "Self-Assembled Microactuated XYZ Stages for Optical Scanning and Alignment," Proceedings of Transducers '97, the 1997 International Conference on Solid-State Sensors and Actuators, Chicago, IL, vol. 1, pp. 319-322, 1997.

[121] Fukuta, Y., Collard, D., Akiyama, T., Yang, E.H., Fujita, H., *"*Microactuated Self-Assembling of 3D Polysilicon Structures with Reshaping Technology*"*, Proceedings, IEEE., Tenth Annual International Workshop on Micro Electro Mechanical Systems, Nagoya, Japan, pp. 477-481, Jan. 1997.

[122] Zou, J., Chen, J., Liu, C., *"*Plastic Deformation Magnetic Assembly (PDMA) Of 3D Microstructures: Technology Development and Application*"*, Proceedings of Transducers '01, paper, the 11th International Conference on Solid-State Sensors and Actuators, Munich, Germany, June 11-14, 2001.

[123] [5] Lubecke, V., Barber, B., Chan, E., Lopez, D., Gross, M., and Gammel, P., "Self-Assembling MEMS Variable and Fixed RF Inductors," IEEE Transactions on Microwave Theory and Techniques, Vol. 49, No. 11, November 2001.

[124] Skidmore, G., Parker, E., Ellis, M., Sarkar, N., Merkle, R., *"*Exponential Assembly*"*, Nanotechnology Vol. 12, pp. 316-321, 2001.

[125] Geisberger, A., Jungen, A., Sarkar, N., Ellis, M., and Skidmore, G., "Modeling Electrothermal Plastic Deformation Self-Assembly," *Technical Proceedings of the 2003 Nanotechnology Conference and Trade Show,* **Vol.1,** pp. 482-485.

[126] Finot, M., and Suresh, S., "Small and large deformation of thick and thin-film multi-layers: Effects of layer geometry, plasticity, and compositional gradients," *Journal of the Mechanics and Physics of Solids,* **vol. 44, No. 5,** pp. 683-721, 1996.

[127] Harris, K. and King, A., "Direct observation of diffusional creep VIA TEM in polycrystalline thin films of gold," *Acta Mater.,* **Vol 46, No. 17,** pp. 6195-6203, 1998.

[128] Geisberger, Aaron, US patent no. 6,617,185, "System and method for latching a micro-structure and a process for fabricating a micro-latching structure."

[129] Lubecke, V., Barber, B., Chan, E., Lopez, D., Gross, M., and Gammel, P. "Self-Assembling MEMS Variable and Fixed RF Inductors," *IEEE Transactions on Microwave Theory and Techniques,* **Vol. 49, No. 11,** November 2001, pp. 2093-2098.

[130] Chi, C.Y., Rebeiz, G.M., "Planar millimeter-wave microstrip lumped elements using micro-machining techniques," *Proceedings of the IEEE MTT-S International Microwave Symposium Digest,* **Vol. 2,** 1994, pp. 657-660.

[131] Sun, Y., Zejl, H., Tauritz, J.L., Baets, R.G.F., "Suspended Membrane inductors and capacitors for application in silicon MMICs," *Proceedings of the IEEE Microwave and Millimeter-wave Monolithic Circuits Symposium,* 1996, pp.99-102.

[132] Zou, J., Nickel, J.G., Trainor, D., Liu, C., Schutt-Aine, J.E., "Development of vertical planar coil inductors using plastic deformation magnetic assembly (PDMA), *Proceedings of the IEEE MTT-S Digest,* May 2001.

[133] Fan, L., Chen, R.T., Nespola, A., Wu, M.C., "Universal MEMS Platforms for passive RF components: suspended inductors and variable capacitors," *Proceedings of the IEEE Micro Electro Mechanical Systems,* 1998, pp. 29-33.

[134] Dahlmann, G., Yeatman, E., Young, P., Robertson, I., Lucyszyn, S., "Fabrication, RF characteristics, and mechanical stability of self-assembled 3D microwave inductors," *Sensors and Actuators A,* **97-98 (2002)** pp. 215-220.

[135] Park, J.Y., Allen, M.G., "Packaging-compatible high Q microinductors and microfilters for wireless applications, *IEEE Trans. Components Packaging Manuf. Technol.,* **Part B 22 (2)** (1999) pp.207-213.

[136] Victor M. Bright, "Selected Papers on Optical MEMS," *SPIE Milestone Series,* Volume MS 153, 1999.

[137] McManamon, P., Dorschner, T., Corkum, D., Friedman, L., Hobbs, D., Holz, M., Liberman, S., Nguyen, H., Resler, D., Sharp, R., Watson, E., "Optical Phased Array Technology," *Proceedings of the IEEE,* **Vol. 84, No. 2,** Feb. 1996.

[138] Safavi-Naeni, S., "Antennas and Wireless Systems," *Course notes for ECE 476,* **p.77,** 2002.